Design of a Low Aspect Ratio UAV
Final Report

M.T.H. Brown, S. Gamme, R.P.J. Laan,
P. Mouri Sardar Abadi, S. Padmos, R.M. Regtuit,
M. Schmeetz, Y.R. Tan, B. Timmer, X. Wang

AE3200 DSE Group 17

July 2, 2013

Design Synthesis Exercise 2013

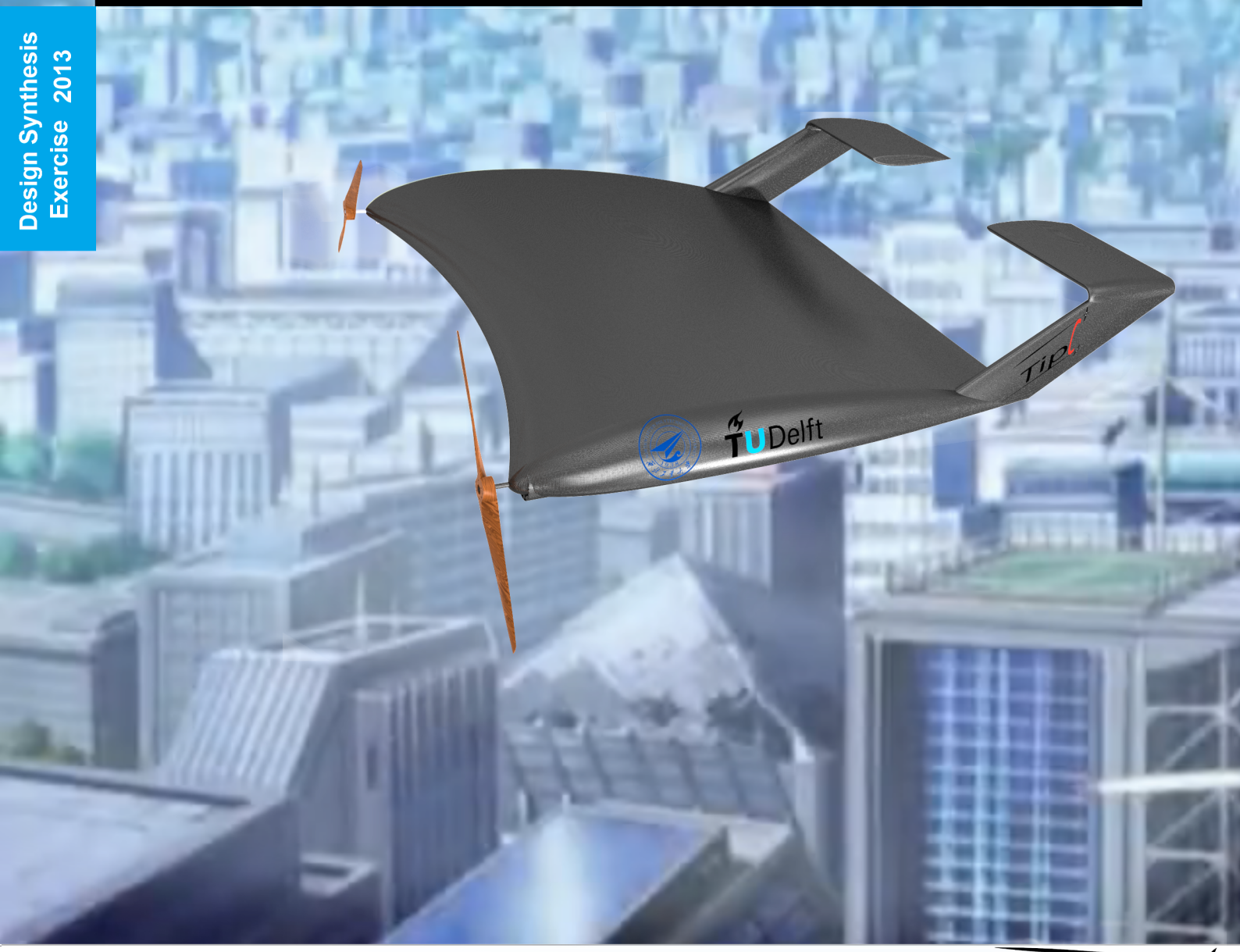

TU Delft Delft University of Technology

TipC

Aerospace Engineering **Challenge the future**

Preface

This report is the last progress report, the Final Report of DSE Group 17. In this report, the chosen concept "Tip-C" from the Mid-Term phase is finalised. The aerodynamic characteristics, propulsion and performance, stability and control, landing gear, sub-systems, and structural characteristics are determined.

Readers who are particularly interested in the design of Tip-C can read Chapters 4-10. Readers who are more interested in the sustainable development strategy and market analysis are advised to read Chapters 18 and 19.

We would like to thank our tutor Dr. ir. Mark Voskuijl and our coaches Adolfo Chaves Jimenez and Hamid Hosseini for giving us feedback on our project progress. We would also thank Lv Peijian "Lex" for the communication with Northwestern Polytechnical University. In addition, we would also like to express our gratitude to Dr. ir. L.L.M. Veldhuis, Dr. ir. R. Vos, Dr. ir. H.G. Visser, Dr. ir. R. De Breuker, Prof. D. Steenhuizen, Prof. A. Gangoli Rao, Prof. A. Elham, Dr. ir. A.C. in 't Veld, Dr. ir. E. van Kampen, Dr. C. Kassapoglou, Dr. ir. O.K. Bergsma, Dr. ir. G. La Rocca, and Dr. M.D. Pavel for their valuable advice during the design process. Their knowledge is used to get a better insight on their field of expertise. Special thanks go to E. van den Bos for his help with CATIA.

Contents

Summary

The DSE group from Delft University of Technology is assigned to come up with a conceptual design for a low aspect ratio (AR) Unmanned Aerial Vehicle (UAV) to participate in the AVIC Cup - International UAV Innovation Grand Prix 2013 in Beijing. The DSE group designs the UAV, while the Northwestern Polytechnical University (NPU) in Xi'an, China, finalises the design, builds it and then operates the aircraft during the competition.

A low AR aircraft has the major advantage of exceptional descent and stall performance. However, it has reduced performance during cruise and climb. Hence the goal of this project is, to come up with a design with good climb and descent performance, while being as efficient in cruise as conventional aircraft with normal AR. In this report, the detailed design of the final concept, called "Tip-C", is discussed and recommendations are made for NPU.

The aspect on which the UAV will be graded during the competition is mainly innovation, which is why innovation is one of the main drivers of this aircraft design. Tip-C has multiple innovative features:

- a C-wing, which functions as tail, stabiliser, and helps to reduce induced drag;
- tip-mounted propellers, to counteract the wingtip vortices and therefore reduce induced drag;
- a belly flap, to increase takeoff and landing performances;
- an inverted plaster wing planform, which has negative sweep and increased efficiency when using tip-mounted propellers;
- and low AR itself, which improves descent and stall performances.

The aerodynamic model that is made, mainly focuses on the effect of tip-mounted propellers. They produce an induced velocity, which affects the wing directly behind it. When counteracting the tip vortices, the induced drag of the aircraft is slightly reduced. The propellers also increase $C_{L_{max}}$ by 20%. The C-wing is also added to the model, which yields that the trimmed aircraft has a similar cruise efficiency as a general aviation aircraft.

The stability of Tip-C is investigated via two Vortex Lattice Method programs, called AVL and Tornado. Both software calculate stability and control derivatives for a given flight conditions. These derivatives are then implemented into a numerical stability model, created in MATLAB. The model gives the responses of the UAV to certain disturbances. It follows that Tip-C is stable, or slightly unstable, during all flight phases.

The controllability of Tip-C is analysed by using the trim conditions of all flight phases obtained by the stability department. The controllability during cruise meets the requirements. The other flight phases require more research, since they are performed at higher angles of attack, and the accuracy of the software is reduced. The sizing of the belly flap is done according to literature.

The design of the propulsion system starts with determining the propeller design point. After that, the propulsion system can be designed in detail. This detailed design consists of propeller airfoil selection and engine selection. Variable pitch is investigated as well. Range, endurance, climb, descent, turn, landing and takeoff are analysed for performance.

For the landing gear, long struts are needed for propeller clearance. The main landing gear is positioned at 32% of the chord, because of the forward centre of gravity position. The gear is a retractable tricycle and is designed using off-the-shelf components.

The electrical, mechanical and pneumatic systems are sized for aircraft systems.

Because of the low AR, the bending moments on the body are small. This results in a simple lightweight structure. Spruce wood is used for the primary structure and foam as filling.

Nomenclature

α	Angle of Attack [deg]
$\bar{c}$	Mean Aerodynamic Chord [m]
$\bar{x}_{cg}$	Coordinate of centre of gravity divided by length of mean aerodynamic chord [-]
$\bar{x}_{np}$	Coordinate of neutral point divided by length of mean aerodynamic chord [-]
$\dot{m}$	mass flux through propeller [kg/s]
η_p	Propeller efficiency [-]
$\frac{d\epsilon}{d\alpha}$	Downwash effect of wing on tail [-]
γ	Flight Path Angle [deg]
γ_A	Approach flight path angle [deg]
γ_d	Descent gradient [deg]
γ_{scr}	Screen height flight path angle [deg]
Λ	Sweep angle [deg]
λ	Advance ratio [-]
μ	Bank angle [deg]
Ω	Angular rotation speed of motor [rad/s]
ϕ	Relative angle - between the plane of rotation and the relative velocity vector
ρ	Density $[\frac{kg}{m^3}]$
σ	Normal stress $[\frac{N}{m^2}]$
σ_d	Duct expansion ratio [-]
τ	Shear Stress $[\frac{N}{mm^2}]$
θ	Pitch angle [deg]
θ_{hor}	Deflection angle of the Horizontal of the C-wing[rad]
θ_{tip}	Deflection angle of the Tip of the C-wing [rad]
θ_{ver}	Deflection angle of the Vertical Section of the C-wing[rad]
AR_p	Propeller aspect ratio [-]
b_h	Span of the Horizontal Section of the C-wing [mm]
b_v	Span of the Vertical Section of the C-wing [mm]

$C_{D,0}$ Drag Coefficient at Zero Lift (parasitic drag) [-]

c_d Section drag coefficient [-]

$C_{L_{\alpha_h}}$ Lift curve slope for horizontal tail [-]

C_{L_α} Lift curve slope for aircraft [-]

$C_{L_{max}}$ Maximum Lift Coefficient [-]

C_{L_p} Propeller Lift Coefficient [-]

c_l Section lift coefficient [-]

$C_{N_{max}}$ Maximum Normal Force Coefficient [-]

C_P Power coefficient [-]

c_{root} Root Chord [m]

c_{tip} Tip Chord [m]

C_T Thrust coefficient [-]

CO_2 Carbon Dioxide

D_{duct} Diameter of the ducted fan [m]

D_g Ground friction [N]

D_{open} Diameter of the open rotor system [m]

D_p Propeller Diameter [m]

E_{batt} Battery capacity [Watt-hour]

E_{spruce} Young's Modulus of Spruce $[\frac{N}{mm^2}]$

F_{brake} Braking force [N]

$F_{N,f}$ Normal force front wheels [N]

f_{usable} Depth of discharge [-]

h_{scr} Screen height [m]

I_h Moment of Inertia of the Horizontal Section of the C-wing

I_v Moment of Inertia of the Vertical Section of the C-wing

i_0 Idle current [Ampere]

I_{roll} Roll Inertia $[kgm^2]$

K_{np} Correction factor for number of blades [-]

L/D Lift over Drag Ratio [-]

L_{hs} Lift Force Acting on the Horizontal Section of the C-wing

l_h Horizontal tail arm [m]

L_{vs} Lift Force Acting on the Vertical Section of the C-wing

l_v Vertical tail arm [m]

P_{br} Brake Horse Power [hp]

P_{shaft} Shaft power [Watt]

R_{min} Minimum Turn radius [m]

R_m Internal motor resistance [Ohms]

$S_{a_{land}}$ Airborne landing distance [m]

$S_{a_{takeoff}}$ Airborne takeoff distance [m]

$S_{g_{land}}$ Ground roll landing distance [m]

$S_{g_{takeoff}}$ Ground roll takeoff distance [m]

S_h Horizontal Tail Surface [m^2]

S_{land} Landing Distance [m]

S_v Vertical Tail Surface [m^2]

T Total thrust[N]

T_{duct} Static thrust of the ducted fan [N]

T_{open} Static thrust of the open rotor system [N]

u_0 initial velocity [m/s]

V_B Design Rough-air Speed [$\frac{m}{s}$]

V_C Design Cruise Speed [$\frac{m}{s}$]

V_D Design Dive Speed [$\frac{m}{s}$]

V_S Design Stall Speed [$\frac{m}{s}$]

V_{av} Average airspeed for lift generation [$\frac{m}{s}$]

v_a Axial velocity [m/s]

V_C Cruise Velocity [$\frac{m}{s}$]

V_E Effective velocity [m/s]

V_e exit velocity [m/s]

V_H Horizontal Tail Volume Coefficient [-]

V_h Free stream flow velocity at horizontal tail [$\frac{m}{s}$]

v_i Induced velocity [m/s]

V_{LOF} Lift off velocity [m/s]

V_R Relative velocity [m/s]

V_{stall} Stall Velocity [$\frac{m}{s}$]

V_T Touchdown velocity [m/s]

v_t Tangential velocity [m/s]

V_V Vertical Tail Volume Coefficient [-]

$V_{tip_{cruise}}$ Tip velocity of blade during cruise [$\frac{m}{s}$]

μ_r Coefficient of friction [-]

A Compressed surface area [mm^2]

a.c. Aerodynamic Centre

AoA Angle of Attack [deg]

AR Aspect Ratio [-]

B Number of propeller blade

b Wing Span [m]

c.g. Centre of Gravity

D Drag [N]

d_ail Distance aileron force [m]

d_all Length from tip to tip [m]

d_bat Distance to battery [m]

d_elv Distance of elevator force [m]

d_eng Distance of engine [m]

d_mlg Distance to main landing gear [m]

d_rib1 Distance to the outer rib

d_rib2 Distance to the inner rib

d_vt Length of vertical tail surface [m]

DSE Design Synthesis Exercise

F Axial load [N]

F Force [N]

f Ratio between takeoff and landing weight [-]

F_ail Force created by aileron [N]

F_hor Resulting Force Acting on the Horizontal Section of the C-wing [N]

F_ht Force created by elevator [N]

F_rud Force created by vertical stabiliser and rudder [N]

F_ver_y Resultant Force Acting in the y-axis Direction [N]

F_ver_z Resultant Force Acting in the z-axis Direction [N]

FBS Functional Breakdown Structure

FEM Finite element method

FFD Functional Flow Diagram

H Hub radius [m]

I Moment of inertia [mm^4]

L_hor Lift Force Acting on the Horizontal Section of the C-wing [N]

L_ver Lift Force Acting on the Vertical Section of the C-wing [N]

LCC Life-Cycle Costing

M Applied moment [Nm]

m mass [kg]

M_hor Moment Acting on the Horizontal Section of the C-wing [Nm]

MAC Mean Aerodynamic Chord [m]

MMOI Mass Moment of Inertia [kgm^2]

MTOW Maximum Takeoff Weight [kg]

n Rotational speed of the engine [$\frac{rad}{s}$]

n.p. Neutral Point

NPU Northwestern Polytechnical University

OEW Operating Empty Weight [kg]

Q Statical Moment of Area [mm^2]

R Tip radius [m]

r Distance [m]

RDT Requirements Discovery Tree

ROC Rate of Climb [$\frac{m}{s}$]

S Wing surface area [m^2]

S.M. Stability Margin [m]

sin(γ) Climb Gradient [$\frac{rad}{s}$]

T Thrust [N]

t Thickness [mm]

TOP Takeoff Parameter [-]

TRL Technical Readiness Level

U Gust Speed [$\frac{m}{s}$]

UAV Unmanned Aerial Vehicle

V Velocity [$\frac{m}{s}$]

v Voltage [V]

W Total Aircraft Weight [N]

W_ail Weight of one of the aileron mechanisms [kg]

W_bat Weight of one battery [kg]

W_bfm Weight of belly flap mechanism [kg]

W_eng Weight of one engine [kg]

W_hor Weight Force of the Horizontal Section [N]

W_ht Weight of one horizontal tail surface [kg]

W_mlg Weight of one of the main landing gear [kg]

W_nw Weight of the nose wheel landing gear [kg]

W_pay Weight of the payload [kg]

W_ver Weight Force of the Vertical Section [N]

W_vt Weight of the vertical tail with rudder [kg]

y Distance from neutral line [m]

1 Introduction

After almost 3 years of studying at the Delft University of Technology, many aspects of the design process of an aircraft have been learned. In the first year the students learned how to explore a specific field for a design. The second year had a slightly more technical aspect of the designing process. In the third year, all the knowledge gained during the two and a half year of study is used in the Design Synthesis Exercise (DSE). The DSE is the final project of the bachelor program of Aerospace Engineering and it aims to synthesise all the theoretical knowledge obtained in previous years.

A group of 10 students is assigned to come up with a conceptual design of a low aspect ratio (AR) Unmanned Aerial Vehicle (UAV) with an electrical propeller propulsion system. The UAV is expected to have excellent climb, descent and field performance, while the cruise performance should be comparable to a conventional aircraft. A conventional is an aircraft with a wing, fuselage, tail, and a normal AR between 5 and 15. This UAV is designed and will participate in the innovation event of the 2013 Beijing UAV Competition. The main aim of the innovation event in the competition is to encourage exploration of innovative technology and design. Hence, innovation is emphasised on during the design process. A conceptual design is made by the DSE group and will be handed over to the Northwestern Polytechnical University (NPU) in Xi'an (China) for further development and production. The Project Objective Statement is defined as:

Come up with an innovative conceptual design of a low AR UAV with a cruise flight performance comparable to a conventional UAV of the same weight class, for the 2013 Beijing UAV competition, which is within manufacturing capabilities of the Northwestern Polytechnical University with a limited budget of 50,000 ¥, by 10 students in 10 weeks.

The goal of this design is to ensure that the UAV has excellent climb, descent and field performance. Currently, low AR aircraft have poor cruise performance properties [1], hence innovative concepts should be included to improve the cruise performance. In order to compare this design to other conventional aircraft, comparable transport efficiency, maximum takeoff weight and payload weight are required. This can be summarised in a Mission Need Statement:

Fly with excellent climb/descent/field performances and comparable transport efficiency with respect to a conventional UAV with similar maximum takeoff weight.

In previous reports, which are the Project Plan, Baseline Report and Mid-Term Report, the set-up, main overview of the project and the design options are explained. A morphological diagram is made and used to create multiple conceptual aircraft designs. Finally one concept, "Tip-C", is chosen as the final design. This design is further developed and presented in this report. In Chapter 2 the Mid-Term geometry of Tip-C is presented. In Chapter 3 the mission profile, functions and operation during flight of Tip-C are presented. After this the technical design of Tip-C is done. Chapters 4-10 explain this. After the technical design is finished a production and test plan is created, see Chapters 14 and 15. A design summary is given in Chapter 16 together with a general sensitivity analysis and a requirements compliance check. In Chapter 17 a risk management is shown. Chapter 18 shows the applied sustainable development strategy. Finally, in Chapter 19 a market analysis is performend and in Chapter 20 the budget is shown.

2 Mid-Term Geometry of Tip-C

After the mid-term phase, the rough geometry of Tip-C is known. This geometry is the first input for the sizing which is done during the final phase of the DSE. The geometry can be found in table 2.1.

Table 2.1: Geometry of Tip-C after mid-term phase.

b [m]	1.105
c_{root} [m]	1.000
c_{tip} [m]	1.100
S $[m^2]$	1.220
AR [-]	1.000
MAC [m]	1.050
l_h [m]	0.900
V_H [-]	0.100
S_h $[m^2]$	0.1423
$S_{h_{half}}$ $[m^2]$	0.1423
b_h [m]	0.4500
c_h [m]	0.1581
S_v/S [-]	6.190%
S_v $[m^2]$	0.0755
$S_{v_{half}}$ $[m^2]$	0.0378
b_v [m]	0.2108
$c_{v_{root}}$ [m]	0.2000
$c_{v_{tip}}$ [m]	$= c_h$

The used axis system is also defined during the mid-term phase and repeated in figure 2.1.

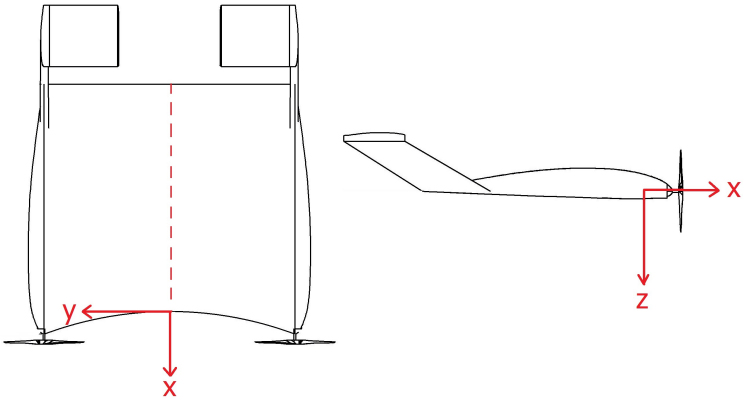

Figure 2.1: Axis definition used for calculations.

3 Operations and Functions

In order to complete its mission, the aircraft needs to be able to complete certain functions. These functions are derived from the aircraft mission profile. After finding and defining all the functions, the functional breakdown structure (FBS) is discussed, which splits up the main functions into sub-functions (and those into sub-sub-functions if needed), in order to show how the functions depend on each other.

3.1 Mission profile

Before the FFD and FBS are shown, first the mission profile, which was defined in the base-line phase, is summarised. The mission is to demonstrate to the jury of the 2013 Beijing UAV Competition the innovative and performance characteristics of the aircraft. The general phases of the aircraft mission are:

1. Start-up
2. Taxi
3. Short takeoff
4. Steep climb
5. Cruise
6. Manoeuvres
7. Steep descent
8. Short landing
9. Taxi
10. Shut down
11. Maintenance

These mission stages are integrated in the flight profile of figure 3.1.

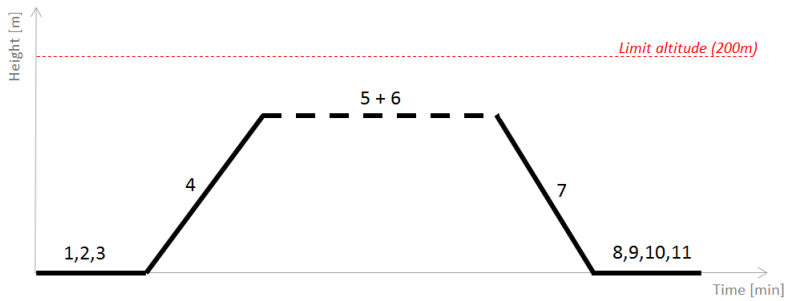

Figure 3.1: Mission profile which will be performed during the Beijing UAV competition.

3.2 Functional Breakdown Structure

The goal of a FBS is to give a better overview on how the different functions influence each other. Figure 3.2 displays how the success of the mission depends on the different functions the UAV has to fulfil. Time independent functions are shown in the FBS as well. These extra functions are controllability and stability requirements, since they hold throughout the whole mission.

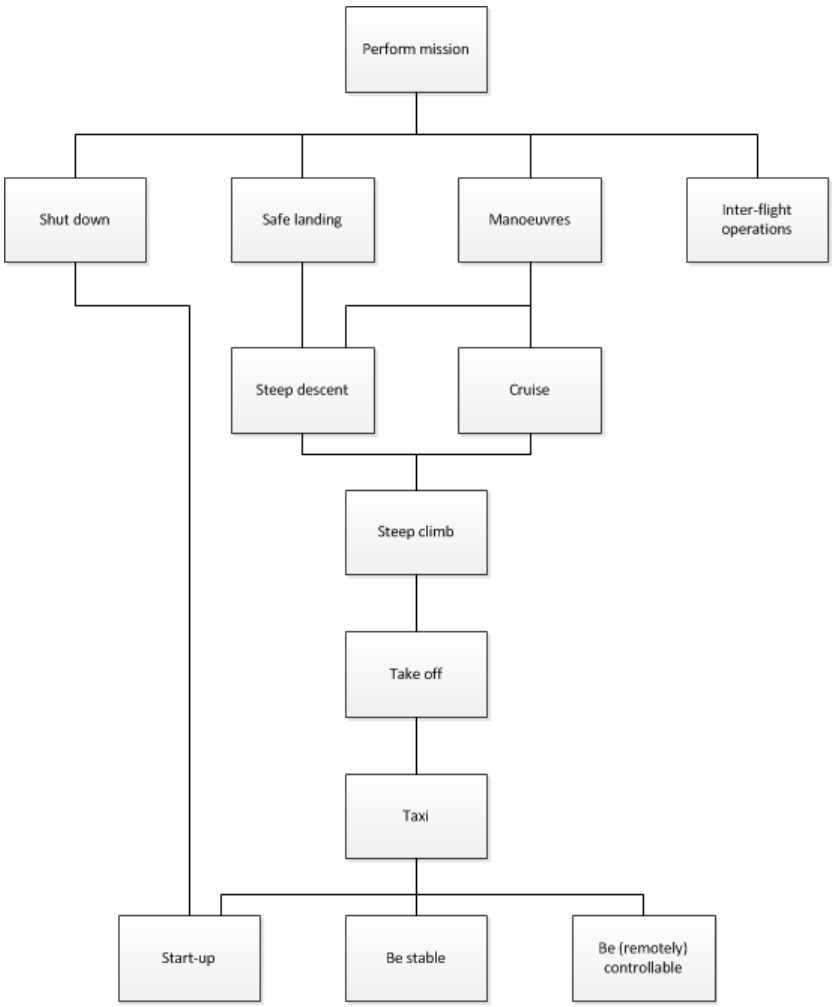

Figure 3.2: Functional breakdown structure for low AR UAV

3.3 Flight Operations

Besides the functions mentioned in the FBS, other operations have to be performed. Before Tip-C can actually fly its mission on the Beijing UAV Competition, some steps have to be performed beforehand. Once the conceptual design is completed, detail design is performed. If the total design is finished, the production phase can start. During this phase multiple components are made or ordered, such that the whole aircraft becomes one coherent piece. The construction must be checked carefully, to spot any mistakes made during assembly, before continuing to the next phase. This next step is to check all the different subsystems before making test flights. This includes retracting and deploying of the landing gear, checking the brakes, see whether the nose wheel steers properly, inspect the deflection of the control surfaces and investigate whether the engines function properly. If all these inspections are positive, one could continue to start on the test flight. The test flight should start with very simple manoeuvres at first to more risky manoeuvres later. If everything is so far still as according to expectations, one could prepare the UAV for the competition in Beijing.

4 Aerodynamic Performance

In this section, the aerodynamic performance of the aircraft is analysed. First some theory is discussed to understand the aerodynamic properties. This is followed by a description of the numerical tools used in the aerodynamic model. Before implementing them in a model, the airfoil is chosen. This is done with a 2D analysis and trade-off first, followed by a 3D analysis on the preliminary planform. A more extensive aerodynamic model is then made using the chosen airfoil and using an updated planform. In this model the tip-mounted propellers are taken into account and their effects are investigated. Using data from the stability and controllability department, the tail is modelled. In addition to the choice of airfoil, the incidence angle for the vertical tail is sized. The goal of this is to avoid a resultant horizontal force on the fin. The effect of trimming the aircraft is then analysed.

4.1 Background

To comprehend the steps taken to analyse the aerodynamic performance, a small theoretical background is given. Attention is mainly given to the addition of the tip-mounted propellers and the C-wing.

4.1.1 Propeller Influence

It was described before that the propeller will improve the aerodynamic performance. To understand these effects, first an understanding of tip vortices should be gained. It is known that lift is generated by a change in pressure over the airfoil. The upper part experiences a lower pressure than the lower part, this pressure difference generates a net upwards force. For a finite wing, the pressure difference wants to reach zero at the tip of the wing, since the system wants to reach equilibrium. This causes the flow at the tips to move around the tip from the lower to the upper surface. This circular motion of air is called a trailing vortex, which is visualised in figure 4.1. This vortex creates a downwash on the wing, which decreases the effective AoA. This does not only decrease lift at that point, but the lift vector is also tilted backward, which adds a drag component. This drag component is called induced drag.

Figure 4.1: Wingtip vortex visualisation [2]

Wingtip mounted propellers can be used to reduce this effect. A short introduction to propeller aerodynamics is given first. In order to create thrust, an induced velocity is generated, this follows

from the propeller disk theory described in equation 4.1.

$$T = \dot{m} \cdot (u_e - u_0) \tag{4.1}$$

This velocity component can be split up in an axial and tangential direction. The axial induced velocity increases the dynamic pressure over the wing changing the resulting forces on the wing. The tangential component of the induced velocity, also called swirl, creates a larger AoA at the going-up blade which creates extra lift on that part of the wing. On the going-down blade, the AoA decreases, hence a decrease in lift is present. The net effect is still positive, and if tip-mounted propellers are used, the benefit is even larger as shown qualitatively in figure 4.2. Now one can reason that the going-down blade will counteract the tip vortex, reducing the induced drag.

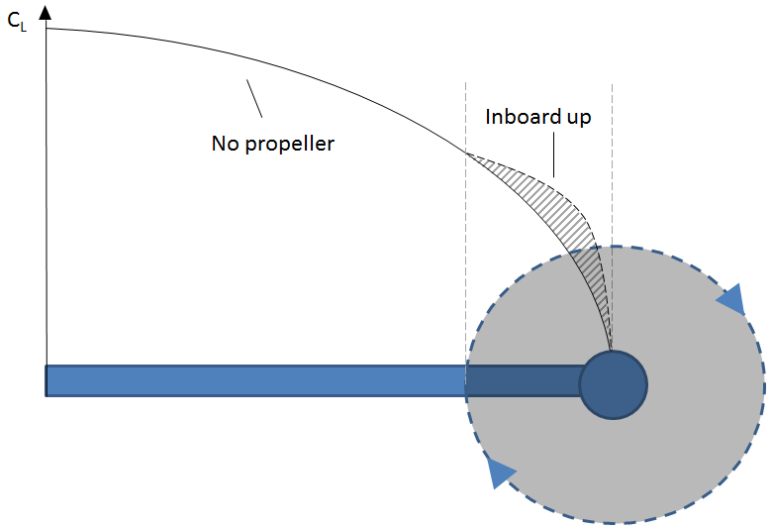

Figure 4.2: Tip-mounted propellers net effect

In order to gain a feeling about the factors that influence this effect, a small elaboration on figure 4.3 is given. When increasing the RPM, the ωR vector becomes larger, so the angle ϕ becomes smaller. This means the effective AoA α becomes larger, which results in a higher induced velocity. Physically it means that the aerodynamic advantages of the tip-mounted propellers are larger. This is also the case when reducing the free stream airspeed as described in section 7.4. If the induced velocities become too high, the stall AoA will be exceeded and performance will deteriorate.

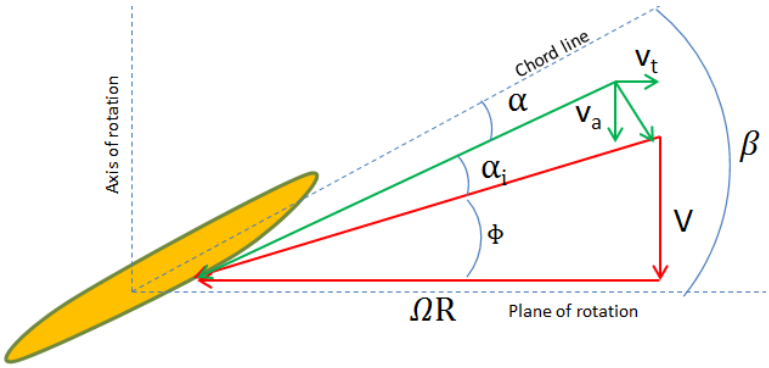

Figure 4.3: Propeller geometry (Adapted from [3])

4.1.2 C-wings

For this UAV, C-wings were chosen. They can be described as Prandtl wings with an interrupted horizontal stabilizer. According to [4], the induced drag reduction is roughly the same as the traditional Prandtl wing, but the viscous drag will be less since the wetted area is less. However this is structurally challenging since a closed box structure is much more efficient. Another downside is that a constant lift distribution on the horizontal part is not possible since lift must be zero on the tips. This will yield possible large control surface deflections. This UAV will be the first flying aircraft with this kind of tail, allowing the team to research the aforementioned effects.

4.2 Aerodynamic model

In order to optimize the aerodynamic performance of the aircraft, an aerodynamic analysis model should be made. Inputs for this model are mainly flight conditions such as airspeed, motor RPM and atmospheric conditions. The output are the aerodynamic properties of the aircraft such as C_L, C_D as functions of alpha. These outputs are necessary inputs for the stability and controllability, performance and the propulsion departments. This model should not only be accurate but its user friendliness is a major feature. Since NPU will do a more detailed analysis on this UAV, it is important that executing the model doesn't require much time or effort. Before proceeding to the development of the model, an airfoil is chosen. This was done by a 2D analysis first, followed by a 3D analysis.

4.2.1 Numerical tools

To come up with an aerodynamic model of the UAV, different numerical tools are needed. Next to 2D airfoil characteristics, one should also do a 3D analysis of the aircraft. Also the propeller contribution needs to be investigated. A lot of open source software is available. In this section, XFOIL, XFLR5 and QProp are discussed which is used in the analysis.

XFOIL

XFOIL is a panel code program which produces 2D airfoil data. The FORTRAN executable is used for the design and analysis of subsonic isolated airfoils. This can be done for varying Reynolds and/or Mach numbers. The program also takes into account the viscous effects of air. This software is mainly used for the 2D airfoil selection. A downside of XFOIL is that it can only handle a limited amount of separated flow. This means inaccuracies will occur within and after the stall angle region. If better stall approximations are needed, the Eppler method should be used [5].

XFLR5

XFLR5 is also an open source software which is gaining popularity the last few years. It allows users to create a basic 3D geometry and generate a CFD mesh. When this is done, a 2D airfoil analysis is done using the XFOIL plug-in. To come up with 3D aerodynamic properties, 3 methods can be selected, namely Lifting Line Theory (LLT), Vortex Lattice Method (VLM) and the 3D panels method. The first makes use of Prandtls theory combined with the Kutta-Joukowski theory. A finite number of horseshoe vortices, which each have their aerodynamic properties, are placed along the lifting line, each of them creates their own lift. Integrating the separate vortices along the span gives the aerodynamic properties of the aircraft. This classical lifting-line theory is not appropriate for low AR wings and swept wings [6]. With VLM, the previous model is extended by placing a series of lifting lines on the wing. In fact, an infinitely thin sheet of discrete vortices is created to compute aerodynamic properties. In this method, viscosity is neglected. Fortunately XFLR5 interpolates the viscous effects from the previously generated XFOIL 2D airfoil data. This method is used in the aerodynamic model

since it is compatible with the induced velocities of the propeller, see section 4.2. Since XFOIL data is used, the XFLR5 model is also not very accurate in the stall region. The 3D panel method takes the thickness of the wing into account, whereas the VLM method only takes the mean camber line of the wing. It models the wing as a sum of doublets and sources distributed over the top and bottom surfaces of the wing. To determine the properties of the doublets and sources, boundary conditions are evaluated. For more theoretical background on these methods, one can consult [7].

Qprop

To integrate the propeller in the aerodynamic model, Qprop is used. It is a FORTRAN executable which can predict the performance of propeller-motor combinations. It uses a propeller definition file and a motor definition file where basic the basic propulsion component characteristics are specified. An optional runfile can be specified to define the velocity, RPM, voltage and the change in pitch. The outputs are the propulsion properties such as thrust,electric current, shaft power, efficiencies etc. Also the induced velocities in axial and tangential direction along the blade is an output. This is used in the aerodynamic model to look at the propeller interaction on the wing. The theory behind this program is thoroughly explained in [8].

4.3 Development of the Numerical Model

The 3D flow analysis of the geometry is done using XFLR5. An interface between XFLR5, Qprop and Matlab is made by M. Dimchev This tool, called xflrP, first uses Qprop to calculate induced velocities at the propeller plane using the blade element method. The result is saved in a text file and processed by Matlab to account for the slipstream effect on the wing. Now another text file is generated which is used in the VLM analysis in xflrP. As mentioned before, the user friendliness is an important factor in the model. That is why the described program is modified so everything can be controlled from a Matlab environment. A flowchart of the program is described in figure 4.4. After defining the inputs, it is checked whether the specified case was already executed using the filename. If not, Qprop is executed and its output is directly analysed and converted to induced velocities. When this is done, xflrP starts up. The user is now required to do an analysis with the specified speed. The polar should be exported to a text file with an exact name in a specified folder. When closing xflrP, Matlab reads in the generated file. To avoid negative C_D values, the thrust from Qprop is added to the C_D values. If the landing gear is deployed, the landing gear drag is added to the C_D. Then the output is plotted in the Matlab environment. To check the effect of the propeller, the case without prop at the same cruise speed is also analysed and plotted.

4.4 Results

4.4.1 Body Airfoil Selection

An important aspect of the aerodynamic design is the airfoil selection. This was already done in the midterm report [9]. Only a handful of airfoils were considered but it is likely to resemble the detailed design airfoil so it was adequate for rough parameter estimations. Now a more detailed analysis is done for the main body, the vertical fin and the horizontal stabilizer.

The aerodynamic parameters of these airfoils were obtained from XFOIL at the operating Reynolds number for cruise.

2D Analysis

In the midterm phase, the body had a maximum thickness of 12 cm. All systems fitted inside and the centre of gravity (c.g.) was within the stability range. Therefore again a maximum 12 cm thickness is

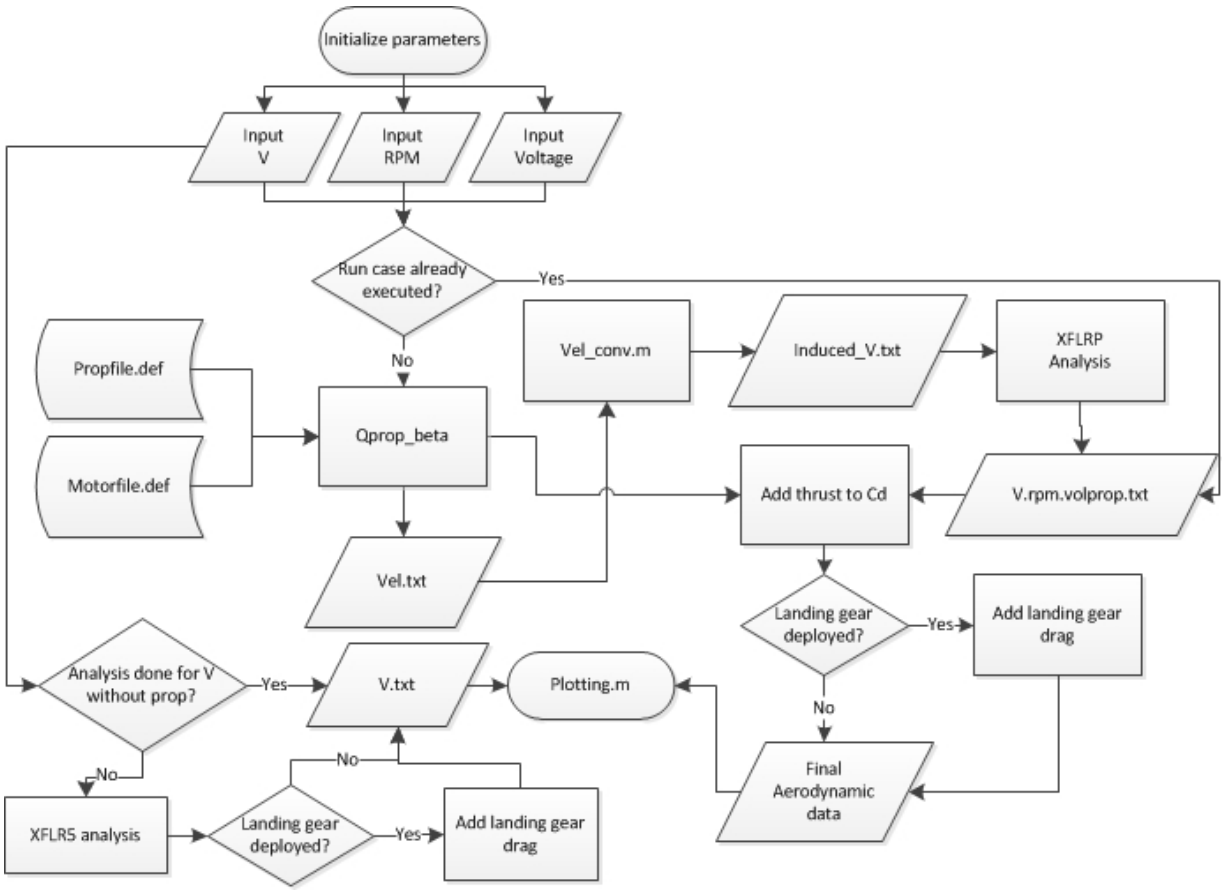

Figure 4.4: Flowchart of the aerodynamic analysis model.

chosen. As the chord at the root is exactly 1m, an airfoil with a minimum 12% thickness is considered. The pitching moment should be small and preferably negative. Though it has a negative contribution to the lift, the C-wings are more effective when a negative lift is produced. This is based on a technical report of Stanford University [10]. This was checked in XFLR5 by giving the horizontal stabilizer an incidence angle of 8° at first, followed by −8°. This decreased the induced drag by 30%, these numbers cannot be considered accurate but it qualitatively confirms the aforementioned statement. Another aspect is the stall characteristic of the airfoil. A high stall angle and $C_{L_{max}}$ are desirable. This is necessary to maintain steep sustained descent. The last point is the cruise efficiency, which is reflected in the lift to drag ratio. This is an important factor and is therefore given a large weighing factor. The analysis was done at the Reynolds number for cruise $(1.5 \cdot 10^6)$, later at the Reynolds number for takeoff $(1.1 \cdot 10^6)$ is analysed, this is calculated with a root chord of 1m.

In table 4.1 a selection of airfoils is made and their properties are shown. The selected airfoils are all comparable to the NACA22112 which was chosen in de midterm phase. To select the best option, a trade-off should be made, weights are added to the criteria and a qualitative trade-off is made in table 4.2. There it becomes clear that the NACA22112 has the largest score, followed by the NACA23112 and the ClarkY airfoil in third place.

Table 4.1: Airfoil selection overview ($Re = 1.5 \cdot 10^6$).

	12% Joukowski	Clark Y	Goe 429	NACA 23112
L/D	89.0	125.5	77.0	111.0
Stall angle [°]	15.0	16.0	12.5	16.0
$C_{L_{max}}$	1.53	1.62	1.30	1.60
C_m at cruise α	0.0018	-0.060	-0.0010	-0.008
Thickness [%]	12%	11.7%	11.4%	12%
	Eppler 330	N6412mb-il	Bacxx-il	NACA22112
L/D	100.0	108.0	98.0	103
Stall angle [°]	14.0	16.0	15.0	17
$C_{L_{max}}$	1.35	1.47	1.52	1.65
C_m at cruise α	0.054	-0.031	-0.042	-0.0013
Thickness [%]	11%	12%	11%	12%

Table 4.2: Airfoil trade-off ($Re = 1.5 \cdot 10^6$).

	Weights	12% Joukowski	Clark Y	Goe 429	NACA 23112
L/D	4	-	++	–	+
Stall angle	5	+	-	0	+
$C_{L_{max}}$	4	+	++	–	++
$C_m at cruise \alpha$	3	0	–	++	0
Thickness [%]	1	+	0	-	+
	Score:	1	15	-16	18
	Weights	Eppler 330	N6412mb-il	Bacxx-il	NACA22112
L/D	4	0	+	0	+
Stall angle	5	0	+	0	++
$C_{L_{max}}$	4	-	0	+	+
$C_m at cruise \alpha$	3	–	-	-	++
Thickness [%]	1	-	+	-	+
	Score:	-11	10	0	25

3D Analysis

To assure the right airfoil is chosen, their effect on the 3D aircraft is considered. When implementing the airfoils in the 3D planform model some differences emerge. For example, in the 2D case the NACA23112 has a slightly larger L/D ratio compared to the NACA22112. Though in the 3D case the NACA22112 has a 3% lower L/D compared to the NACA23112. Also the moment curves have to be reconsidered. These are shifted upward and their slope is changed compared to the 2D model. Because of these changes, one cannot purely decide using the 2D analysis alone. Special attention has to be paid to the aerodynamic moments in the 3D case since these have a strong impact on trim drag. From figure 4.5b one can see maximum L/D is obtained at an AoA of 2° for the Clark Y airfoil. This will be the cruise AoA because this is the most efficient configuration. Therefore also the C-wings need their maximum effectiveness, which is only possible with a negative lift contribution. When looking at the $C_m - \alpha$ plot in figure 4.5a for an AoA of 2, one can observe that the moment coefficient of the Clark Y airfoil is slightly negative. This can be compensated by a down force of the horizontal part of the C-wing, which is not likely to affect the overall lift generation considerably. This is not the

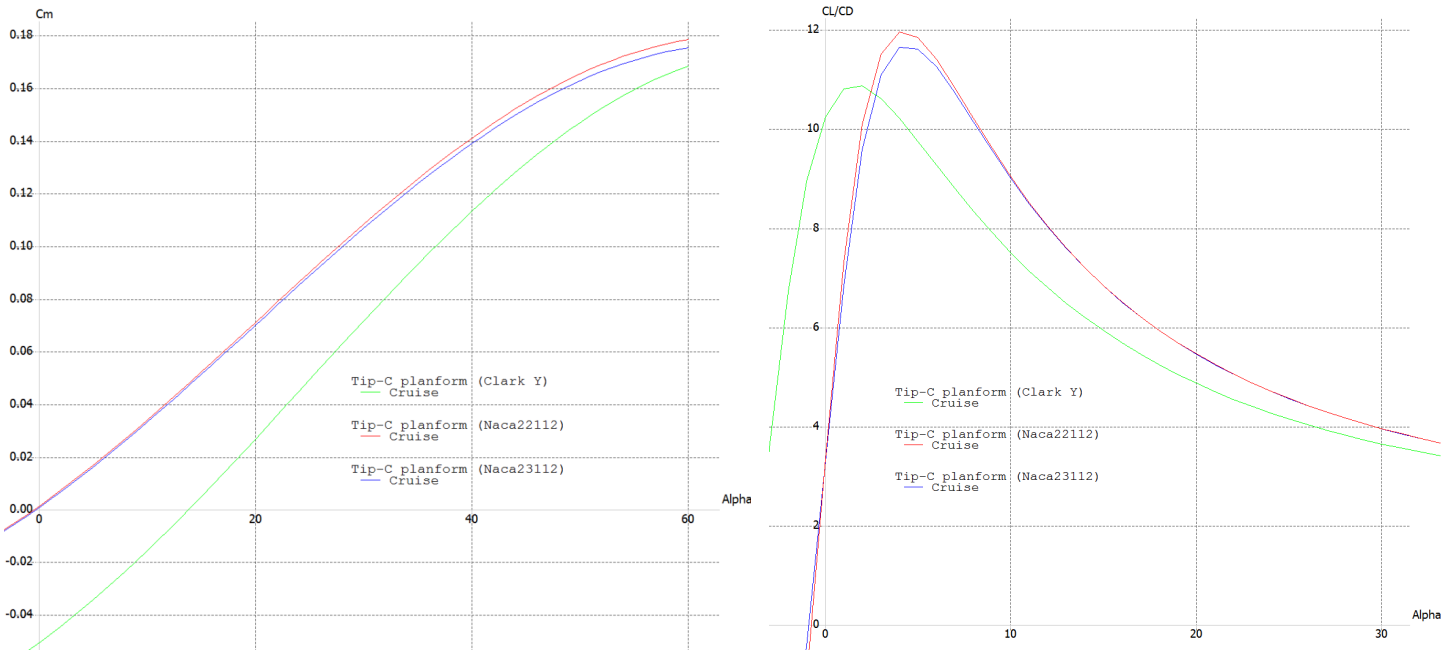

(a) $C_m - \alpha$ (b) $C_L - C_D$

Figure 4.5: Tip-C planform data with different airfoils.

case for the NACA22112 and NACA23112 airfoil since these have their maximum L/D at 4°, which corresponds to a C_m of 0.015. Though this moment is small, the tail should create positive lift which lessens the C-wing effect. Also the $C_{L_{cruise}}$ for these airfoils is lower compared to the Clark Y airfoil (0.13 vs. 0.16).

From the above reasoning one can see that the Clark Y is most suitable for this UAV. Though its maximum L/D is slightly lower, its favourable moment properties and slightly larger $C_{L_{cruise}}$ make this suitable for the aircraft.

4.4.2 Propeller Effects on Wing

Before adding a tail, first the effect of the propeller on the planform aerodynamic characteristics is investigated. In figure 4.6a the $C_L - \alpha$ graph for different propeller speeds is researched. Note that the propeller speed specified by the propulsion department is 5900RPM. One can see that adding the propeller improves the $C_{L_{max}}$. Stall angles are not affected significantly by adding a propeller, these range from 34° without propeller, to 36° with the propeller at 5900RPM. It can be observed at lower angles of attack that increasing the RPM yields higher C_L values for a fixed AoA. This is logical since higher rotational motion produces a larger induced velocity, which increases the local AoA. When looking at higher angles of attack, one sees that the opposite effect occurs. This can be explained by the fact that the local AoA exceeds the stall angle due to the large upwash created by a faster spinning propeller. When operating in this regime, lower C_L values occur for higher RPM. As the propeller configuration counteracts the vortex, a decrease in induced drag is present. According to the drag polar of figure 4.6b, drag increases with RPM. This is probably due to the high induced velocities, which means flow conditions near stall are applicable. One can see small drag reduction w.r.t. the propellerless configuration. This only occurs below 5000RPM, then the counteracting vortex has the largest effect. It is suspected that at larger RPM values, the effect of the propeller is overcompensated

which creates a vortex the other way. It becomes clear that the specified 5900RPM configuration does not always follow the trends described above. Therefore a thorough CFD analysis should be done to check for it's accuracy.

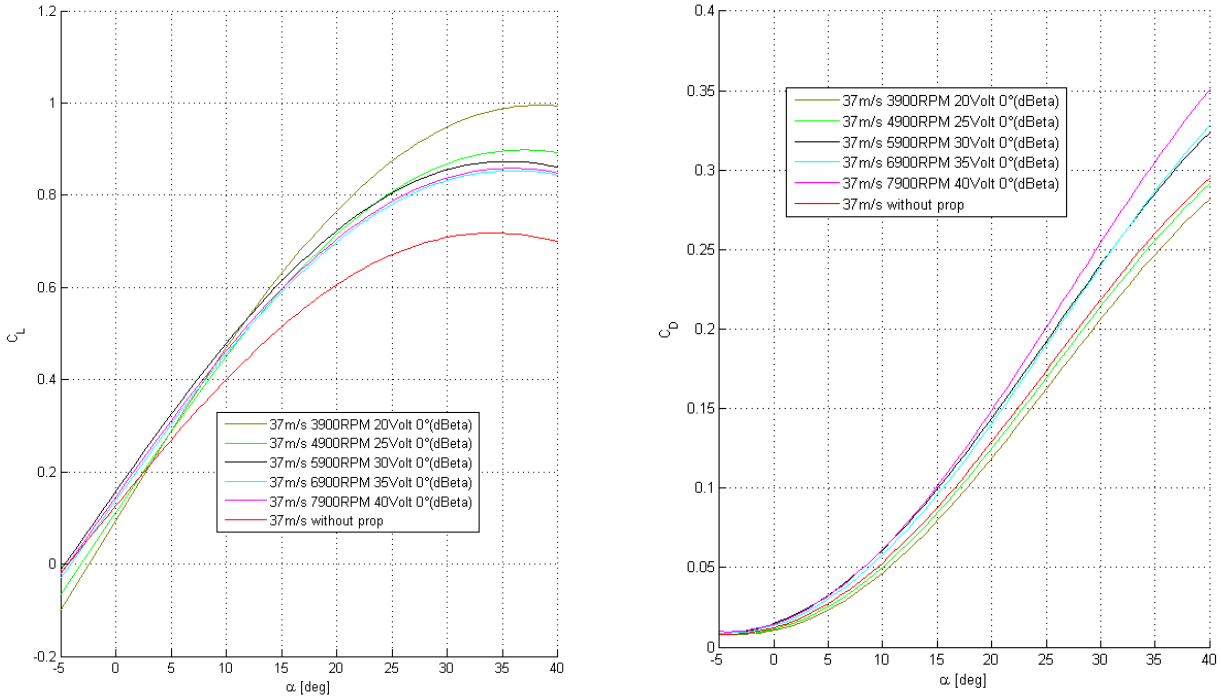

(a) $C_L - \alpha$ (b) $C_D - \alpha$

Figure 4.6: Aerodynamic performance with varying RPM.

Increasing the airspeed should have the opposite effect of increasing the RPM. For higher speeds the effective AoA is smaller and consequently also the induced velocities are smaller which means the C_L values should be lower. From figure 4.7a it becomes clear that the above is only valid for lower angles of attack. When looking at the higher AoA region, higher C_L values for higher flight speeds are obtained. This is probably to the expected fierce slipstream deformation by the body at high angles of attack. As this interaction is neglected here, again an extended CFD analysis should be done to confirm the above statements.

4.4.3 Planform Shape Analysis

In the midterm report [9] the planform was chosen based on a meeting with Dr. ir. L.L.M. Veldhuis (from TU Delft Aerodynamics department). This planform would not be optimal in clean configuration. However when the propeller slipstream is added, some aerodynamic advantage should occur. The above statement is now researched with the aerodynamic model which simulates the propeller flow on the wing. A code was written to describe the geometry of the aircraft. This includes the location of the section, the chord of that section, and the offset from the reference point. These properties can be directly put in the xflrP model. The analysis was done for the 5900 RPM case prescribed by the propulsion department and the cruise speed found before, which is 37m/s. The

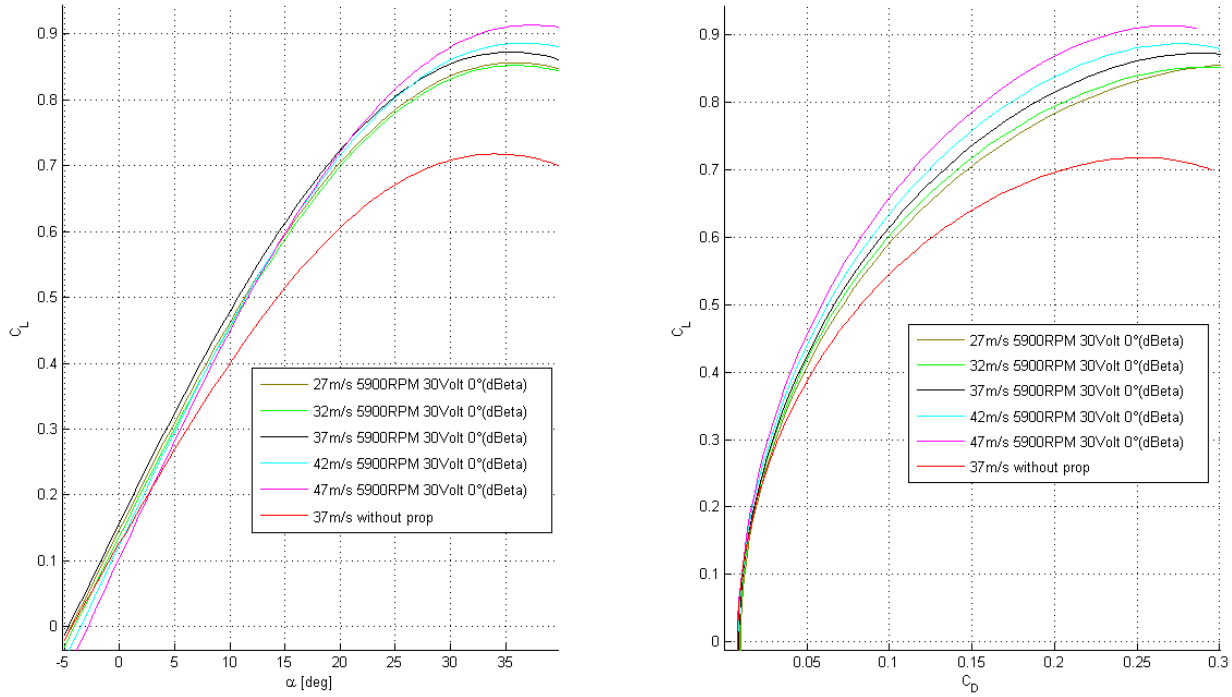

(a) $C_L - \alpha$ (b) $C_L - C_D$

Figure 4.7: Aerodynamic performance with varying speed.

results can be seen in figure 4.8a,4.8b and 4.8c. An inverted plaster, a plaster and a square planform with the same mean aerodynamic chord and span, hence the same AR are analysed. For the plaster and inverted plaster the difference between tip chord and root chord was taken constant.

From figure 4.8a it becomes clear that the inverted planform has the lowest $C_{L_{max}}$ values with 0.72. The square planform is larger with 0.83 and the plaster is slightly better. One would not expect stall angles to be so high (36°). Therefore wind tunnel results for different planform shapes are sought. In [11] wind tunnel tests on a model of the XF5U-1 aircraft are described. Reynolds numbers are in the same range as the current range so this comparison can be assumed valid. The stall angle of the XF5U-1 model is 34° which is in the same range as the stall angles of Tip-C. As no advantage in $C_{L_{max}}$ nor in $C_L - \alpha$ is found, a quick look to the L/D graph from figure 4.8b. It becomes clear that the inverted plaster planform has a slightly higher L/D (7%) compared to the other two planforms. The real advantage is found in the $C_m - \alpha$ plot of figure 4.8c. This is because the trimmed condition is reached at a lower α, which is preferable since cruising at higher angles of attack creates more drag. By adding the tail, this plot is further shifted to the left. But by choosing this planform, the effect of the tail can be smaller which generally means less trim drag is created. This together with the higher L/D makes the inverted planform a good planform shape for Tip-C.

4.4.4 Planform Optimisation

The current cruise speed of 37 m/s was obtained using iterations of the planform. The initial goal was a 30 m/s cruise speed but the C_L values at optimal cruise conditions were to low. With the planform at that time, a cruise speed of 43 m/s is needed to maintain vertical equilibrium. At

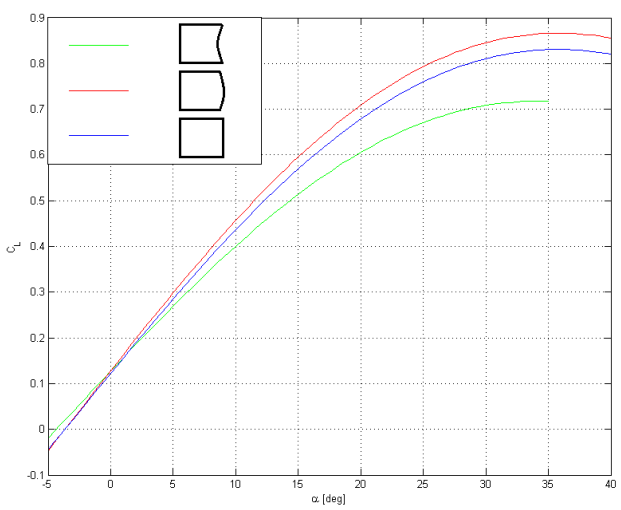

(a) $C_L - \alpha$

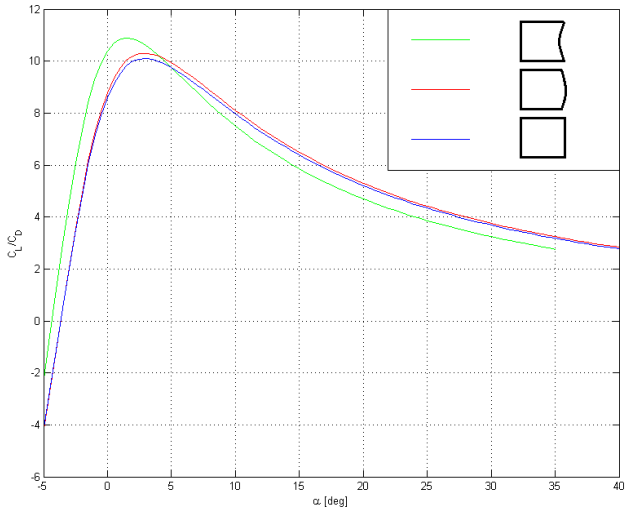

(b) $C_L/C_D - \alpha$

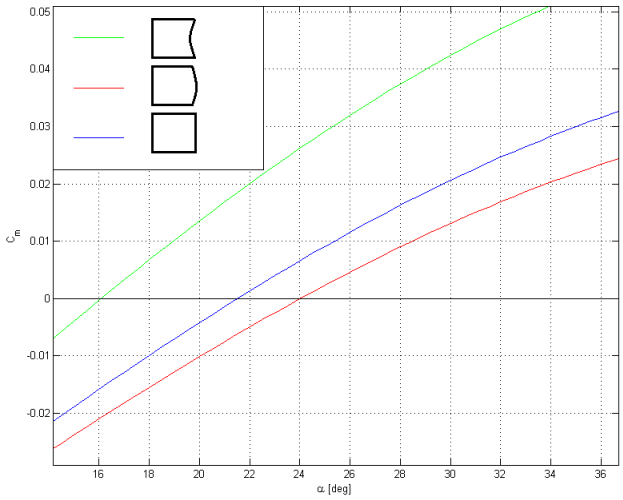

(c) $C_m - \alpha$

Figure 4.8: Tip-C planform data analysis with propeller installed.

this speed, the propeller pitch will be too high. That means the tip of the propeller will stall too early. To lower the cruise speed, one can increase the surface area, or increase the $C_{L_{cruise}}$. The latter can be achieved by increasing the AR since it increases the lift slope. After iterating the planform dimensions, an AR of 1.06 and a span of 1.1045 m was obtained. With this configuration the UAV can fly steadily at maximum L/D at 37 m/s.

4.4.5 Tail design

Vertical tail

The size of the vertical tail was determined by the stability and controllability department. For the aerodynamic design, the load analysis on this surface is of importance, since a negligible resultant force in cruise is desirable. As the propeller is turning inboard up (counteracting the tip vortex) a swirl is created which a has a clockwise motion looking from the front on the right wingtip. In figure

4.9 this swirl is plotted using the induced velocities from Qprop. These induced velocities create a dynamic pressure on the area of the fin. Integrating this pressure over the vertical area results in the total force of 9.38 N on the fin, acting outwards (to the right).

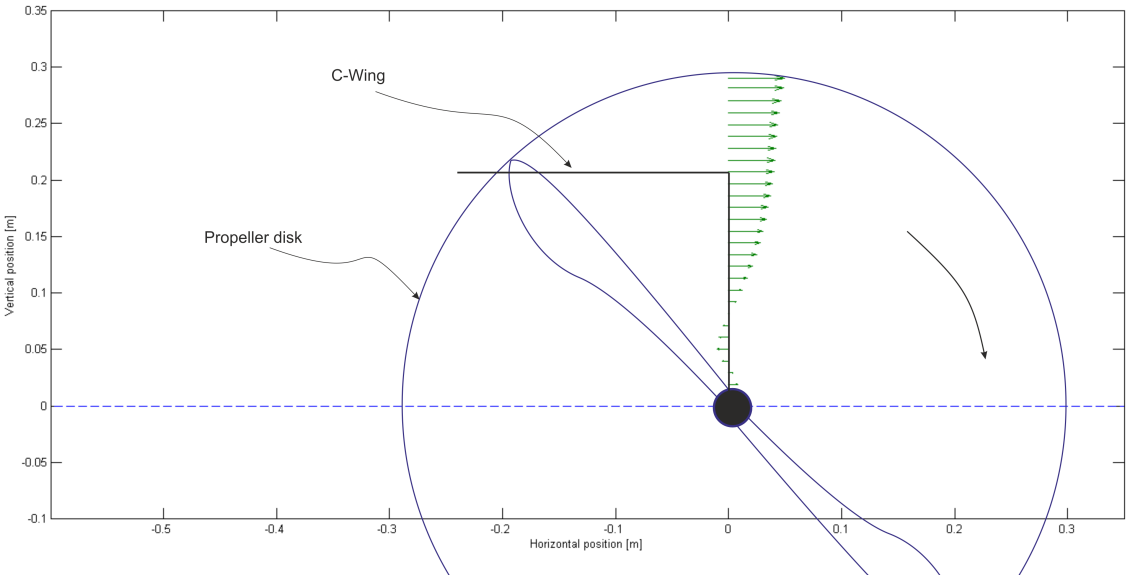

Figure 4.9: Induced velocities on vertical fin.

Note that a circular slipstream is assumed. In reality the swirl will not act within a tubular constraint since the body will deform this slipstream considerably. The slipstream shape also depends on the AoA. This means this estimation can only be used for initial sizing. To obtain a more accurate results, a thorough CFD analysis is advised.

To counteract the force calculated above, the vertical tail is given an asymmetric airfoil. Symmetric airfoils have to be placed at a rather high incidence angle and produce a larger drag accordingly. A slightly cambered airfoil with sufficient thickness for the rudder servo is the eppler 360 airfoil. When running an XFLR5 analysis on the separate tail segment, it is found that equilibrium is achieved at an incidence angle of -2 degrees. With a C_L value of 0.0139 the fin now counteracts the force generated by the propeller swirl.

Again one has to be careful with this result since the vertical and horizontal stabilizer were modelled without the body to allow C_L calculations of the tail. In reality, the body will influence the flow around the tail considerably so again a definite answer can only be given by a thorough CFD analysis. This design change is implemented by other departments in the second iteration section.

Horizontal tail

The horizontal tail sizing is mainly determined by the stability and control department but an airfoil needs to be chosen. Since a standard symmetric airfoil leads to large control surface deflections to trim the aircraft, again an asymmetric airfoil is chosen. The analysis was done with different airfoils, where the main goal was to have a small resultant moment with the least amount of drag. Just like for the vertical tail, the eppler 360 was chosen. To further decrease the deflections needed in cruise, it was placed at an incidence angle of 2°.

Aircraft analysis with tail

To estimate the final aerodynamic performance graphs the tail has to be added to the XFLR5 model. As the model cannot run with the propeller and tail installed simultaneously, the analysis of the configuration with tail and with propellers has to be run separately. In the final model the absolute difference between the planform and the tailed planform is taken and added to the planform with propellers. This yields the final aerodynamic performance graphs. This means the effect of the propeller slipstream on the tail is neglected. In figure 4.10a one can see the tail improves the C_L max of the aircraft. This was not expected since the tail produces downforce throughout the AoA range. The most likely explanation is that air is squeezed between the body and the horizontal tail, whereby the velocity is increased. Therefore the static pressure difference over the wing is increased, which increases lift. This is confirmed by the panel force distribution in XFLR5, where larger forces on the trailing edge region of the body are observed. This also causes an increase in L/D as can be seen in figure 4.10b. The tail also has a drag penalty since the viscous drag increase is much larger than the induced drag decrease. The latter is present because the vertical fins avoid vortex generation at the back of the wing. Therefore the L/D is decreased by 15.7% when adding the tail. Still the aircraft is not trimmed, with data obtained from the stability department, the change in C_L and C_D is applied to the graphs. This mainly affects the cruise performance so the L/D graph is lowered. The latter can be seen in figure 4.10b where a final L/D of 8.1 is found. This theoretical value is better than e.g. a Cessna 150 (conventional general aviation aircraft) which has an L/D of 7 [12]. From the L/D graph it also becomes clear that the cruise AoA increases to 5 degrees which corresponds to a higher C_L value. This means one can fly at a slightly lower cruise speed. So iterating the whole process is necessary to come up with better estimates.

Comparison other tails

In section 4.1 the advantages for C-wings were described. To check these, the model was run with a Prandtl wing as well (closing the C-wing). The propeller was neglected for simplicity. To have a fair comparison the incidence angle of the Prandtl wing was chosen such that the same contribution to the moment was obtained. However it is not possible to match the slope and the C_{m_0} closely since the lift distribution is very different from the C-wings. From this analysis it becomes clear that one can not state which one is better. A extensive trade-off and further CFD analysis should be done to check the advantage of the Prandtl wing configuration.

4.5 Sensitivity analysis

In order to know which parameters affect the aerodynamic properties the most, a small sensitivity analysis is done. As mentioned, an aircraft configuration change would mean a complete iteration of the analysis. For example, if a Prandtl wing is chosen, the planform moment would not be so important for the airfoil selection since the the bigger tail would create a larger force. Another airfoil means other 2D aerodynamic properties, which means the whole analysis has to be re done. Other parameters are inputs from the performance department for example. It dictates the required surface area, to achieve the chosen wing loading. It is likely that airfoil selection remains the same, but C_L will be larger. This means lower cruise speeds are achieved, which affects the tip mounted propeller effect. So the process has to be iterated.

4.6 Recommendations

This conceptual aerodynamic analysis is not conclusive. Therefore recommendations are done to further improve the design. It became clear through the investigation that the cruise AoA became

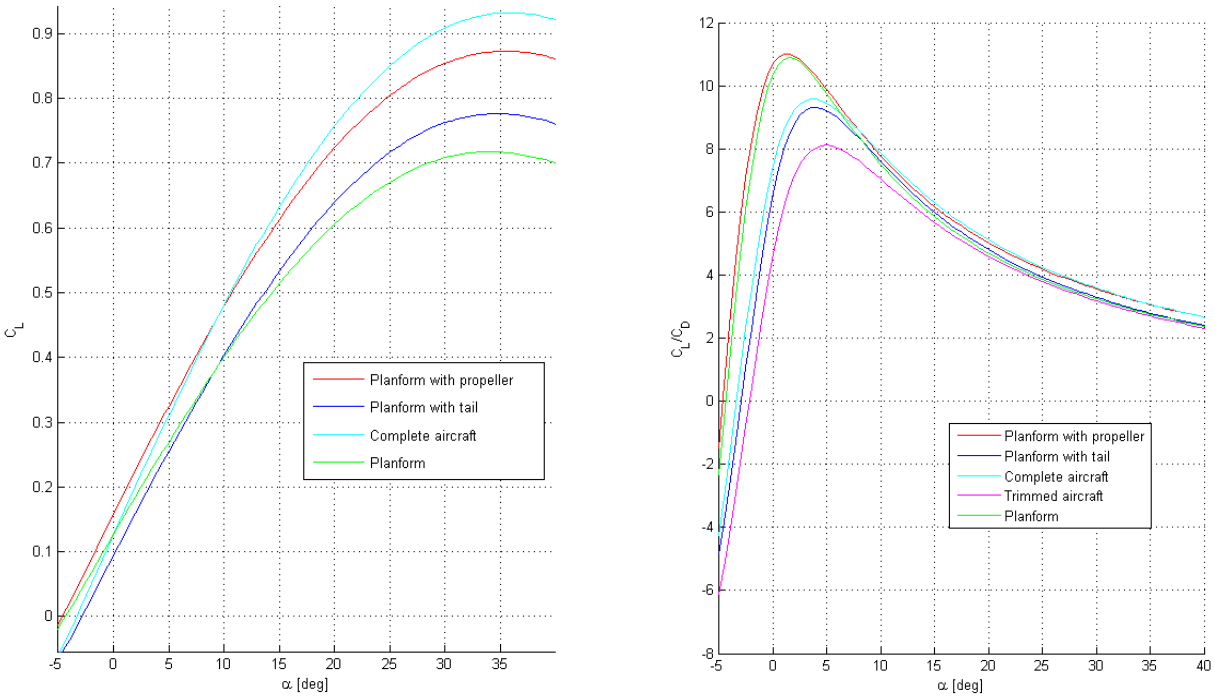

(a) $C_L - \alpha$ (b) $C_L/C_D - \alpha$

Figure 4.10: Aerodynamic performance with tail.

larger, which means cruise speeds can be lowered. This will increase the thrust as shown in 4.4.2. This means another iteration has to be done to get the updated data. Since many simplifications were made, verification and validation procedures should be executed. The numerical tools used have their own weaknesses as described in section 4.2.1. Verifying the developed model is possible by a thorough CFD analysis, which uses a 3D panel method instead of VLM. It is very likely that drag values are underestimated. Also the results near the stall angle are very doubtful. A careful analysis on the body wake should be done in this configuration to ensure the tail surfaces still function during stall conditions. As explained in 4.4.5 there are also uncertainties about the C-wings. A better aerodynamic model of this configuration should be able to predict if it has better performance than the Prandtl wing. Although by using the closed configuration, an innovative feature of the UAV is lost. It is also advised to validate the above results by wind tunnel tests. Experiments can be done on a scale model of the planform with tail, ideally with a propeller installed. By doing this, uncertainties regarding the propwash effect, load distribution and stall characteristics can be narrowed.

5 Stability

In this chapter, the longitudinal and lateral stability of the aircraft is analysed. The stability of an aircraft is very important as it determines if the aircraft is feasible in flight. Hence, the stability analysis is done extensively and as accurately as possible to ensure that the design is indeed feasible. The stability of the aircraft is mainly maintained by the C-wing, which is swept back to form a tail. The vertical part of the C-wing acts as the vertical stabiliser and the horizontal part as the horizontal stabiliser. Two separate software, Tornado and Athena Vortex Lattice (AVL), are used in the analysis. These software takes the aircraft geometry and flight conditions in as input and uses vortex lattice methods to obtain the stability and control derivatives. These derivatives are then put into a MATLAB model which gives a pulse control surface deflection inputs of $-0.25°$ for one second in symmetric motions and half a second for asymmetric motions. For symmetric motions, the elevators are deflected and for asymmetric motions, the ailerons and rudders are deflected. This is to simulate a gust that the UAV may meet during flight. The MATLAB model calculates the eigenvalues and plots the eigenmotions from the state space matrices. From the eigenvalues and motions a conclusion can be made about the stability of the design.

5.1 Initial Design

The original tail design is taken from the Mid-Term Report. These are the dimensions defined in the conceptual design phase. The stability of this design is first analysed before changes are implemented. The dimensions are defined in table 5.1.

5.2 Iterations

To get from the initial geometry of Tip-C to the final design, a lot of iterations are performed. If the new geometry makes the aircraft more stable it can stay, but if it makes it less stable or even unstable, the change in geometry is discarded. Table 5.1 summarises the intermediate steps taken. At the top the geometry of the initial design is given. Below that, are all iterations. For each iteration, the parameter(s) that change are displayed in a white cell and the parameter(s) that stay constant in a grey cell.

After each horizontal black line between some of the iterations, an important or bigger step is taken towards the final design. One of the most important parameters changed is the vertical tail sweep. This parameter is displayed as x_h, which is the distance between the vertical tail root LE and vertical tail tip LE. As the vertical tail sweep increases, so does x_h, which means the horizontal tail moves backward. This makes the horizontal tail more effective, since its moment arm is larger. The downside is that the vertical tail has a larger sweep angle, which makes it less effective. There is a trade-off between increased horizontal tail performance for symmetric stability and vertical tail performance for asymmetric stability. $x_h = 0.375$ m is chosen for the final design.

Table 5.1: Iteration steps taken to arrive at the final design. Changing parameters in white, constant parameters in grey.

#	Iteration change / Dimensions	[m] cv_root	[m] cv_tip	[m] bv	[m] ch_root	[m] ch_tip	[m] bh	[m] xh	[deg] ih	[m] x_cg	Airfoil	[m] cw_root	[m] cw_tip	[m] bw	[m] c_a	[m] b_a	[m] c_e	[m] b_e	[m] c_r	[m] b_r
1	Initial geometry (from Mid-Term Report)	0.22	0.15	0.22	0.15	0.15	0.45	0.395	0	0.3	NACA0012	1	1.1	1.1045	0.20202	0.13825	0.054	0.37	0.09	0.14
2	Increase main wing AR											0.85	0.91	1.4	0.20202	0.13825	0.054	0.37	0.09	0.14
3	Change main wing AR back again											1	1.1	1.1045						
4	Increase tail chords, V-tail sweep and move c.g. forward	0.3	0.2		0.2	0.2		0.575		0.29										
5	Decrease H-tail span and increase V-tail sweep						0.35	0.675												
6	Update control surface sizes (from Xueying) and decrease V-tail sweep							0.375									0.05	0.28		
7	Increase V-tail sweep							0.475												
8	Increase V-tail sweep							0.575												
9	Increase H-tail chord (forward)		0.25		0.25	0.25		0.525												
10	Increase H-tail chord (backward)		0.25		0.25	0.25		0.575												
11	Increase V-tail span			0.3																
12	Experiment with closed C-wing (O-wing)	0.3	0.2	0.22	0.2	0.2	0.55225	0.375	0	0.29	NACA0012	1	1.1	1.1045	0.20202	0.13825	0.05	0.28	0.09	0.14
13	Increase V-tail sweep							0.475												
14	Increase V-tail sweep							0.575												
15	Move back to iteration 6 but add an incidence angle to H-tail	0.3	0.2	0.22	0.2	0.2	0.35	0.375	-2	0.29	NACA0012	1	1.1	1.1045	0.20202	0.13825	0.05	0.28	0.09	0.14
16	Increase V-tail sweep							0.475												
17	Increase V-tail sweep							0.575												
18	Increase H-tail incidence angle and decrease V-tail sweep again							0.375	-3											
19	Increase H-tail incidence angle								-4											
20	Iteration 15 but increase V-tail sweep							0.675	-2											
21	Iteration 17 but increase H-tail chord		0.25		0.25	0.25		0.575												
22	Move back to iteration 6 but increase H-tail chord and decrease span	0.3	0.27	0.22	0.27	0.27	0.3	0.375	0	0.29	NACA0012	1	1.1	1.1045	0.20202	0.13825	0.05	0.28	0.09	0.14
23	Change the tail airfoil										NACA0016									
24	Add taper to the H-tail					0.17														
25	Add 18.4° sweep to the H-tail					0.27														
26	iteration 22 but change tail airfoil (H-tail inverted)	0.3	0.27	0.22	0.27	0.27	0.3	0.375	0	0.29	Eppler 360	1	1.1	1.1045	0.20202	0.13825	0.05	0.28	0.09	0.14
27	Update control surface sizes (from Martijn)														0.15	0.25	0.1	0.25	0.1	0.25
FINAL	iteration 22 but change tail airfoil	0.3	0.27	0.22	0.27	0.27	0.3	0.375	0	0.29	Eppler 360	1	1.1	1.1045	0.15	0.25	0.1	0.25	0.09	0.14

AVL uses the camber line of the airfoil to analyse the stability. Since NACA0012 and NACA0016 are both symmetric airfoils with a straight camber line, the stability analysis for AVL does not change at all when changing the airfoil. From Tornado however, it follows that symmetric stability increases slightly when using NACA0016.

The airfoil of both the horizontal tail and vertical tail is changed once more to Eppler 360, which is a requirement from the aerodynamics department. The reason to use this airfoil is explained in section 4.4.5. This new airfoil positively influences both symmetric and asymmetric stability, since the forces created by this airfoil are larger. This makes the tail more effective and smaller control surface deflections are required to trim the aircraft.

For iteration 22, the horizontal tail geometry drastically changes; the span decreases and the chord increases. This is done, because the servos for the elevator did not fit. Increasing the chord gives a larger maximum thickness. So the decision is a necessary step for the systems department. After that, the airfoil is changed to NACA0016 to increase the thickness even more.

5.2.1 Final Design

After the rounds of iteration, the design is optimised for best stability with the least negative influence on the other departments of the group. The final design configuration can also be found in table 5.1.

At the same time, the airfoil chosen for the horizontal tail and vertical tail is the Eppler 360. For the horizontal tail, the airfoil is inverted to create the necessary down force for maximum efficiency of the C-wing. The horizontal tail also have a -2° incidence angle for the same reason while the vertical tail has a 2° toe-in angle to counteract the side forces acting on the vertical tails due the propeller slipstream. A more detailed explanation for this phenomenon is given in Chapter 4.

In the next section, the stability characteristics of the final design in different flight conditions are analysed. The flight conditions are defined for the flight phases that the UAV will go through. These are: takeoff, climb rate, climb gradient, cruise, descent, and landing. The UAV is analysed for both longitudinal and lateral stability in each flight phase and it is important that it is stable for each of these phases.

In the analysis, the propeller is not implemented in the model as this is not possible in either Tornado or AVL. Hence the analysis is done for just the body with tail and the effect of propeller interaction with the tail is considered separately in section 5.5. Similarly, the 2° toe-in angle on the vertical tail is also not implemented in the model in Tornado and AVL when analysing the stability and control derivatives as the software is unable to define the geometry smoothly with the incidence angle on the horizontal tail and the toe-in angle on the vertical tail. Hence, a separate analysis is for the toe-in angle to see how implementing it can possibly affect the stability. This can be found in section 5.4

5.3 Final Design Stability Characteristics

In this section, the stability for each of the flight phases is analysed. In the software Tornado and AVL, the geometry is entered as input and the design is set to trim for a certain elevator deflection at the stated flight condition. The stability and control derivatives are then found and set as input for the stability model in MATLAB. The response of the eigenmotions are plotted and shown for each flight phase. For the symmetric motions, the response of V and AoA are shown in the left column. For asymmetric motions, the response of the roll rate and roll angle are plotted in the middle column and the response of the yaw rate and yaw angle are plotted in the right column.

Takeoff and landing with crosswind is considered but it is realised that Tornado is unable to trim the aircraft in asymmetric flight conditions. AVL is able the trim the aircraft but only with control surface deflections. This is not the case in real flight since in real flight, the aircraft is able to trim with both control surface deflections and change in wing incidence angle. Also due to the inaccuracy of AVL, as explained in section 5.6, it is decided that an analysis on crosswind situation is too inaccurate with the software available.

5.3.1 Takeoff

For takeoff, the UAV goes through a series of different flight conditions from the beginning of the air borne phase to the start of the climb phase. The UAV first starts with the ground run and rotates around the main landing gear to go into the air borne phase. The flight condition at the start of the air borne phase is:

- V $= 14m/s$
- $\alpha = 15^\circ$

After the UAV is in the air, it will continue increasing AoA and V until it reaches the velocity needed for maximum climb gradient. The flight condition at this instant is:

- V $= 20m/s$
- $\alpha = 30°$

The UAV will only be analysed for stability under these two extreme conditions for takeoff. The response of the UAV under the first flight condition can be seen in figure 5.1.

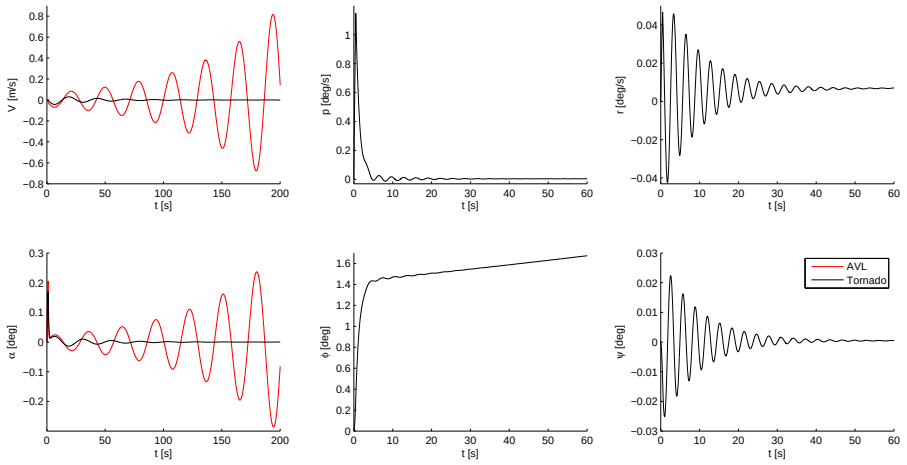

Figure 5.1: Response curves for a pulse control deflection of $-0.25°$ for takeoff

In the figure, the results for AVL are only shown for the symmetric motion as the results for AVL are neither accurate nor reliable at high AoAs. The inaccuracy is explained in detail in section 5.6. The symmetric AVL results are plotted with the Tornado results to show the difference. From the V and AoA plots, it can be seen that Tornado results in a stable aircraft while the AVL plots show that the aircraft is unstable. The time to double amplitude for the AVL results is 52.6 seconds which is still acceptable as the pilot has enough time to stabilise the UAV. After 200 seconds, the peak change in V is only $0.8m/s$ and the change in AoA is only $0.3°$ which shows that the UAV is still acceptably unstable. For the Tornado results, the starting response is similar to that of AVL, for both V and AoA, but the response damps out. It takes around 190 second for the phugoid to damp out fully but the change with V and AoA is extremely small within the period, with the peak deviation in V being $0.03m/s$ and the peak deviation in AoA being around $0.02°$

The asymmetric response can be seen in the plots for roll and yaw in figure 5.1. The roll angle ϕ shows that the UAV is unstable in spiral as the ϕ increases after the initial deflection. For the second flight condition analysed in takeoff, the results are plotted in figure 5.2.

In this condition, AVL is unable to trim the aircraft due to the limitations at high AoAs. Hence, only Tornado results are shown. It can be seen that the symmetric motion is stable, as the oscillations damp out. The peak change in V and AoA are also not large, with peak change in V to be $-0.052m/s$ and peak change in AoA to be $0.08371°$. For the asymmetric case, the oscillations in roll and yaw damp out but they continue to increase aperiodically. From the eigenvalues shown in table 5.2, it can be seen that the Dutch roll and aperiodic roll are stable but the spiral is unstable. The time to double amplitude in this case is computed to be approximately 32.3 seconds which is still acceptable for the pilot to stabilise the aircraft again. The change in roll and yaw angles are also not extremely

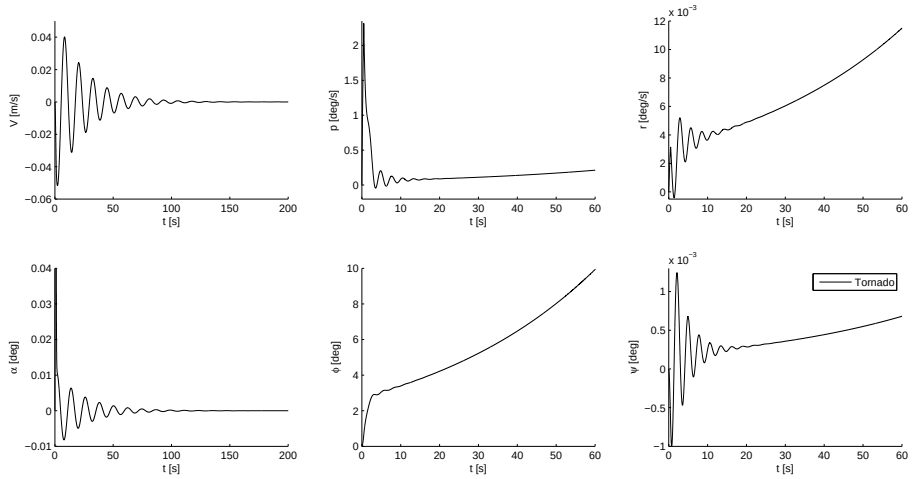

Figure 5.2: Response curves for a pulse control deflection of $-0.25°$ for takeoff

Table 5.2: Eigenvalues for Asymmetric motion in Takeoff Condition 2

Dutch Roll	Aperiodic Roll	Spiral
$-0.2694 \pm 2.2296i$	-1.1855	0.0214

large until it proves difficult to stabilise. After 100 seconds, the roll angle change is 23.5° and the yaw angle change is only in the order of 10^{-4}. It should be noted however, that Tornado also suffers from inaccuracies at high AoAs so the results cannot be said to be highly accurate.

5.3.2 Climb Rate

After the takeoff phase, the UAV will proceed to climb. The condition for maximum climb rate is first analysed for the values:

- V = $22m/s$
- $\alpha = 11°$

The response of the UAV due to a small deflection in control surfaces are shown in figure 5.3. For the symmetric motions, both Tornado and AVL results show an unstable phugoid motion. The AVL results are much more unstable than the Tornado results, which can be seen from T_2 shown in table 5.3.

The T_2 and period for both results are sufficiently large so that the UAV will not be out of control within reasonable response time for the pilot. The peak change in the response is also not large. After 200 seconds, the peak change for V in AVL is $2.4m/s$ while for Tornado it is $0.273m/s$. For AoA, the peak change after 200 seconds for AVL is $-0.64°$ and for Tornado it is $-0.077°$.

Table 5.3: Time to double amplitude and period for max. climb rate

	T_2 [s]	Period [s]
Tornado	403.9	20.7
AVL	57.4	23.25

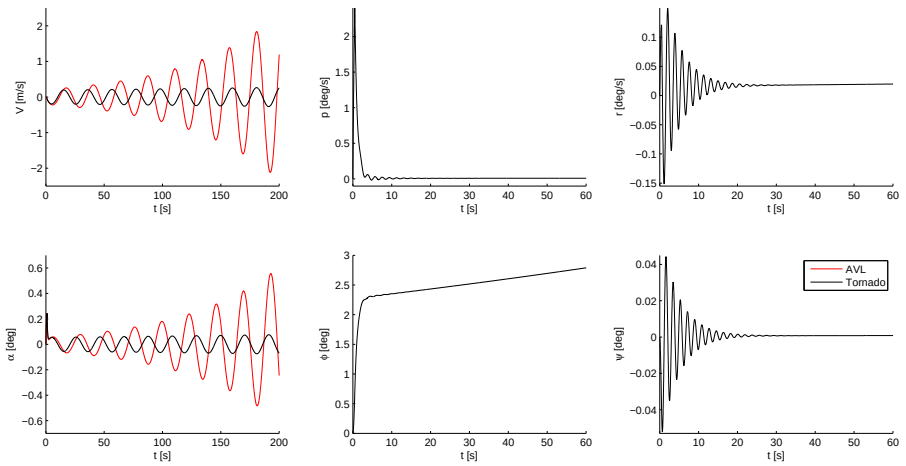

Figure 5.3: Response curves for a pulse control deflection of $-0.25°$ for maximum climb rate

Table 5.4: Eigenvalues for Asymmetric motion at max. climb rate

Dutch Roll	Aperiodic Roll	Spiral
$-0.2135 \pm 3.3998i$	-1.4626	0.0034

For asymmetric motions, only Tornado results are shown again as the AVL results are inaccurate for the high AoA. From the eigenvalues shown in table 5.4, it can be seen that the Dutch roll and aperiodic roll are stable while the spiral is unstable.

Since the eigenvalue for spiral is a very small positive value, the spiral is not unacceptably unstable. This is also reflected in the roll angle T_2 which is 202.85 seconds, where the roll angle increased from $2.4°$ to $4.8°$.

5.3.3 Climb Gradient

The maximum climb gradient condition is defined as:

- V $= 20m/s$
- $\alpha = 15°$

The response of the UAV is shown in figure 5.4. Similar to the response at maximum climb rate, the phugoid motion is unstable. The T_2 and period of the response can be seen in table 5.5. As can be seen, the T_2 for the AVL results is rather small while the T_2 is much longer. Even though T_2 is short for AVL, the deviation values for V and AoA are not large, with peak value for $V = -12.7m/s$ and $AoA = 3.75°$ after 100 seconds. Thus the UAV can still be stabilised within a reasonable amount of time. At the same time, since Tornado is more accurate at high AoAs, the results for Tornado are much more reliable, which shows that the instability is still in the acceptable range.

For the asymmetric motion, the eigenvalues are shown in table 5.6. The Dutch roll and aperiodic roll are again stable while the spiral is slightly unstable. The T_2 for the roll angle is 183.04 seconds from $2.2°$ to $4.4°$. Since the T_2 is very long and the change in roll angle rather small, the spiral instability is not a problem.

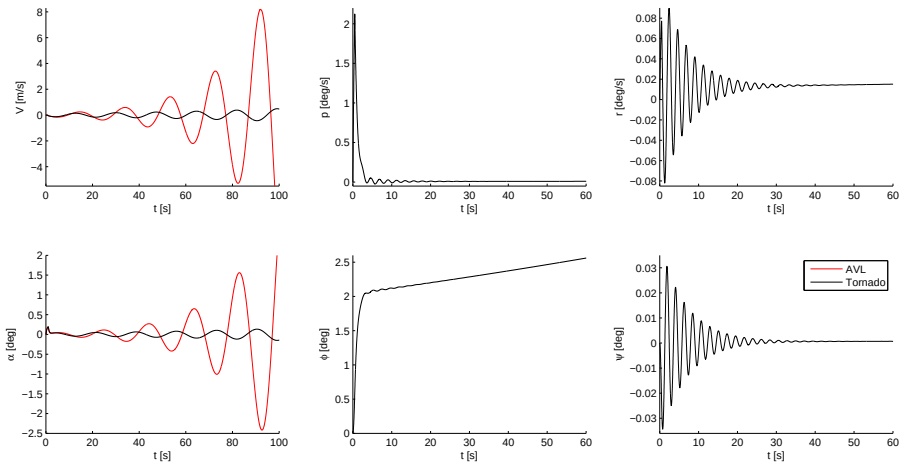

Figure 5.4: Response curves for a pulse control deflection of $-0.25°$ for maximum climb gradient

Table 5.5: Time to double amplitude and period for max. climb gradient

	T_2 [s]	Period [s]
Tornado	48.8	17.24
AVL	15.3	19.4

5.3.4 Cruise

After the UAV climbs to the desired altitude, it will be in the cruise phase. The flight condition for this phase is defined as:

- V $= 37m/s$
- $\alpha = 2°$

The response of the UAV is shown in figure 5.5. In this flight phase, both AVL and Tornado results are shown as the AoA is small, so the AVL and Tornado results should be similar. The symmetric motions are shown for up to 200 seconds as the period of one oscillation is very large. The period for both Tornado and AVL are shown in table 5.7. The time to half amplitude is also shown in the table. From these values, it can be seen that the symmetric motions damp out rather quickly with few oscillations. This is further supported by the response plots for V and AoA.

For the asymmetric motions, the eigenvalues are shown in table 5.8. Dutch roll and aperiodic roll are stable for both of the software while spiral is stable for AVL and unstable for Tornado. The peak deviation in roll angle and roll rate are much higher for Tornado than AVL, with peak roll rate of $5.255°/s$ for Tornado and $2.235°/s$ for AVL. At the same time, the oscillations for roll rate and roll angle of AVL is larger than for Tornado. This difference can be explained by the different calculation

Table 5.6: Eigenvalues for Asymmetric motion at max. climb gradient

Dutch Roll	Aperiodic Roll	Spiral
$-0.1468 \pm 2.8468i$	-1.4088	0.0038

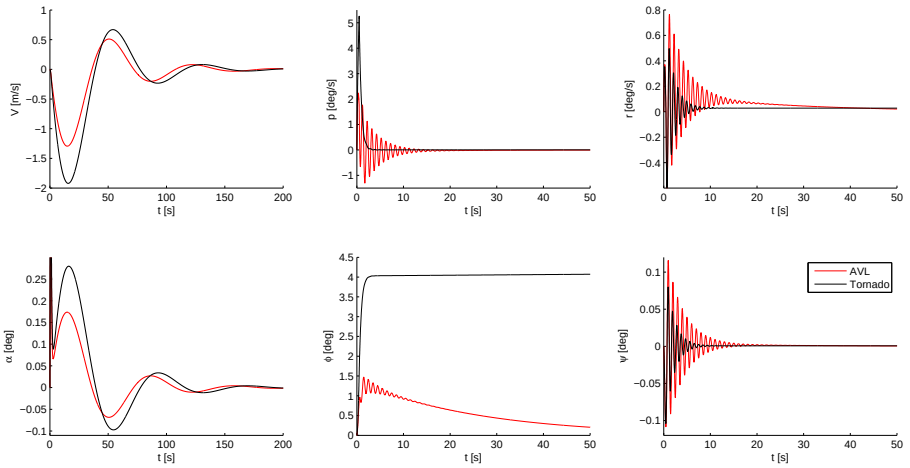

Figure 5.5: Response curves for a pulse control deflection of $-0.25°$ for cruise

Table 5.7: Time to double amplitude and period for cruise

	T_2 [s]	Period [s]
Tornado	25.3	76.7
AVL	26.7	71.5

methods used by the two software. In rolling motion, the wake of the surface has a "cork-screw" shape, which Tornado takes into account by making the trailing legs of the horseshoe vortices flexible. This phenomenon is not accounted for by AVL, hence causing the difference (see section 5.6.2)

Similar to the other flight conditions, the roll motion is only slightly unstable. Within 400 seconds, the roll angle only increases from 4.039° to 4.378°. Hence it can be concluded that in cruise, the UAV is stable.

5.3.5 Descent and Landing

For descent and landing, the flight condition is the same as for the second condition for takeoff. The flight condition is:

- V $= 20m/s$
- $\alpha = 30°$

The response plots and eigenvalues are the same as for the second flight condition of takeoff. The plots and eigenvalues can be found in figure 5.2 and table 5.2. Hence, the stability behaviour can be found in section 5.3.1.

Table 5.8: Eigenvalues for Asymmetric motion at max. climb gradient

	Dutch Roll	Aperiodic Roll	Spiral
Tornado	$-0.5684 \pm 6.7287i$	-2.1274	0.0002
AVL	$-0.2734 \pm 6.2626i$	-2.8683	-0.038

5.4 Vertical Tail Incidence Angle

The aerodynamics department added an incidence angle to the vertical tail, to cancel out the forces from the propeller wake on the vertical tail. This decision also affects stability. However, implementing the incidence angle accurately into AVL and Tornado is impossible. An incidence angle can be added, but then at the transition from vertical tail to horizontal tail, the vertical tail intersects with the horizontal tail and vice versa. This is shown in figure 5.6, which is the model used in Tornado. In the model, the intersection between the vertical- and horizontal tail as well as the gap due to this intersection can be seen clearly. This can give unexpected and inaccurate results.

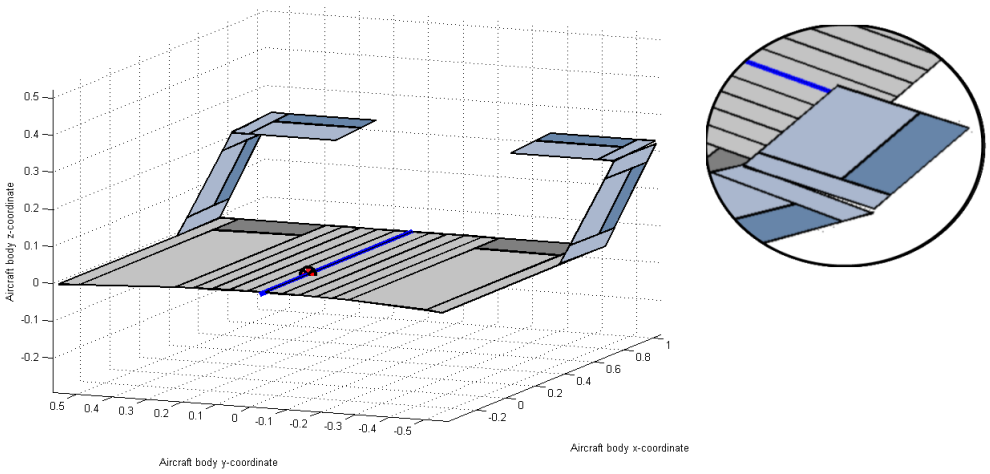

Figure 5.6: Intersection between vertical and horizontal tail due to $-2°$ incidence angle

Using this best approximation of the vertical tail incidence angle, the following results are obtained: figure 5.7 shows the results from AVL and figure 5.8 the results from Tornado, both with and without vertical tail incidence angle.

Figure 5.7 shows that, with the $2°$ incidence angle, the initial amplitude of the symmetric response of V and AoA is larger than without incidence angle. However, the motion still damps out in the same timespan, which implies the elevator to be more effective and symmetric stability is increased.

The opposite is happening for the roll and yaw responses: with incidence angle the initial amplitude is smaller, and the motion takes longer to damp out. This means the aileron and rudder are less effective and asymmetric stability is decreased.

The same can be seen in figure 5.8. Symmetric stability increases, but asymmetric stability decreases. Asymmetric stability turns out to be already sufficient from the analyses without vertical tail incidence angle. Adding the incidence angle affects it, but the asymmetric motions are still stable. However, from the analyses without vertical tail incidence it follows that the phugoid is slightly unstable for some flight phases. Adding the incidence angle improves the symmetric stability and makes the unstable flight phases stable.

Figure 5.9 gives an explanation for the fact that asymmetric motions damp out slower if the vertical tail has an incidence angle. When the aircraft is in straight flight, i.e. no sideslip, the forces created in the Y-direction by the vertical tail are equal in magnitude but in opposite direction. This means the resulting force is zero. The only difference between with and without vertical tail incidence angle is the fact that the forces created by the vertical tail with incidence angle are larger.

If the aircraft now flies with a certain positive sideslip angle β, assuming no rudder deflections, the vertical tail will have an AoA. For zero vertical tail incidence, this AoA is approximately β for both vertical tails. The left vertical tail now creates a larger inward force and the right vertical tail

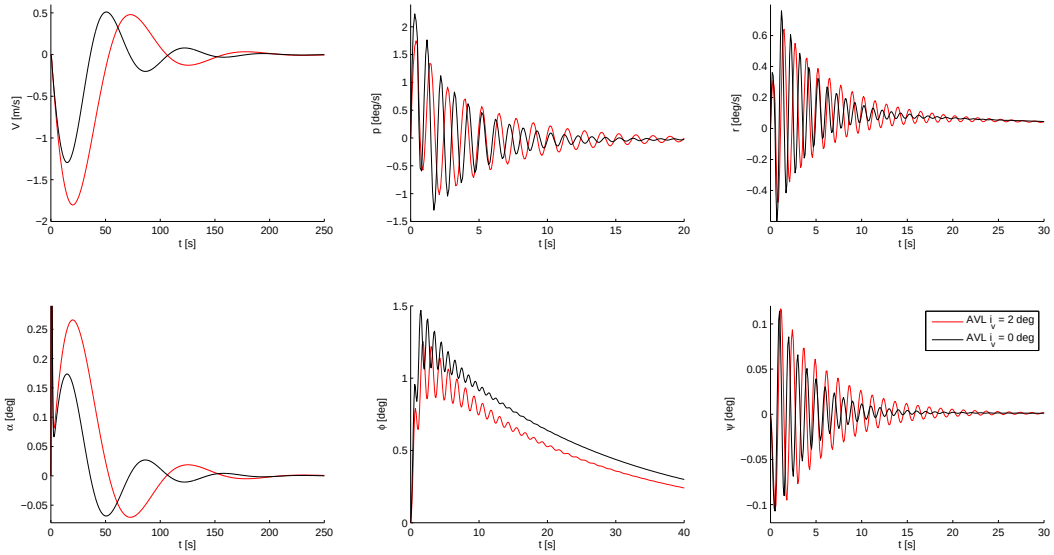

Figure 5.7: Stability characteristics of AVL both with and without 2° vertical tail incidence angle.

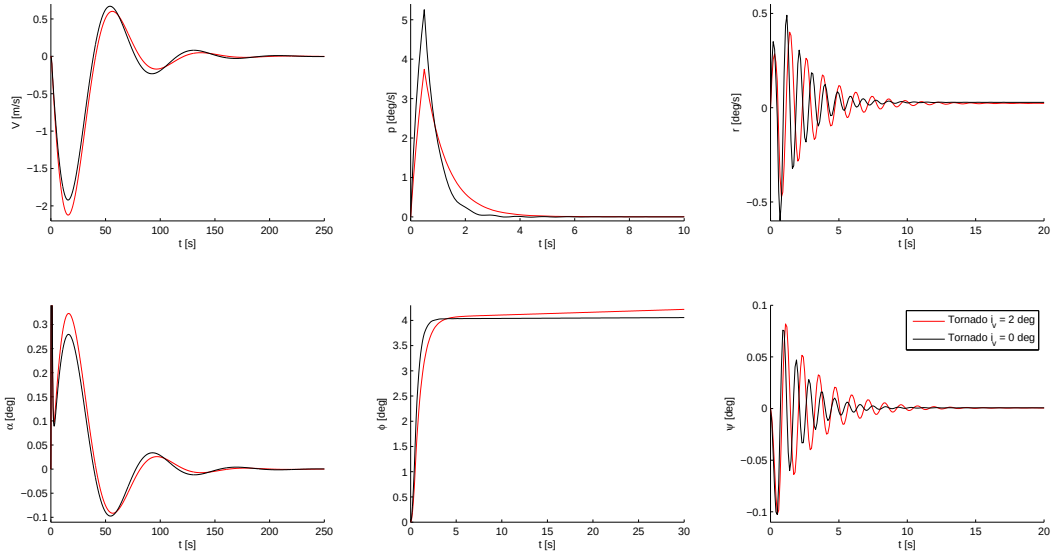

Figure 5.8: Stability characteristics of Tornado both with and without 2° vertical tail incidence angle.

creates a small outward force, due to its AoA. The resulting force in the Y-direction is now to the right, causing the aircraft to return to equilibrium, i.e. zero sideslip.

However, for a 2° vertical tail incidence angle, the resulting AoA for the left vertical tail is $+2°+\beta$ and for the right vertical tail is $-2°+\beta$. This means the left vertical tail creates a larger inward

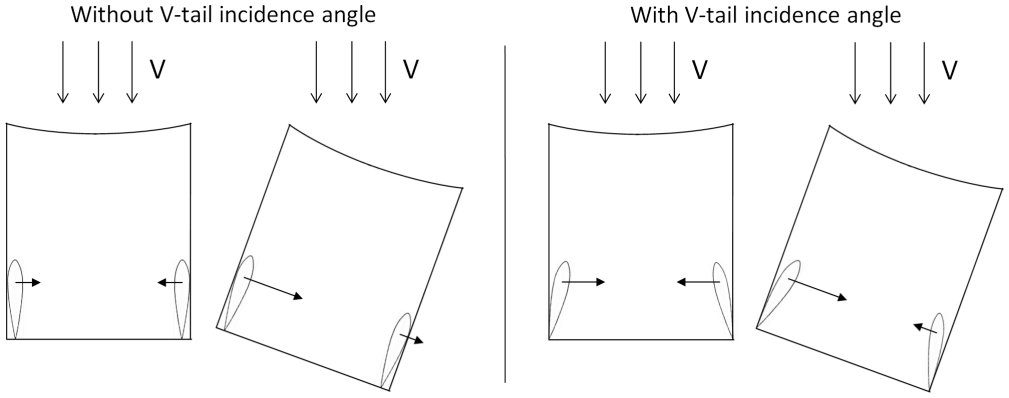

Figure 5.9: A vertical tail incidence angle makes the resulting Y-force smaller, causing the asymmetric motions to damp out slower.

force, but the right vertical tail also creates an inward force, but smaller. The resulting force for this configuration is also to the right, but is smaller than for zero vertical tail incidence angle. The aircraft also returns to equilibrium, but more slowly.

5.5 Propeller Interaction with Tail

In the stability analysis done thus far, the propellers are not implemented in the model and analysis as the software used did not support this function. However, in real flight, the propellers will have significant influence on the stability of the UAV. Hence this section is dedicated to investigate possible effects of propeller-tail interactions.

When the propellers are added, the first effect is an asymmetrical lift distribution which forms over the wings [13]. This asymmetric distribution is due to the presence of the propeller slipstream. According to Schroijen [13], "this wing-lift distribution gives rise to an asymmetrical wing trailing vortex sheet roll up which adds to the asymmetry of the flowfield." Because of this vortex sheet roll up, a sidewash is induced on the vertical fins which will increase the yaw moment. As a result, the vertical tail fins as well as the rudder should be slightly over-designed so that they are sufficient to overcome this additional yaw moment. From the yaw rate and yaw angle plots in figures 5.1, 5.2, 5.3, 5.4 and 5.5, it can be seen that the yaw angle deviations in response to a side gust is very small and the motion damps out within a short period of time. Hence even with the additional yaw moment due to the propellers, the vertical fins and rudders are expected to be sufficient in asymmetric motions.

Another destabilizing effect of the propellers is the shift in neutral point (n.p.) position due to the presence of the propellers and when there is a change in power during flight. According to Eshelby [14], the n.p. tends to shift forward with increasing C_L when the propellers are turned on. The forward shift in n.p. can be up to $3\%MAC$. This is shown in figure 5.10 [14]. In the figure, different shaft horsepower (SHP) for the propellers induces different shifts in n.p. However, the shaft power shown in the plots is very high compared to the shaft power of the UAV propellers. The combined shaft power for both engines at maximum power condition is $4400W$ which is only $5.9SHP$. Hence it can be concluded that the shift in n.p. with propellers active is not as large as stated in [14]. In figure 5.10, the n.p. shift with $38SHP$ is only approximately 1%, hence for the UAV the shift in n.p. with propellers can be taken as 0.5%. In addition, when there is a change in power during flight, there will also be a shift in n.p. by up to $2\%MAC$ [14]. Similarly, this test result is for much higher shaft power with larger increase and decrease in power, so the shift in n.p. for the UAV can be taken as approximately $1\%MAC$.

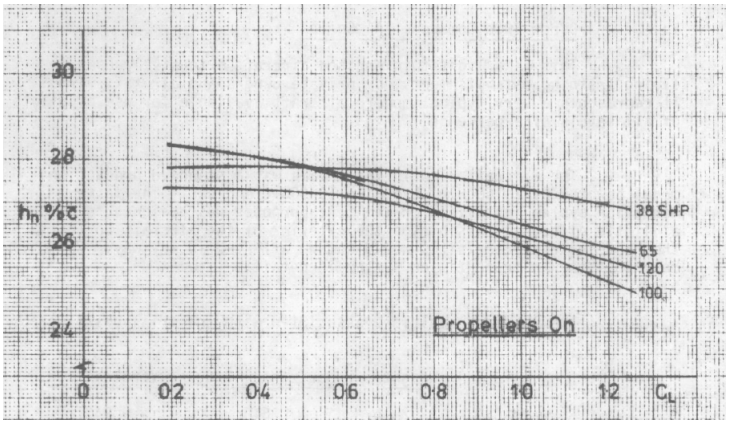

Figure 5.10: Shift in neutral point with increase in C_L

Hence, it is advisable to have a static margin (S.M.) of 1.5%MAC in order to make sure that the n.p. will not shift forward of c.g. which will cause the UAV to be statically unstable. Currently the design has a SM of 1.54% for the first design and 1.22% for the iteration. As such the current S.M. is sufficient for the first design but not so for the iteration. In order to increase the S.M., the batteries and payload location can be shifted forward to shift the c.g. forward without affecting the n.p. location. With the equation for the S.M. shown in equation 5.1 and the values for $\bar{x}_{np}$ and the S.M. given in Tornado and AVL, the optimum c.g. location for the S.M. of 0.015 should be at $0.2904m$ instead of the current $0.2917m$ for the design after iteration.

$$\bar{x}_{cg} = \bar{x}_{np} - SM \tag{5.1}$$

Besides the destabilising effects, addition of propellers also have positive effects. Due to the propeller slipstream, the dynamic pressure at the tail is higher than the free stream dynamic pressure. This is due to two factors: firstly, the propeller slipstream induces an additional velocity component in the negative x-axis and secondly, the TE of the body and the horizontal stabliser forms a duct and the flow through this "duct" sees an increase in velocity. Due to the increase in dynamic pressure at the tail, the forces acting on the tail are larger than without propellers active. This makes the tail more effective. At the same time, the control surfaces also become more effective. This is especially apparent at high AoAs, when the elevator becomes less effective as it is immersed in the wake of the wing. According to Katzoff [15], operation of the propeller largely reduces this loss in elevator effectiveness.

5.6 Accuracy of Stability Calculation Software

In order to say anything about the results from AVL and Tornado, the behaviour of the software should be known. What calculation methods do they use and what is the range of flight conditions in which the results are still accurate. [16, 17, 18, 19, 20, 21, 22]

5.6.1 Accuracy of AVL

"AVL (Athena Vortex Lattice) 1.0 was originally written by Harold Youngren circa 1988 for the MIT Athena TODOR aero software collection. The code was based on classic work by Lamar (NASA codes), E. Lan and L. Miranda (VORLAX) and a host of other investigators. Numerous modifications have since been added by Mark Drela and Harold Youngren, to the point where only stubborn traces of the original Athena code remain." [20]

AVL uses the classical Vortex Lattice Method to model and calculate aerodynamic and stability characteristics. This method is most accurate for thin surfaces and small angles, i.e. small AoAs and small sideslip angles. The software models these surfaces into a single layer vortex sheet, which is split up into horseshoe vortices. The wake created by the surface is assumed to be parallel to the body X-axis.

Because the wake is always assumed to be parallel to the body X-axis, downwash is not taken into account. Also, at higher AoAs or high sideslip angles, the wake is also no longer parallel to the body X-axis in reality. This is one of the reasons why AVL is not as accurate at high angles.

AVL accounts for compressibility by using the Prandtl-Glauert (PG) transformation. This means the PG equation is converted to the Laplace equation. The Laplace equation can then be solved using incompressible flow methods. The forces are calculated by using the Kutta-Joukowsky relation, which is still valid for compressible flow, on each vortex. This method also gives inaccurate results if the change in velocity becomes large or if thick surfaces are used. The PG transformation is expected to be valid up to a Mach number of 0.6.

There have been multiple experiments and projects which used AVL to calculate the stability and control derivatives and also performed wind tunnel tests to verify the results from AVL. The conclusions in the articles are similar and all confirm that AVL is a program that can accurately calculate stability characteristics if the perturbations are small.

5.6.2 Accuracy of Tornado

Tornado is a software developed by Tomas Melin as his master thesis: "A Vortex Lattic MATLAB Implementation for Linear Aerodynamics Wing Applications" [21]. Similar to AVL, it uses the Vortex Lattice Method. However, where AVL uses a horseshoe arrangement, Tornado uses a "vortex-sling" arrangement. The principle is the same as the horseshoe method, except that the wake is assumed to be flexible and consists of seven instead of three vortices of equal strength.

Because Tornado uses a flexible wake, non-linear effects are also taken into account up to a certain degree. This means the control and stability derivatives are more accurate than for AVL, because the influence of the wake is more accurate. This effect is mostly visible in the difference in roll behaviour obtained from AVL and Tornado. Tornado takes the roll-up of the wake into account, while AVL assumes a straight wake. The wake roll-up influences the roll of the aircraft, which explains why the roll response for Tornado is unstable, while AVL gives a stable roll.

Tornado also uses the assumption of thin surfaces and small angles. Therefore, the accuracy of the results decreases as the perturbations become larger.

5.6.3 Conclusions from Software Accuracy

The following ranges of values are assumed to be accurate, for both AVL and Tornado:

- Angle of attack: $0° < AoA < 10°$;
- Sideslip angle: $0° < \beta < 10°$;
- Non-dimensional roll rate: $-0.10 < pb/2V < 0.10$ ($-384 < p < 384$ deg/s);
- Non-dimensional pitch rate: $-0.03 < qc/2V < 0.03$ ($-123 < p < 123$ deg/s);
- Non-dimensional yaw rate: $-0.25 < rb/2V < 0.25$ ($-960 < p < 960$ deg/s).

When using conditions which exceed these limits, the results should be interpreted with caution. The cruise conditions are within the accurate range and cruise is also the flight phase in which the aircraft

spends most time. Therefore, the results obtained from the cruise analyses give a good approximation of the general aircraft stability characteristics.

Since several flight conditions are performed at a high AoA, the results of these analyses are questionable. For the second phase of takeoff, landing and descent, the AoA is 30°, which is well beyond the accurate range. These results are most likely not a good representation of the actual behaviour of the aircraft. To find the stability characteristics at such extreme flight conditions, wind tunnel tests or extensive CFD analyses should be performed.

5.7 Sensitivity Analysis

In order to see how much the results explained in this chapter change if a certain parameter or requirement changes, a sensitivity analysis is performed. Below is a list of parameters that influence the stability characteristics of the aircraft:

- Aircraft geometry:
  - Main wing AR;
  - Tail volumes (both horizontal and vertical);
  - Control surface dimensions;
  - Airfoil (for main wing, horizontal tail and/or vertical tail);
  - Wing planform;
  - Tail incidence angle (both horizontal and vertical);
- C.g. location;
- Mass moment of inertias (e.g. I_{xx}, I_{yz});
- Flight conditions (e.g. airspeed, AoA, sideslip angle);
- Gust magnitude;

There are also some parameters which do change stability, but not directly. For example: changing the type of engine alters the MMOIs, shifts the c.g. location and maybe changes the flight conditions as well. These changes then influence stability, but the change in engine type is not the immediate reason for stability changes. The parameters that have the largest influence on the stability characteristics are: tail volumes, c.g. location:
Tail volumes: the tail volume is defined as $\frac{S_h l_h}{S\bar{c}}$ for the horizontal tail, and similar for the vertical tail. Changes to the surface area or the longitudinal distance greatly affect the stability of the aircraft. For example, increasing the horizontal tail surface area gives the aircraft more longitudinal damping, but it also makes the aircraft more susceptible for gusts. In general, a larger tail volume gives higher stability, but to see the true effect of such a change, a new analysis has to be performed.
C.g. location: if the c.g. changes, there are multiple outcomes. If it shifts forward, stability might increase, since the moment arms of the horizontal tail and vertical tail increase. Vice versa if the c.g. shifts backward. However, if it lies outside of the stability margin, the aircraft becomes unstable. Also for this parameter, a new analysis is required.

5.8 Recommendations

Even though detailed analysis has been done to optimise the design and in the different flight phases, there are still several areas which were not examined in detail due to limitations in software,

time or are out of scope of the group's knowledge. Hence these areas are described in this section such that future work on this design can be carried out with ease.

The first area to look into detail is the stability at high AoAs. Even though Tornado uses the vortex-sling method which makes the analysis more reliable at higher AoAs, the accuracy is still questionable at $AoA > 10°$. Hence a more sophisticated software or advanced CFD should be done on the design to investigate stability especially at high AoAs to have more reliable results.

The second area to consider is the vertical tail incidence influence on stability. A simple analysis is done using both AVL and Tornado to see the effects of adding a toe-in angle on the vertical tail. However, in the analysis model, the connection between the vertical tail and the horizontal tail is not smooth due to limitations of the software used. This would have an effect on the flow near the connection and influence the stability and control derivatives. Hence a proper model with smooth joints should be made and analysed to obtain a more accurate influence of the toe-in angle.

Another important aspect to examine is the flight phases under crosswind situation. The crosswind condition is not considered here due to the limitations of AVL and Tornado in trimming the aircraft in asymmetric flight. For Tornado, only one of the control surfaces could be chosen to analyse trim which is not possible for asymmetric flight as both ailerons and rudders have to be used. For AVL, it is possible to trim with the control surfaces but it is unable to simulate trim with aircraft body rotations. As a result, large deflection angles are given for the maximum crosswind condition of $6m/s$. Since the analysis for AVL and Tornado are unable to simulate real flight conditions, the analysis with crosswind is not done. For the final design, crosswind analysis should be done with a more sophisticated tool as it is likely that the UAV will be flying under crosswind at some point in the demonstration flight.

Besides the above points, the most important area to consider is the effect of the propeller on the tail. As it is impossible to implement propellers into AVL and Tornado, the stability analysis is done with propellers and the effect of the propeller slipstream on the tail is investigated separately based on literature. This effect is elaborated on in the section 5.5. As C-wings used as tails in combination with tip-mounted propellers is a new concept, there is few literature examining the effect of propeller-tail interaction. Hence the literature used to investigate such an effect is mainly for propeller interation with a conventional T-tail. Therefore, in order to obtain the most accurate results for the stability of the design, CFD as well as wind tunnel tests should be done. Another condition to consider with the engine is the effect on stability with one engine inoperative (OEI). When such a situation occur, the control surfaces should be capable of trimming the aircraft. Due to the inability of implementing propellers in the software. This situation could not be investigated. Thought is given to assign a certain moment in the Z-axis in the flight condition to simulate the OEI condition but due to the inability to trim the model in asymmetric flight, such an analysis could not be carried out either. Hence, for more detailed design, care should be taken to analyse this condition in great detail. Since the vertical tail design is partly based on OEI condition during takeoff, special attention should be given to the analysis during this condition.

The analysis for the above considerations is not possible without more sophisticated software or advanced CFD analysis. Besides such numerical analysis, it is also recommended for the design to be put through the wind tunnel for tests in order to validate the numerical models. More details of the propeller-tail interaction can also be achieved through such wind tunnel tests. This is essential as such a configuration is new, so conventional numerical analysis has to be backed with actual test results to make sure that the numerical results are reliable. After wind tunnel tests are done, it is also recommended to hold a test flight before the actual competition.

6 Controllability

In this chapter the control surfaces sizing and exact location is determined. With a preliminary size a first design optimisation is done. During this first optimisation there is checked with AVL or Tornado if the model is trimable in different flight phases. If not, the control surface size is adjusted to lower the trim angles. After the trim condition is known, there is looked if there is enough deflection left to control the aircraft. There is also looked if it can reach the desired pitch, roll and yaw rate. After this the controllability is checked at high AoA and high deflection angles. Finally, a preliminary sizing is done for the belly flap.

6.1 Sign Convention

Before the trim condition and control derivatives can be found, first the sign should be determined. For the sign convention the same method is used as taught in the Flight Dynamics course [23]. A positive aileron/elevator deflection is when it is deflected downwards. For the rudder the deflection is positive when it is deflected to the larboard wing.

6.2 Control Surfaces Sizing

Longitudinal control or pitch control is achieved by deflecting both elevators in the same direction. For the sizing of the ailerons, elevator and rudders, as a first approximation the method of Sadraey [24] is used. In this method, the control surfaces are sized according to percentages. For the elevator, and also the other control surfaces, the used range is shown in 6.1. The determined size is for two elevators and is divided by two, since there are two elevators (one on each horizontal stabiliser).

Table 6.1: Control surfaces size and location limits mentioned in [24].

	from	to		from	to		from	to
S_e/S_h	15%	40%	S_a/S	5%	10%	S_r/S_v	20%	40%
b_e/b_h	80%	100%	b_a/b	20%	30%	b_r/b_v	60%	100%
C_e/C_h	20%	40%	C_a/C	15%	25%	C_r/C_v	30%	50%
$\delta_{e_{max_{up}}}$	25 °	-	$\delta_{a_{max}}$	±20 °		$\delta_{r_{max}}$	±25 °	
$\delta_{e_{max_{down}}}$	20 °	-						

All preliminary control surface dimensions defined for Tip-C are summarised in table 6.2. For the elevator this results in a surface area of 0.02 m^2.

Lateral control, or roll control, is achieved by deflecting the ailerons in opposite direction. Deflecting the right aileron upwards and the left aileron downwards, results in a roll to the left.

Since the moment arm of the ailerons is very small, the size and deflection angle of the ailerons should be large to create enough roll. How much is needed, is determined via an iterative process as explained earlier. As a first estimate the location is chosen as far as possible from the symmetry (x) axis to have the largest arm. The area is chosen exactly between the calculated values and equals 0.04 m^2.

Directional control or yaw control is achieved by deflecting the rudder. Because Tip-C has two rudders, both should be deflected in the same direction. Deflecting the rudders to the starboard wing, will result in a yaw to the starboard direction. Vice versa for deflecting the rudder the other way around.

The determined size for the rudder is also divided by two, since Tip-C has two rudders. The location of the inboard edge of the rudder (b_{R_i}) is chosen arbitrarily.

Table 6.2: Preliminary control surface sizes for *one* of two control surfaces.

Parameter	Elevator	Aileron	Rudder
c_{tip} [m]	0.054	0.04	0.09
c_{root} [m]	0.054	0.04	0.09
b [m]	0.37	0.1657	0.14

6.3 First Design

To determine the trim conditions calculated by the stability department with AVL and Tornado are used. The geometry of Tip-C is used as an input together with the flight phase conditions. There are six critical phases defined at which trim and controllability is checked. These phases are takeoff, climb, cruise, descent and landing (see table 6.3). For climb there is sized for climb rate and climb gradient. During these stages the trim condition is determined in AVL and Tornado by the stability group. At high AoA, Tornado is more reliable. The reason for this is explained in section 5.6.

Table 6.3: Flight phases with their flight angles.

	Takeoff	Climb rate	Climb gradient	Cruise	Descent	Landing
V [m/s]	14 and 20	max 22	max 20	37	20	20
AoA [deg]	15 and 30	11	15	2	30	30
Required Manoeuvrability						
q [deg/s]	30	0	0	30	0	15
p [deg/s]	0	0	0	10	0	5
r [deg/s]	0	0	0	15	0	5

With the given trim angles for elevator, aileron and rudder it is determined whether there is enough deflection left to manoeuvre and to achieve the desired pitch, roll and yaw rate. For takeoff and landing crosswind is taken into account, since the location of the runway is fixed. The aircraft should be able to takeoff and land under this conditions. The requirement for the competition state a maximum crosswind of 6 m/s.

In section 6.5, the accuracy and reliability of the results are discussed.

6.3.1 Takeoff

For takeoff the AoA changes from 15° to around 30°, the pitch rate needed equals 30°/s and is determined by the performance group. In table 6.4 the trim deflections are shown for both takeoff stages and with and without crosswind. AVL and Tornado are not capable of calculating all conditions, so only the ones that are available are stated.

In MATLAB two stability models are made, one for AVL and one for Tornado. This stability model calculates the eigenmodes of Tip-C for stability. In this model it is possible to give a step input on the elevator, aileron or rudder and see how Tip-C responses. In AVL the trim elevator deflection is -11.890°. The maximum deflection is -25°, this means that there is -25+11.890 = -13.110° left to pitch Tip-C. For Tornado there is -25+14.027 = -10.973° left to pitch. For pitch down the possible deflections are larger, so this case is not taken into account. If in both models a step input is given on the elevator, the responses can be seen in figure 6.1. For AVL the maximum pitch rate equals

Table 6.4: Takeoff trim angles (N.A. = Not Available).

	α=15°, V=14m/s		α=30°, V=20m/s	
	without crosswind	with crosswind	without crosswind	with crosswind
		AVL		
δ_e [deg]	-11.890	-2.815	N.A.	N.A.
δ_a [deg]	0	-100.064	N.A.	N.A.
δ_r [deg]	0	205.830	N.A.	N.A.
		Tornado		
δ_e [deg]	-14.027	N.A.	-53.462	N.A.
δ_a [deg]	0	N.A.	0	N.A.
δ_r [deg]	0	N.A.	0	N.A.

20.86°/s. For Tornado the maximum pitch rate equals 12.03°/s. This is *not* large enough to give the aircraft the desired pitch rate of 30°/s. For the aileron and rudder the trim deflections are zero, this means that for both the aileron and rudder there is ± 25° left. These deflections are also well large enough.

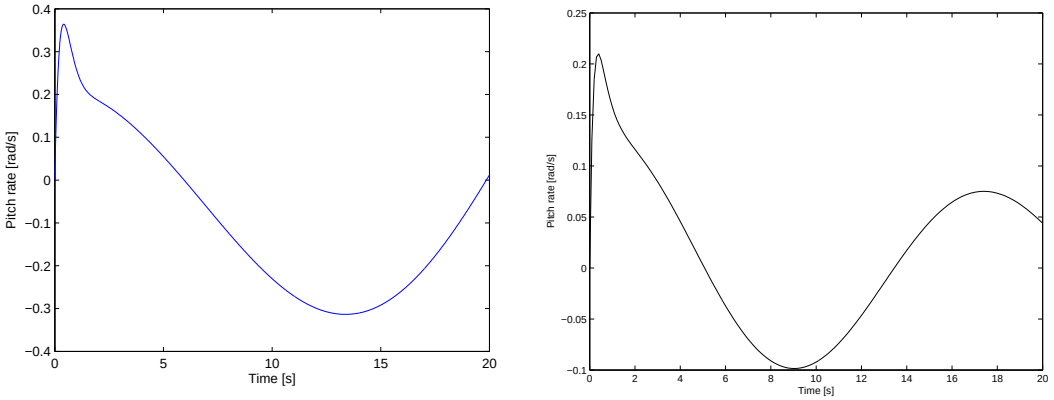

(a) AVL δ_e = -13.110° (b) Tornado δ_e = -10.973°

Figure 6.1: Takeoff: response of Tip-C on an elevator step input.

6.3.2 Climb Rate

According to the performance sizing for climb rate, the velocity should be 22 m/s with an AoA of 11°. During climb it is not necessary to have a specified pitch, roll and yaw rate, since no specific change is needed. The required control surface deflections are shown in table 6.5.

Table 6.5: Climb rate trim angles.

α=11°, V=22m/s		
	AVL	Tornado
δ_e [deg]	-9.851	-10.370
δ_a [deg]	0	0
δ_r [deg]	0	0

For AVL there is -15.149° left to pitch-up and for Tornado -14.630°. This results in a pitch rate of 29.828°/s for AVL and 28.447°/s for Tornado (see figure 6.2).

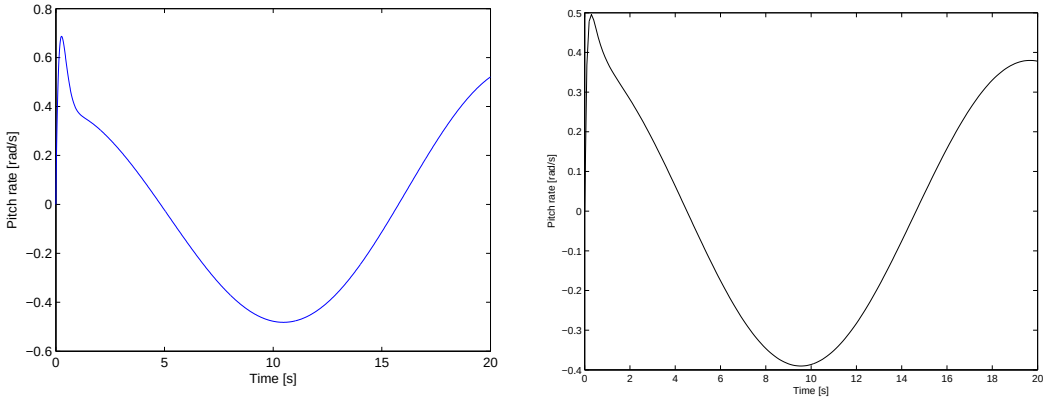

(a) AVL δ_e = -15.149° (b) Tornado δ_e = -14.630°

Figure 6.2: Climb rate: response of Tip-C on a elevator step input.

6.3.3 Climb Gradient

Again, according to performance sizing, the AoA for climb gradient should be 15° with a speed of 20 m/s. There is no desired pitch, roll and yaw rate. The required trim deflections are shown in table 6.6. For AVL there is -13.1104° left for pitch-up and for Tornado there is -10.973° left.

Table 6.6: Climb gradient trim angles.

α=15°, V=20m/s		
	AVL	Tornado
δ_e [deg]	-11.890	-14.027
δ_a [deg]	0	0
δ_r [deg]	0	0

Looking at figure 6.3, the pitch rate for AVL equals 0.520rad/s which is 29.828°/s. For Tornado it equals 0.314rad/s, 18°/s.

6.3.4 Cruise

For cruise the speed is defined to be 37 m/s and the AoA is specified to be 2°. Since the UAV is small, it should be able to manoeuvre very fast. The pitch, roll and yaw rate are set at 30, 10 and 15 °/s. The values are based on what experts advised and what current UAVs are capable of doing. Because Tip-C is almost a square, the expected roll damping is very high, therefore the roll rate is specified to be low. The trim deflection angles as determined by the stability group can be seen in table 6.7.

For AVL, the elevator deflection leaves -16.377° for moving the elevator upwards and 28.62° to move downwards. For Tornado the elevator deflection to pitch is -16.959° and the downward deflection is 28.041°. Giving a step input on the elevator for both AVL and Tornado (see figure 6.4), results in a pitch rate of 1.332 rad/s for AVL, which equals 76.318°/s. For Tornado this is 79.412°/s. According to these results, the desired pitch rate of 30°/s can be achieved.

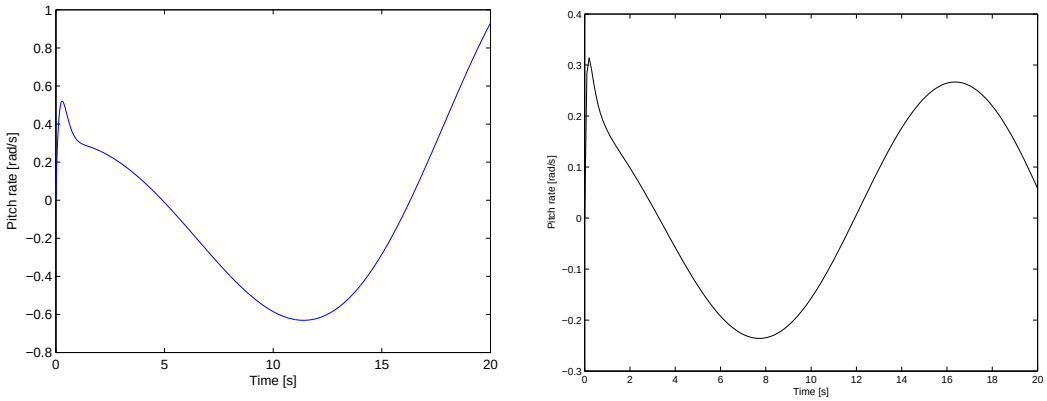

(a) AVL δ_e = -13.110° (b) Tornado δ_e = -10.973°

Figure 6.3: Climb gradient: response of Tip-C on a elevator step input.

Table 6.7: Cruise trim angles.

α=2°, V=37m/s		
	AVL	Tornado
δ_e [deg]	-8.623	-8.041
δ_a [deg]	0	0
δ_r [deg]	0	0

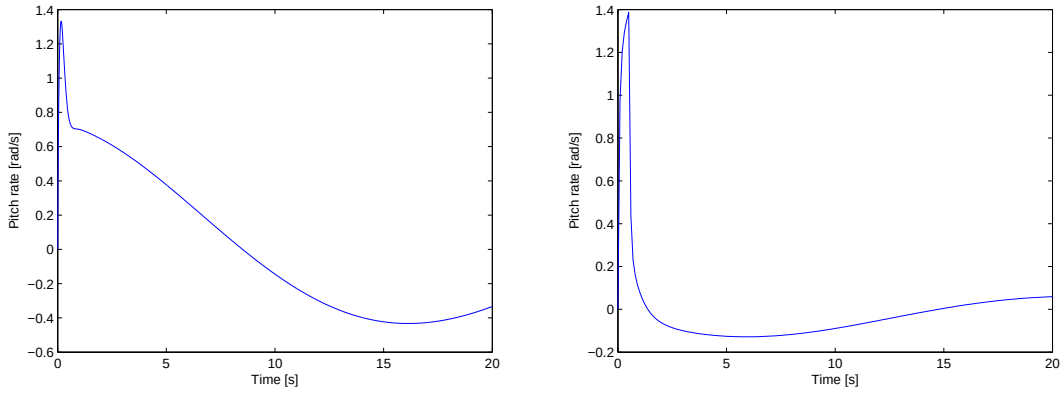

(a) δ_e = -16.377° (b) δ_e = -16.959°

Figure 6.4: Cruise: response of Tip-C on an elevator step input.

For both the aileron and rudder, the trim deflection is zero. This means that for both ±25° deflection can be used for manoeuvring. For AVL, an aileron step input of ±25° results in a maximum roll rate of ±286°/s after which slowly damps out. A ±25° input on the rudder results in maximum yaw rate of ±355°/s after 140 seconds, the motion is not damped.

6.3.5 Descent and Landing

For descent and landing, the AoA and velocity are equal to the takeoff phase 2 without crosswind (table 6.4 column 4+5), so they are discussed together. For landing a crosswind of 6 m/s should be taken into account. Only Tornado was able to trim Tip-C in descent/landing conditions. The elevator deflection that is required for trim is -53.462°.

6.3.6 Controllability at High Angles of Attack

Neither AVL or Tornado takes viscous flow into account. For this reason, the accuracy of the stability and control derivatives should be questioned. At high AoA the effectiveness of the control surfaces can go down due to flow separation over the control surface. Combining this with high deflection angles of the control surfaces, the possibility arises that the UAV becomes uncontrollable.

6.3.7 Differential Thrust

Instead of a rudder for yaw, differential thrust can be used as well. For example during cruise, per engine a maximum thrust of 47N is available. Setting one engine at zero and the other at maximum, the torque created is 26Nm. The maximum moment created by the rudder is about 14Nm. As can be seen, differential thrust can be used for yaw as well since the torque created by the engine is larger than 14Nm.

6.3.8 Maximum Hinge Moments

The maximum hinge moments are obtained via AVL by the stability department. AVL can calculate the hinge moment for a given flight speed, deflection and AoA. For the same reason as for the controllability at high angles, these hinge moments are without viscous flow. Therefore, their actual value can deviate from what AVL gives. During the actuator design in the Aircraft Systems Chapter a safety factor of 2.5 is used. The hinge moments are determined for cruise, since this is the most accurate flight phase. The determined hinge moments are given in table 6.8.

Table 6.8: Hinge moments during cruise, determined by AVL at maximum control surface deflections.

Elevator	Aileron	Rudder
0.978 Nm	1.748 Nm	0.0752 Nm

6.3.9 New Control Surfaces Geometry

After a few optimisations, the final control surfaces size is known. There is made sure that Tip-C is trimable at low angles of attack (α<10°). After 10°, the results become more inaccurate, see section 5.6. This is also the case for landing and descent, where the elevator deflection for trim is over -50°. When crosswind comes in, Tornado is not able to trim. The trim angles of AVL are too large and very inaccurate.

6.4 Belly Flap

As explained during the mid-term phase, there was a possibility to implement a belly flap on Tip-C. A belly flap is mainly used for blended wing bodies (BWB) where the pitch controls have a shorter arm compared to a conventional tailed aircraft. Due to this shorter arm a larger down force is needed by deflecting the elevator. "This introduces a larger lift-loss, causing the BWB first to plunge downward before achieving the desired AoA" [25]. Since Tip-C has a very short body compared to the span, a belly flap can also be suitable. When the belly flap is deployed, it creates a positive pressure in front of the flap and a negative pressure behind, which results in a (positive) nose-up pitching moment

Table 6.9: Old versus new control surface geometry determined .

	New	**Old**	**% Change**
$S_e[m^2]$	0.0250	0.0200	+25
$b_e[m]$	0.2500	0.3700	+48
$c_e[m]$	0.1000	0.0540	+85
$S_a[m^2]$	0.0375	0.0279	+74.4
$b_a[m]$	0.2500	0.1383	+80.77
$c_a[m]$	0.1500	0.2020	-74.26
$b_{a_i}[m]$	0.3314	0.3140	+5.54
$S_r[m^2]$	0.0126	0.0126	0
$b_r[m]$	0.1400	0.1400	0
$c_r[m]$	0.0900	0.0900	0

(see figure 6.5).

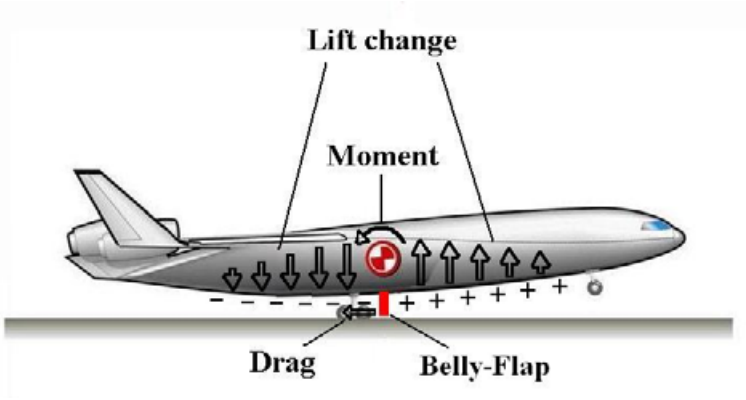

Figure 6.5: Principle of a belly flap [25].

A belly flap is very suitable for takeoff and landing. During takeoff it can be deployed to give extra pitch-up moment. This is beneficial since it helps to rotate the aircraft during takeoff but also during landing. It shortens the takeoff distance and thereby shorter runways can be used. A belly flap does not only increase the pitching moment, but it also increases drag. This increase in drag is beneficial during landing, because it can be used to slow the aircraft down. The sizing of the belly flap is done according to the study of reference [25]. In this study a model of the Boeing BWB is tested in a wind tunnel with different belly flaps. The Reynolds number equals $1.37{\cdot}10^6$ with Mach number of 0.09, which is quite similair to the condition Tip-C is flying in. The result of the wind tunnel test is summarised in table 6.10. It shows the optimum span, chord and location of the belly flap.

Table 6.10: Result of wind tunnel test on 7 belly flaps.

	Percentage	Result
Span	14.1%b	0.1557m
Chord	24.4%M.A.C	0.2506m
Longitudinal location	60-65%C_{root}	0.6000m
Lateral location		On centre line

Different types of belly flaps were tested, with and without porosity and with two different chord lengths. There is looked at the pitching moment, lift and drag change of seven different types. The recommended and selected belly flap is a 23% porosity flap, which increases the lift by 27% at 0° AoA and 13% at 8° AoA, the relation is almost linear. Due to the high porosity, the drag increase is low, around 5% for all AoA. The pitching moment coefficient increase is 5% at 0° AoA and 7% at 8° AoA, again this relation is linear.

Remark The expected increase in lift, drag and pitching moment are optimum for the tested BWB with similar characteristics. The half span equals 0.54m which is comparable to Tip-C. The Reynolds number ($1.17 \cdot 10^6$) and Mach number (0.1) of Tip-C are about equal to the BWB model. Although this does not mean that this belly flap size and location is the best option for Tip-C. A wind tunnel test should be performed to determine the optimum location. The preliminary estimate, based on reference [25] can be used as a first estimate to start with.

6.5 Validation and Discussion of Results

In this section the discussion of the results is done. The difference between the results of AVL and Tornado are very small. The largest difference is found to be 8% for the elevator deflections at high AoA (>15°). As might be noticed, the trim conditions for crosswind can not be calculated by Tornado. This is due to the fact that Tornado can only trim with one control surface at a time. For crosswind, the trim condition should be achieved by deflecting more than one control surface, which is simply a restriction of Tornado.

The results AVL give for crosswind are questionable. The competition requires to handle a crosswind of 6 m/s. During climb, cruise and descent, the UAV can adjust its flight to the crosswind condition, but for takeoff and landing, it should align with the runway. This means that there is a possibility that the crosswind acts perpendicular on the UAV. AVL was able to trim the UAV with impossible large deflection angles.

A reason for this could be the large contribution of C_{l_β} to the aerodynamic roll moment, due to the high sideslip angle. To counteract this roll moment, the aileron and rudder can be used. The contribution of the aileron, $C_{l_{\delta_a}}$ is much larger than the rudder, but not large enough to counteract the aerodynamic roll. For the large rudder deflection, the reason lies in the relatively low value of $C_{n_{\delta_r}}$, which requires a large deflection to counteract the aerodynamic yaw moment.

For takeoff phase 2 and descent and landing without crosswind, the department of stability was only able to calculate a trim value with Tornado. However, this trim value equals -53°. A cause for this large deflection can be due to the high aerodynamic pitch moment that is created by the high AoA. A solution can be to use elevons instead of ailerons. The elevons can "help" with creating that extra pitch down moment. However, the effectiveness of this solution should be investigated in the next phases of the design.

As specified by the performance group, for takeoff a pitch-up moment of 30°/s is needed. This pitch-up moment is *not* met by around 7°/s for AVL and 18°/s for Tornado. Because the elevator deflection of Tornado is larger, there is less deflection left to pitch. This results in a smaller pitching moment for Tornado compared to AVL. A solution for this problem can be an increase of the control derivative $C_{m_{\delta_e}}$. This increase can be achieved by making the elevators larger, or increase their moment arm.

The latter one is rather difficult, since the tail should than be moved backwards. Moving the tail backwards influences stability, since it changes the c.g. and the n.p. location. Increasing the elevator size is difficult as well, because the elevators are almost as large as the horizontal stabiliser. A solution can be to join the two horizontal stabilisers, but this will influence the c.g. and n.p. as well. If this

solution is chosen, the whole design should be redone. A more feasible solution is to make the ailerons elevons, so that they can "help" with pitching.

6.6 Sensitivity Analysis

The controllability is affected by a few parameters, e.g. control surface size, c.g. and n.p. location, tail size and location and MMOI. In the design of Tip-C the most critical parameters are number 2 and 3, because they are the most likely to change. In fact, 3 is related to 2. Changing the tail size and/or location will change the c.g. and n.p. location, which changes the S.M. An increased S.M. is beneficial for stability but for controllability a decreased S.M. is preferable.

Besides this, a more aft c.g. location requires less lift of the tail to trim [26]. Moving the tail more backwards increases the tail arm, which makes the tail and thus the control surfaces on the tail more effective. Shifting the internal systems inside can change the c.g., a more aft c.g. results in higher controllability. If the airfoil of the tail is changed, the lift generated by the tail changes, a smaller tail lift coefficient lowers the trimmability. Which means that it requires more work to trim.

6.7 Recommendations

- Due to the inaccuracy of AVL and Tornado at high AoA and the inaccuracy with crosswind, a wind tunnel test would be advised to check the reliability of the results. If it turns out that the effectiveness of the elevator is too low, there can be looked at the possibility of using elevons. If elevons seem to be insufficient as well, the possiblity to join the C-wing exists. However, this shifts the c.g. and n.p. to the back. The possibility exist that the S.M. changes. A decrease is beneficial for controllability, an increase for stability. The consequence of this should be investigated.

- As explained before, the controllability at high angles should be investigated as well. Predicting this with AVL and Tornado is not possible, because these programs do not make use of viscous flows. Another advanced CFD program can be used, but the inaccuracy of this program should be investigated as well. Besides this, a whole new model should be created. A wind tunnel test in this case might be a faster solution.

- For the placement of the belly flap a preliminary location is determined, this location should be tested in order to see if it is the optimum location for Tip-C.

- Due to the tip-mounted propellers, there is a possibility that the propeller slipstream affects the control surfaces. Neither in AVL or in Tornado it is possible to include propellers. According to reference [27], the slipstream increases dynamic pressure values which leads to an increase in the lift and drag coefficient. Besides this, the propeller slipstream alters the pressure distribution of the horizontal and vertical stabiliser which results in a change in the local AoA. Of course, this affects the control surfaces. But to what extend should be investigated via CFD or wind tunnel testing.

7 Propulsion Design

In this chapter, the detailed design and performance modelling of the engine is elaborated. Firstly, the initial design point of the propulsion is specified. Thereafter, specific details such as propeller airfoil and engine selection are elaborated. The design of the propulsion system concerns mainly the selection of the propeller blade and engine system.

In the beginning, various type of propeller airfoils are selected and compared. The propeller airfoil that gives the best aerodynamic properties is selected. This results in the highest thrust produced for a given blade diameter, power supplied and number of blades. Once an optimal propeller blade is chosen, the next key consideration is to match the propeller to the engine such that a good impedance matching can be achieved. The purpose of such a matching is to ensure a high peak efficiency for both the engine and the propeller at its design operating point.

7.1 Propeller Design Point

In the initial design phase, the operating design point is specified. The following parameters are needed to run both Qprop and Javaprop: the propeller hub radius, free stream flight speed, rotation velocity and the required power. The chosen free stream flight speed was determined based on the AoA for maximum lift to drag ratio. The optimal AoA was found to be 2° and the value of lift coefficient was approximately 0.22. The flight speed is calculated to be 37m/s, using equation 7.1:

$$V_{cruise} = \sqrt{\frac{2W}{S\rho C_{L_{cruise}}}} \tag{7.1}$$

An initial estimate of the propeller diameter is then calculated from equation 7.2.

$$D_p = K_{np}\sqrt{\frac{2P\eta_p AR_p}{\rho {V_{av}}^2 C_{L_p} V_{cruise}}} \tag{7.2}$$

The initial total engine power is determined from the required power loading, which is limited by the climb gradient requirement. Given a power loading of 0.047 N/W and an initial MTOW estimation of 21.36 kg, the required power per engine is calculated to be approximately 2200 W. A range of propeller AR from 7 to 15 was used. The propeller efficiency is estimated to be 75%. The average velocity is estimated to be 70% of the propeller tip speed at cruise of approximately 180m/s.

A range of propeller rotational speeds (n in revolutions per minute) is then calculated from equation 7.3. This is used as input into Javaprop together with the selected propeller geometry to calculate the propeller thrust and torque.

$$n = \frac{120\sqrt{V_{tip_{cruise}}^2 - V_c^2}}{D_p 2\pi} \tag{7.3}$$

Once all these parameters are known, they are then used as inputs into Javaprop to obtain an initial estimate of the propeller thrust and torque. These initial values are subsequently adjusted during the design process to ensure that the thrust produced by the propeller meets the takeoff and climb gradient requirements.

7.2 Propeller Airfoil Selection

In the selection of a propeller airfoil blade, the relative velocity acting on the airfoil blade varies from root to tip, due to the changing angular velocity. In the design of the airfoil blade in Javaprop,

it is desired to have a high L/D at a specified AoA for each element along the radius. As such, the optimal AoA at each element has to be specified accordingly. This AoA varies with selected airfoil type, since the AoA for maximum L/D differs for each airfoil.

Due to the increasing angular velocity from root to tip, the angle φ reduces progressively from hub to tip. In order for the airflow to act on each blade element at its optimal angle of attack from hub to tip, the pitch angle, β has to be progressively reduced in order to keep the angle of attack between the relative velocity vector and the blade element at its optimal angle of attack. As such, the pitch of the blade varies from hub to tip. It is noted that the pitch angle β will be larger nearing to the hub due to the larger relative velocity angle at the hub. This is illustrated in figure 7.1.

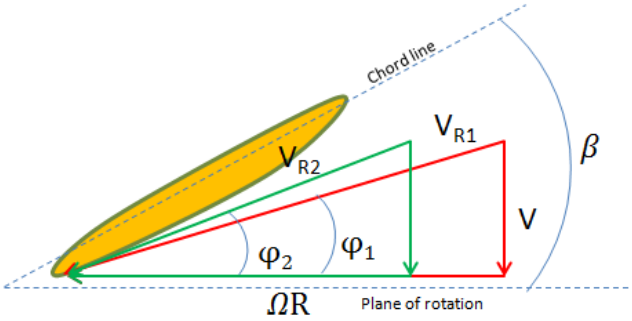

Figure 7.1: Free body diagram of velocity vectors acting on a propeller blade element.

The following airfoils are considered; Clark Y, MH 126, MH 112, MH 114, ARA D6 and E193 airfoil. Their L/D are presented in table 7.1. The selection of the propeller airfoil is based on the value of L/D, since a higher L/D value implies a lower drag force, a smaller engine torque and a higher net thrust. This is illustrated in figure 7.2. The L/D values are obtained at an estimated reynolds number of 500000. In both figure 7.1 and 7.2, it should be noted that the induced velocity component is not considered for the sake of clarity.

Table 7.1: Maximum lift to drag ratio of various airfoil types.

Propeller Airfoil	Maximum Lift to Drag Ratio at specified AoA
Clark Y	29.2
MH 126	12.6
MH 112	22.7
MH 114	27.9
ARA D6	17.2
E 193	29.1

From table 7.1, it can be seen that the Clark Y airfoil has the highest L/D among the various airfoils considered and thus it is selected for the engine and performance modelling. The propeller airfoil selected for performance modelling might differ from the actual propeller blade used for the competition, since the final propeller has to be purchased off-the-shelf.

The selected blade geometry is extracted from Javaprop and defined in Qprop to compute the thrust and torque of the propeller. As part of verification, the thrust and torque values obtained from Javaprop and Qprop are compared at a later stage. These thrust and torque values are computed based on blade element theory. An illustration of the forces acting on the propeller blade with induced

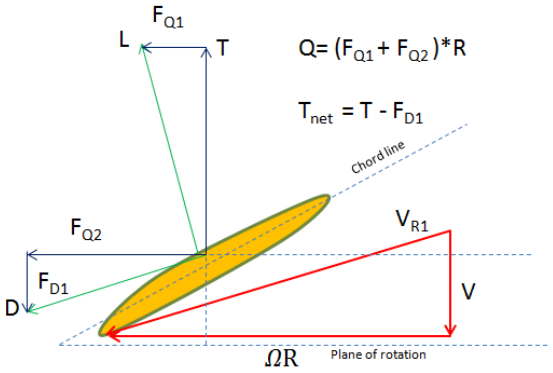

Figure 7.2: Free body diagram of forces acting on a propeller blade element.

velocity taken into account is presented in figure 7.3. The governing equations for computing thrust and torque are given in equation 7.4 [28] and 7.5 [28].

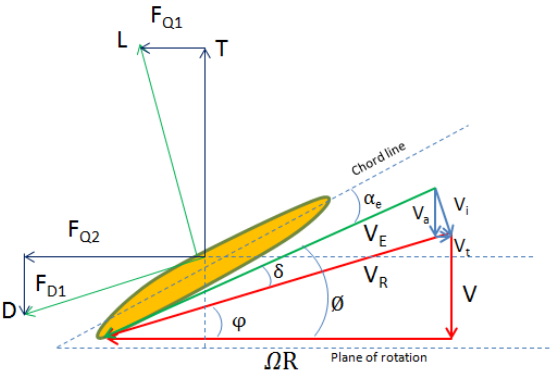

Figure 7.3: Free body diagram of forces and velocity vectors acting on a propeller blade element.

$$T = B \int_H^R \frac{1}{2} \rho {V_E}^2 c \left(c_l cos(\phi) - c_d sin(\phi) \right) dr \tag{7.4}$$

$$Q = B \int_H^R \frac{1}{2} \rho {V_E}^2 c \left(c_l sin(\phi) + c_d cos(\phi) \right) r dr \tag{7.5}$$

In equation 7.4 and 7.5, V_E is the effective velocity, ϕ is the angle between the plane of rotation and the effective velocity and B is the number of propeller blades. R and H represents the tip and hub radius respectively. It can be seen from equation 7.4 and 7.5 that the higher the drag coefficient, the lower the net thrust produced and the higher the engine torque required. Hence, the propeller airfoil that generates the least drag is highly desired.

7.3 DC Motor Propeller Matching

Once the propeller is sized with the required engine power and rotation speed, the next step is to find an engine that matches the propeller torque to the engine torque. In order to do so, a method based on the lecture notes of Massachusetts Institute of Technology (MIT), "DC Motor/ Propeller Matching" is used. The governing equations for making this model in MATLAB are presented below. The following motor parameters, motor torque, motor efficiency and shaft power, can be calculated

from equation 7.6, 7.7 and 7.8 respectively. A representative illustration of the circuit diagram is shown in figure 7.4.

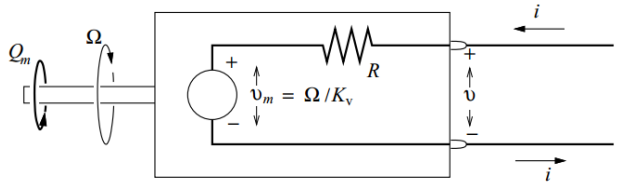

Figure 7.4: Representative circuit diagram of engine with power source.

$$Q_m(\Omega, \upsilon) = \left[(\upsilon - \frac{\Omega}{K_\upsilon})\frac{1}{R_m} - i_o\right]\frac{1}{K_\upsilon} \tag{7.6}$$

$$\eta_m(\Omega, \upsilon) = \left[(1 - \frac{i_o R_m}{\upsilon - \Omega/K_\upsilon})\frac{1}{R_m} - i_o\right]\frac{\Omega}{\upsilon K_\upsilon} \tag{7.7}$$

$$P_{shaft}(\Omega, \upsilon) = \left[(\upsilon - \frac{\Omega}{K_\upsilon})\frac{1}{R_m} - i_o\right]\frac{\Omega}{K_\upsilon} \tag{7.8}$$

In the above equations, $K_\upsilon = 192$rpm/V, internal motor resistance $R_m = 0.16\Omega$, and idle current $i_0 = 2.1$A. The following governing equations for calculating the propeller parameters, advance ratio, propeller thrust and propeller torque, are given in equation 7.9, 7.10 and 7.11. The thrust and power coefficients are obtained directly from Qprop.

$$\lambda = \frac{V}{\Omega R} \tag{7.9}$$

$$T_{prop} = \frac{1}{2}\rho V^2 \pi R^2 \frac{C_T}{\lambda^2} \tag{7.10}$$

$$Q_{prop} = \frac{1}{2}\rho V^2 \pi R^3 \frac{C_P}{\lambda^2} \tag{7.11}$$

The torque matching condition $Q_m = Q_{prop}$ is then applied to determine the required motor rotation speed. This rotation speed has to be close or exactly the same as the rotation speed used as input for Qprop and Javaprop earlier, since there is a thrust requirement for each engine. Using the required motor rotation speed, the other motor parameters are determined from the motor and propeller characteristic curve. In the process of matching the torques, the flight velocity and the motor voltage have to be specified. The flight velocity is specified to be the cruise speed (37m/s) since it is desired to have high efficiency during the cruise phase. The supplied voltage to the engine is 36 volts as specified in the motor catalogue. The results of the final iteration are presented below.
From figure 7.5, the required rotation speed is about 6800rpm. This is then verified with the engine manufacturer data to see if the selected engine is able to spin at this rotation speed. The final engine selected is the Hacker A60-14L. From the required rotation speed, the motor and propeller efficiencies can be determined. Their results are presented in figure 7.6 and 7.7.
As seen in figure 7.6 and 7.7, the current configuration is able to achieve a motor and propeller efficiency of approximately 0.93 and 0.85 respectively. This gives a total efficiency of 0.79 during cruise. It should be noted that the motor is initially selected based on power requirements for climb gradient. This motor parameter is then inputted into the program to check for torque matching. The resulting motor rotation speed is verified with the engine catalogue to see if such a rotation speed is feasible.

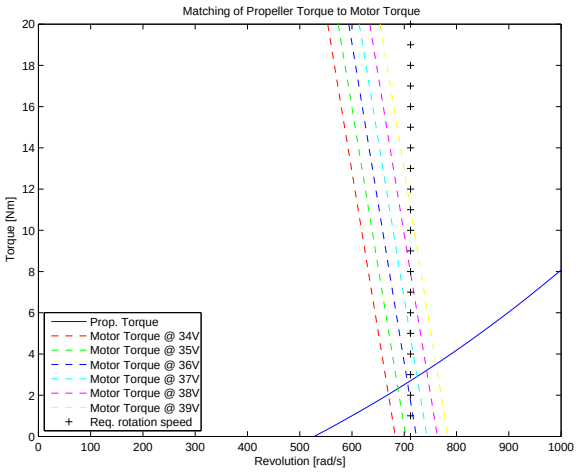

Figure 7.5: Matching the propeller torque to the motor torque.

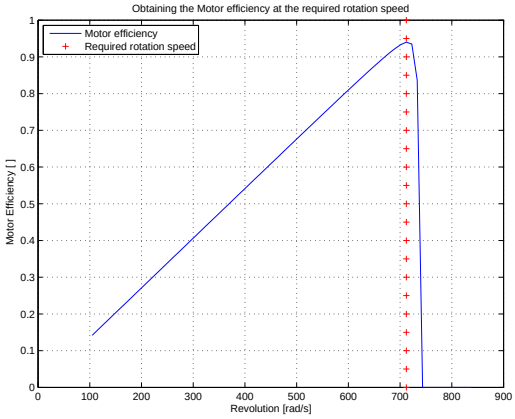

Figure 7.6: Motor efficiency vs. rotation speed.

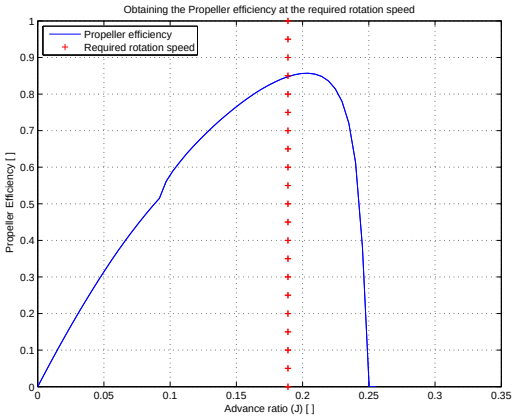

Figure 7.7: Propeller efficiency vs. advance ratio.

7.4 Effect of Variable Pitch on Propeller Performances

During the Mid-Term phase, it was initially decided that a variable pitch mechanism would be used since such a system would provide an improvement to the overall efficiency of the system. It was later discarded since there was insufficient time to realise it. However, the effect of variable pitch was already investigated in Qprop to analyse its overall effect on the propeller performance. It should be pointed out that these graphs are produced assuming a constant rotation speed of 5900rpm based on the initial design operating point.

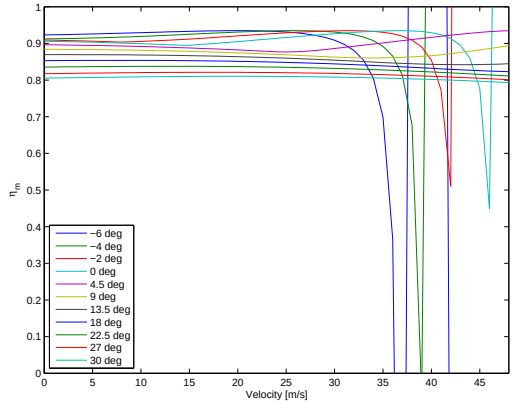

Figure 7.8: Motor efficiency vs. velocity.

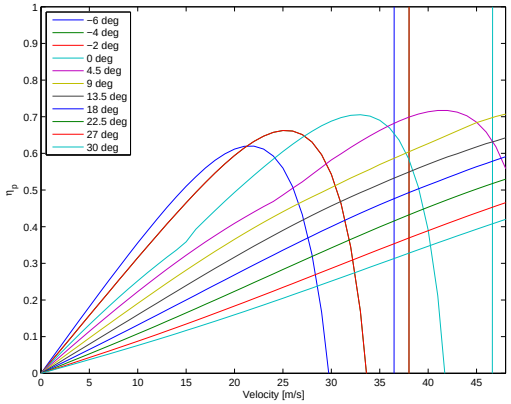

Figure 7.9: Propeller efficiency vs. velocity.

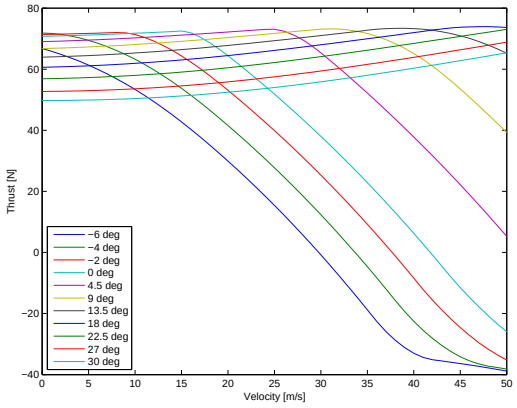

Figure 7.10: Thrust vs. velocity.

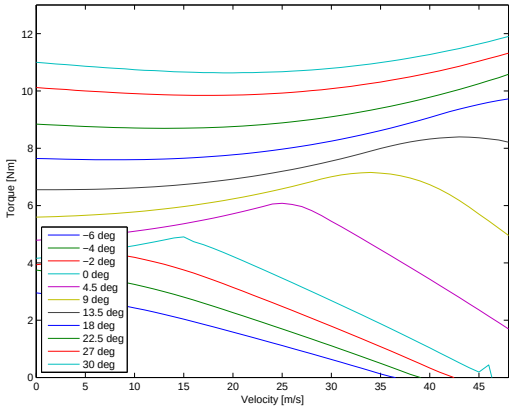

Figure 7.11: Torque vs. velocity.

In figure 7.8, it can be seen that the motor efficiency stays almost constant. This is only true in the case that the engine rotation speed stays constant as the velocity changes. From figure 7.6, it is clear that the engine efficiency is a function of the rotation speed. Hence it is desired to keep the engine rotation speed close to its maximum efficiency point during the various flight phase. This can be achieved with the use of a constant speed governor.

In figure 7.9, it can be seen that the propeller efficiency varies as the velocity changes. This is valid since the effective AoA varies according to the free stream flight velocity (see figure 7.3). As such, the amount of thrust produced at each velocity point varies too. There exists an optimal velocity at a given blade pitch angle setting for maximum propeller efficiency. The implementation of a variable pitch mechanism ensures a high propeller efficiency throughout its operating velocity range.

In figure 7.10, the effect of the change in thrust due to changing pitch blade angle is investigated. It is interesting to note that the thrust curve shifts up as the blade pitch angle reduces. This means that it is beneficial to lower the blade pitch angle during takeoff, to achieve higher thrust and efficiency during low speed.

Another point to note is that all the thrust curves start declining once they reach a certain velocity (depending on the blade pitch angle setting). This point of decline shifts towards higher velocities as the blade pitch angle increases. Therefore, it is beneficial to increase blade pitch angle at higher speed to achieve higher thrust and efficiency. As the free stream velocity increases, the thrust curve

declines. This decline in thrust is mainly due to the increase in relative angle ϕ, which leads to a lower effective AoA.

Finally, it can be seen in figure 7.11 that the effect of increasing the blade pitch angle results in a higher propeller torque. This is valid since a higher blade pitch angle results in a higher effective AoA, given the same rotation and flight speed. The increase in AoA leads to a higher drag for each blade element and thus leads to higher torque. Hence, the actual engine power requirement will increase depending on the maximum adjustable blade pitch angle during flight. The decrease in torque after a certain flight speed follows from the same explanation as for the drop in thrust after a certain flight speed.

7.5 Practical Considerations for Propeller and Engine Installation

After the sizing of the propeller and the selection of the engine, the final consideration is the installation of the propeller as well as the engine to the power source. This is explained in more details below.

Electronic Speed Controller In order to connect the engine to the battery source, an electronic speed controller is required. Depending on the engine used, a particular electronic speed controller (ESC) is recommended by the engine manufacturer. For the hacker A60-14L motor, the "M Basic 90 - Opto " speed controller would be used. One important consideration during the installation of the ESC to the motor is that the motor on one side of the UAV has to rotate in the other direction. This can be achieved by connecting the positive end of the motor to the negative end of the ESC and the negative end of the motor to the positive end of the ESC.

Reverse Blade Geometry for Propeller Spinning in Other Direction The propellers which have to rotate opposite of its intended direction has to have its blades twisted in the other direction in order to produce a forward thrust. This is an important point to be taken into account when the propeller blades are to be purchased. It is noted that the manufacturer "XOAR International" provides custom made propellers according to customers specification and hence this problem can be rectified.

7.6 Engine Components and Propeller Characteristics

A summary of the engines and propellers which are compared and matched is provided in the table below. The selected engine and propeller are highlighted. It should be noted that two sets of engines and propellers will be purchased. The prices indicated are for one unit.

Table 7.2: Engine Characteristics.

Engine Characteristics	A60 -7SV2	A60-14L
Kv [RPM/Volts]	215	192
Ampere [A]	74	68
Voltage [Volts]	36	36
Maximum RPM	7000	7000
Maximum Rated Power [Watts]	2400	2600
Engine Mass [Kg]	0.595	0.910
Engine Length [mm]	62	80.4
Engine Diameter [mm]	60	59
Price [€]	255	299
Selected Engine		✓

Table 7.3: Propeller Characteristics.

Propeller data	XOAR PJH-E 21x13	XOAR PJH-E 21x14
Maximum RPM	7000	7000
Mass (approx) [g]	108	108
Diameter [mm]	533.4	533.4
Pitch [mm]	330.2	355.6
Material	Beechwood	Beechwood
Price [€]	27	27
Selected propeller		✓

The actual engine and propeller characteristics may vary according to different websites. These data are sought to be as accurate as possible. An illustration of the selected components are provided in figure 7.12 and 7.13.

Figure 7.12: Hacker A60-14L motor.

Figure 7.13: XOAR propeller.

The electronic speed controller which is to be used with the selected engine is the "Master Basic Spin 90 Pro Opto" controller. Its characteristics are as such; operating voltage of 12-50V, internal resistance of 2.2mΩ, maximum current of 90A and a mass of 105g.

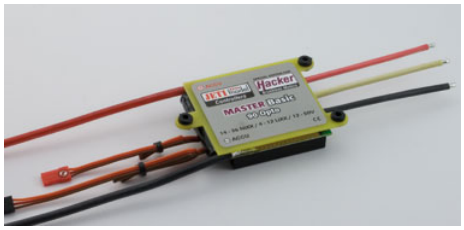

Figure 7.14: Master Basic Spin 90 Pro Opto controller.

7.7 Weight and Cost breakdown of Engine and Propeller Systems.

The weight and cost estimate of the combined engine and propeller system is presented in table 7.4.
The cost of the electronic speed controller would be presented in the cost and weight breakdown of the "Aircraft System" section.

7.8 Recommendations

It is recommended that the full propulsion set-up, which includes the batteries, electronic speed controller, engine and propellers, are tested on the ground before the actual flight test. The rpm of the engine should be varied in steps until its maximum operating rotation speed. A photoreflector

Table 7.4: Weight and Cost estimation

Items	Quantity	Cost [€]	Weight [Kg]
Hacker A60-14L	2	598	1.82
XOAR 21' x 14' propeller blade	2	54	0.216
Total Cost/Weight	-	642	2.036

and weighing scale could be used to measure the rpm and static thrust of the propeller at each point. A fuse should also be included between the connection of the batteries to the ESC, to avoid damage to the engine in case of excess current. During the test set-up, the temperature, current and voltage supplied to the engine should be measured.

8 Performance Analysis

In this chapter, the various performance characteristics of Tip-C are described. Data from the aerodynamics and propulsion department are inputted into the performance model to analyse Tip-C. The following performance characteristics are considered; stall speed, maximum speed, endurance, range, climb, descent, turn, landing and takeoff. For each performance aspect, the governing equations used in making the calculations are described and explained. The numerical results from these calculation are presented in section 8.10.

8.1 Endurance

The expression for the endurance of an electric powered aircraft is shown in equation 8.1 [29], where $\eta_{total} = \eta_{batt}\eta_{motor}\eta_{prop.}\eta_{esc}$:

$$Endurance = \frac{E_{batt}}{W} f_{usable} \frac{{C_L}^{3/2}}{C_D} \eta_{total} \sqrt{\frac{S\rho}{2W}} \tag{8.1}$$

8.2 Range

The expression for the range of an electric powered aircraft [29] can be found by multiplying equation 8.1 with the velocity term.

$$Range = \frac{E_{batt}}{W} f_{usable} \frac{C_L}{C_D} \eta_{total} \tag{8.2}$$

Equation 8.2 is also used to size the required battery capacity. Parameters like L/D and total efficiency are estimated. The additional power needed during takeoff, climb and descent is added to the battery capacity calculated from the range equation. The energy consumed during takeoff and climb is estimated by multiplying the required engine power during these phases with the estimated takeoff and climb time.

Equation 8.2 is also used to make the payload-range diagram. Unlike a fuel powered aircraft, there is no mass variation during flight. However, there is an exchange of payload mass with battery capacity instead of fuel in the payload-range diagram. The increase in battery capacity is estimated by multiplying the battery characteristic (184.26 Watt-hour per kg) with the change in payload mass. The payload-range diagram of the final design iteration is illustrated in figure 8.1.

8.3 Maximum Velocity

The maximum velocity is determined by either the intersection of the thrust/drag curves or the power available/required curves.
As seen in figure 8.2 and 8.3, the maximum level velocity of the final design iteration is 46m/s. From the thrust/drag and power curves, the maximum climb gradient and climb rate can be determined.

8.4 Stall Velocity

The stall velocity is determined using equation 8.3. A level flight is assumed during this calculation. The actual $C_{L_{max}}$ of the aircraft may differ slightly from the values generated by XFLR5 since the program cannot predict the lift coefficient near the stall AoA. A stall speed of 19m/s is found for the final design iteration.

$$V_{stall} = \sqrt{\frac{2W}{S\rho C_{L_{max}}}} \tag{8.3}$$

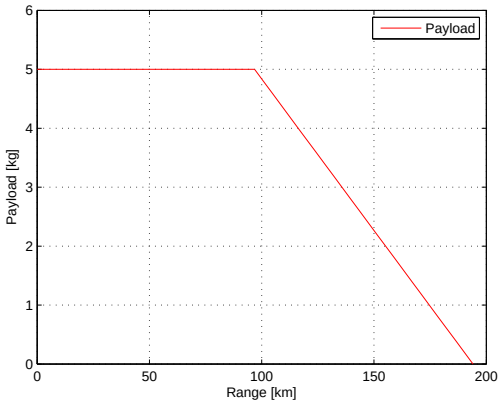

Figure 8.1: Payload-range diagram

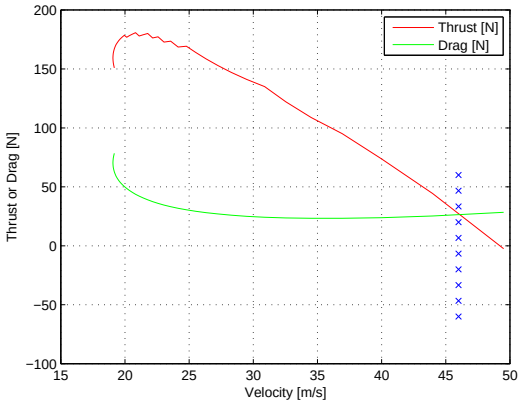

Figure 8.2: Thrust and drag vs. velocity.

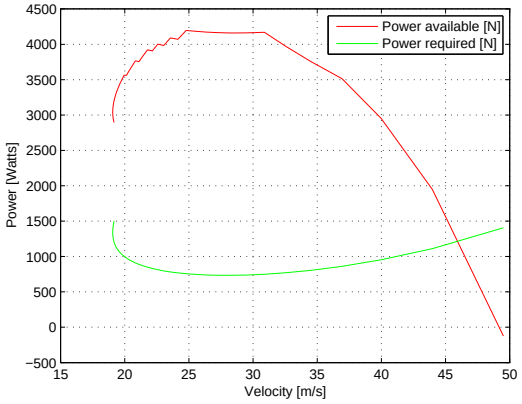

Figure 8.3: Power available and required vs. velocity.

8.5 Climb Performance

In this subsection, the climb performance of Tip-C is analysed. The two parameters to be considered are the maximum climb gradient and the climb rate. The optimal velocity and AoA for each operating point is calculated.

8.5.1 Maximum Climb Gradient

$$sin\gamma_{max} = \left(\frac{Tcos\alpha - D}{W}\right)_{max} \tag{8.4}$$

The formulation of equation 8.4 is based on the assumption of steady climb where acceleration is zero. D is a function of α and V and T is a function of V. In order to determine the climb gradient for each velocity point, the velocity for level flight (equation 8.5) at each specified AoA is used to determine the thrust and drag.

$$V_{level} = \sqrt{\frac{2W}{S\rho C_L(\alpha)}} \tag{8.5}$$

8.5.2 Maximum Climb Rate

By multiplying equation 8.4 with the velocity term on both side, the maximum climb rate can be calculated. This is presented in equation 8.6 below. The final iteration results are illustrated in figure 8.4 and 8.5. The maximum climb gradient/rate as well as the velocities and AoA for flying at that condition is specified in the 12 chapter.

$$RC_{max} = \left(\frac{TVcos\alpha - DV}{W}\right)_{max} = \left(\frac{P_a cos\alpha - P_r}{W}\right)_{max} \tag{8.6}$$

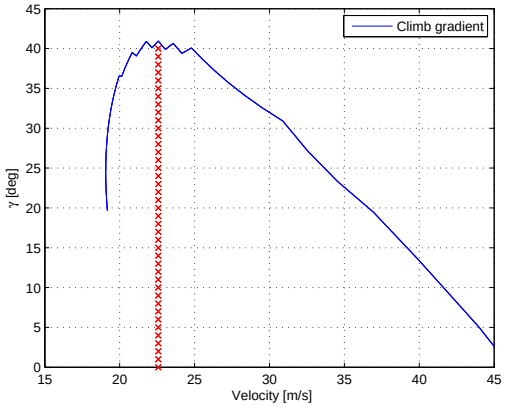

Figure 8.4: Climb gradient vs. velocity.

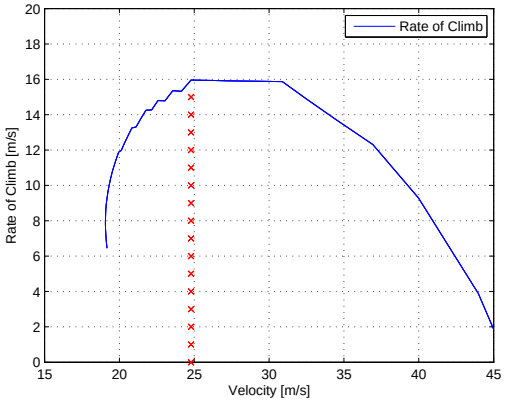

Figure 8.5: Climb rate vs. velocity.

8.6 Turn Performance

In this section, the turn performance of Tip-C is analysed. Firstly, the maximum load factor for each velocity point is determined. Then, the results from this calculation are used to determine the minimum turn radius and minimum time to turn.

8.6.1 Maximum Load factor

The maximum load factor is limited by two main things: the maximum lift coefficient, and the maximum thrust of the engine at each velocity point. In the case of a propeller powered engine, there is no analytical expression to determine the maximum load factor for the segment limited by the maximum thrust. This is because the maximum available thrust is a function of velocity. As such, the maximum load factor at each velocity point has to be obtained graphically. An illustration of the thrust versus drag curve with varying load factor is presented in figure 8.6. The resulting maximum load factor versus velocity plot is presented in figure 8.7.

8.6.2 Minimum Turn Radius

Equation 8.7 and 8.8 were used to derive the minimum turn radius as given in equation 8.9.

$$Lsin\mu = \frac{WV^2}{gR} \tag{8.7}$$

$$Lcos\mu + Tsin\alpha cos\mu = W \tag{8.8}$$

$$R_{min} = \frac{V^2}{g\sqrt{n^2 - (\frac{nW}{nW + Tsin\alpha})^2}} \tag{8.9}$$

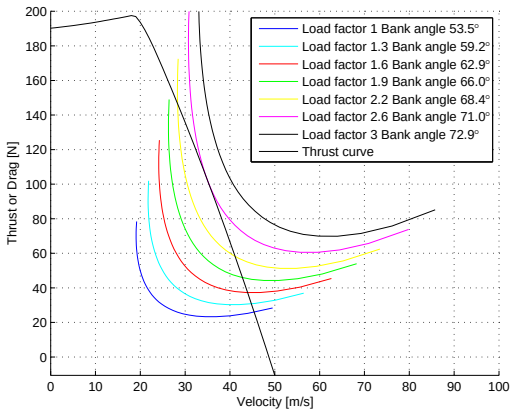

Figure 8.6: Thrust vs. drag curve for varying load factor.

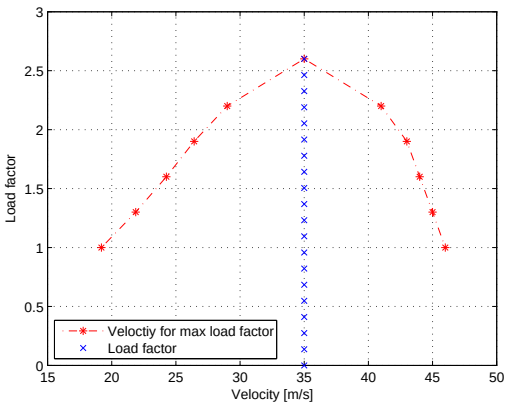

Figure 8.7: Achievable load factor vs. velocity.

Equation 8.9 is derived based on the assumption of horizontal sustained turn. This implies that the aircraft is making turns at level flight with no acceleration. In order to find the minimum turn radius, the maximum load factor at each velocity point is substituted into equation 8.9 to find the minimum turn radius. An illustration of the forces acting on the aircraft is illustrated in figure 8.8.

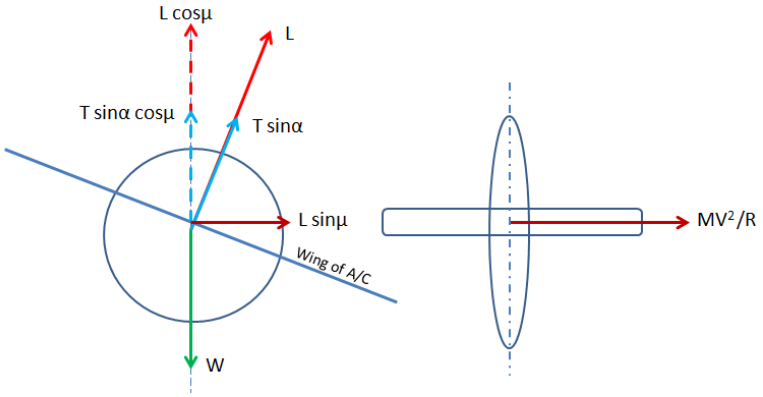

Figure 8.8: Free body diagram and kinetic diagram of a horizontal sustained turn.

8.6.3 Minimum Time to Turn

In this context, the minimum time to turn refers to the minimum time needed to complete one full circle. The results of equation 8.9 are substituted into equation 8.10 to solve for the minimum time to turn. The final results are illustrated in figure 8.9 and 8.10.

$$T_{min} = \frac{2\pi R_{min}}{V} \tag{8.10}$$

8.7 Descent Performance

In this section, the magnitude of the maximum descent gradient as well as the descent rate are determined. The velocity for maximum descent gradient and maximum descent rate are calculated and presented at the end (see table 16.1).

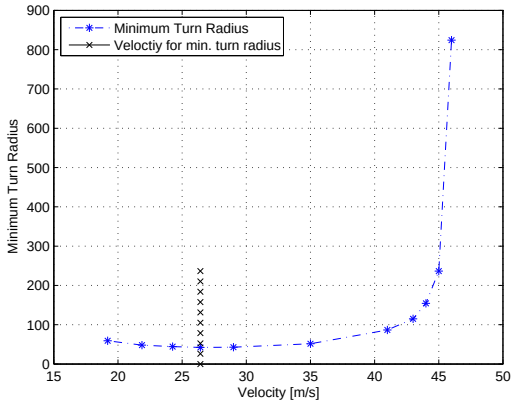

Figure 8.9: Min. turn radius vs. velocity.

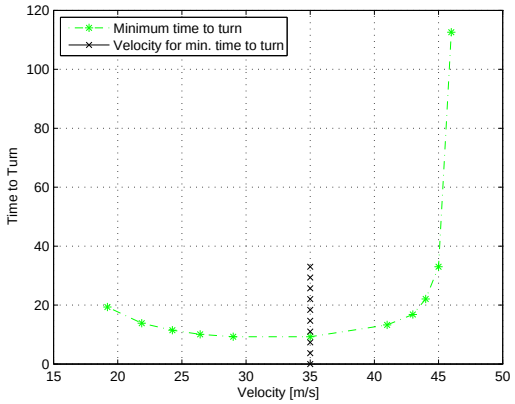

Figure 8.10: Min time to turn vs. velocity.

8.7.1 Maximum Steady Descent Gradient

The maximum descent gradient is derived based on the assumption of steady flight. Since the propulsion system runs is an electric engine, it is possible to shut off and start the engine easily during flight. Hence, the contribution of the propulsive force to the resultant aerodynamic forces can be neglected. The following equations of motion [28] result from these assumptions:

$$-D - Wsin\gamma = 0 \tag{8.11}$$

$$L - Wcos\gamma = 0 \tag{8.12}$$

$$tan(-\gamma)_{max} = tan(\gamma_d)_{max} = \left(\frac{C_D}{C_L}\right)_{max} \tag{8.13}$$

With the provided aerodynamic data, equation 8.13 can be used to solved for the maximum descent gradient. The velocity for maximum descent gradient is computed using equation 8.15.

8.7.2 Maximum Descent Rate

The results of equation 8.13 can be used to solve for the maximum descent rate. This is expressed in equation 8.14 [28].

$$RD_{max} = (V_d sin\gamma_d)_{max} = \left(\frac{V_d C_D cos\gamma_d}{C_L}\right)_{max} \tag{8.14}$$

where:

$$V_d = \sqrt{\frac{2Wcos\gamma_d}{S\rho C_L}} \tag{8.15}$$

The magnitude of the maximum steady descent gradient and descent rate are illustrated in figure 8.11 and 8.12. It can be seen that the maximum descent gradient corresponds closely to the stall speed of the aircraft. Also, the velocity for maximum descent gradient lies very close to the velocity for maximum steady descent rate.

8.8 Takeoff Performance

The takeoff manoeuvre consists of two parts: the ground run and the airborne segment. In the context of the UAV competition, a safety screen height of 10m is specified. This motion is illustrated in figure 8.13. For both segments of the flight, the analytical and numerical solution are described. In both solutions, the following assumptions are taken into account: the runway is flat, the presence of

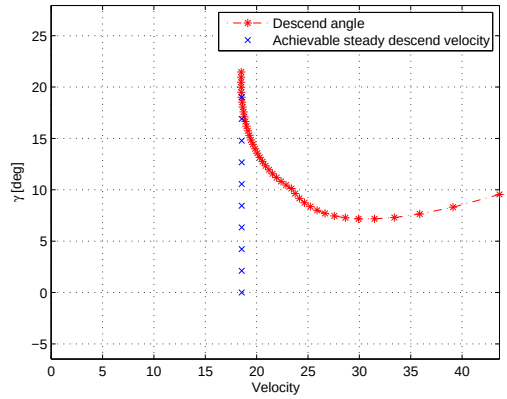

Figure 8.11: Achievable descent angle vs. velocity.

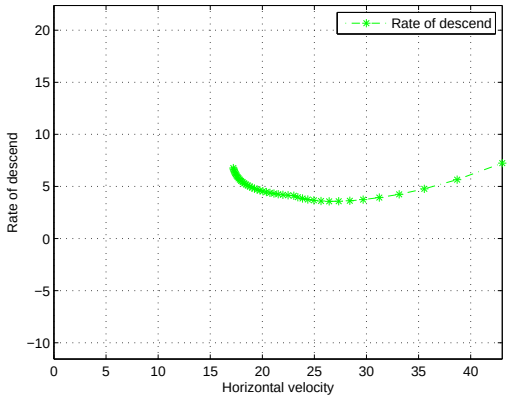

Figure 8.12: Achievable descent rate vs. velocity.

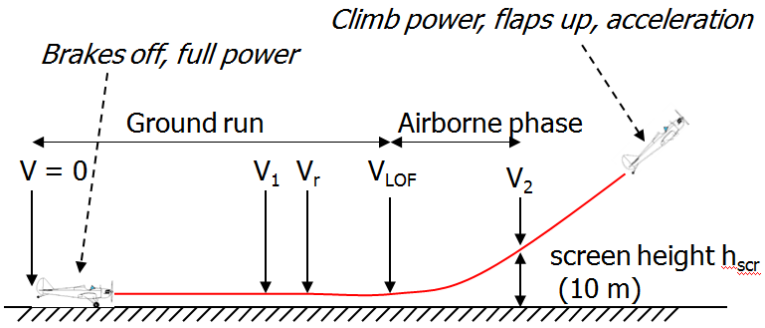

Figure 8.13: Takeoff motion.

wind and ground effects is neglectable. At the end of this subsection, the analytical solution is used to verify the numerical solution.

8.8.1 Analytical Solution

The analytical equation used for determining the ground run distance is given in equation 8.16 [30]. The aerodynamic drag term consists of contribution from the body, tail, belly flap and landing gear.

$$S_{g_{takeoff}} = \frac{W_{TO} V_{LOF}^2}{2g(\bar{T}cos\alpha - \bar{D} - \bar{D}_g)} \tag{8.16}$$

where $\bar{T}cos\alpha$, $\bar{D}$ and $\bar{D}_g$ typically occur at:

$$V_{av} = \frac{V_{LOF}}{\sqrt{2}} \tag{8.17}$$

The analytical equation used for determining the airborne distance is given in equation 8.18 [30].

$$S_{a_{takeoff}} = \frac{\frac{V_{scr}^2 - V_{LOF}^2}{2g} + cos\gamma h_{scr}}{sin\gamma_{scr}} \tag{8.18}$$

In the derivation of equation 8.18, a steady climb is assumed during the airborne phase. As the flight path angle, γ_{scr} increases, the $cos(\gamma_{scr})$ term becomes smaller and the $sin(\gamma_{scr})$ term becomes larger. This implies that a larger climb gradient leads to a smaller airborne distance.

8.8.2 Numerical Solution

The numerical solutions are based on the same governing equations used for deriving the takeoff analytical solutions. The main differences lie in the integration of the equations of motion [31]. The euler integration method is applied to determine the velocity, horizontal distance and height (if applicable) for every time step.

For both flight phases, an initial condition is specified accordingly. In the ground run phase, the initial velocity and horizontal distance are zero. In the airborne phase, the initial condition is based on the last time step of the ground run phase. The equation of motion for the ground run phase is given in equation 8.19. The AoA remains constant during the ground run phase. α is equal to θ since the velocity vector is always horizontal.

$$\frac{dV}{dt} = \frac{g}{W}(Tcos\alpha - D - D_g) \tag{8.19}$$

The euler integration method is applied to determine the velocity V, horizontal distance s and pitch angle θ for each time step:

$$V(i) = V(i-1) + \frac{dV}{dt}(i-1)\Delta t \tag{8.20}$$

$$s(i) = s(i-1) + V(i-1)\Delta t \tag{8.21}$$

The condition that the aircraft starts pitching only after it exceeds the rotation speed V_R is applied. The values of $\frac{d\theta}{dt}$ and V_R are specified through trial and error depending on the shortest takeoff distance. $\frac{d\theta}{dt}$ is a constant.

$$\theta(i) = \theta(i-1) + \frac{d\theta}{dt}(i-1)\Delta t \tag{8.22}$$

The governing equations of motion for the airborne phase are given in equation 8.23 and 8.24. These are also used to derive the analytical airborne distance given in equation 8.18.

$$\frac{W}{g}\frac{dv}{dt} = Tcos\alpha - D - Wsin\gamma \tag{8.23}$$

$$\frac{WV}{g}\frac{d\gamma}{dt} = L + Tsin\alpha - Wcos\gamma \tag{8.24}$$

The euler integration method is again applied to determine the velocity V, horizontal distance s, height h, flight path angle γ and pitch angle θ for each time step. The velocity and pitch angle are computed, based on the same formulation given in equation 8.20 and 8.22. The height and the flight path angle are computed based on the following equations:

$$h(i) = h(i-1) + V(i-1)sin(\gamma)\Delta t \tag{8.25}$$

$$\gamma(i) = \gamma(i-1) + \frac{d\gamma}{dt}\Delta t \tag{8.26}$$

In equation 8.26, the value of $\frac{d\gamma}{dt}$ is determined from equation 8.24. The AoA varies with respect to time during the airborne phase. The value of α at the current time step depends on the pitch angle and the flight path angle. During the airborne phase, the value of α is calculated as such:

$$\alpha(i) = \theta(i) - \gamma(i) \tag{8.27}$$

The results of the final design iteration for takeoff are illustrated in figure 8.14 and 8.15. A screen height of 10m is used as the breaking point for the entire takeoff flight path.

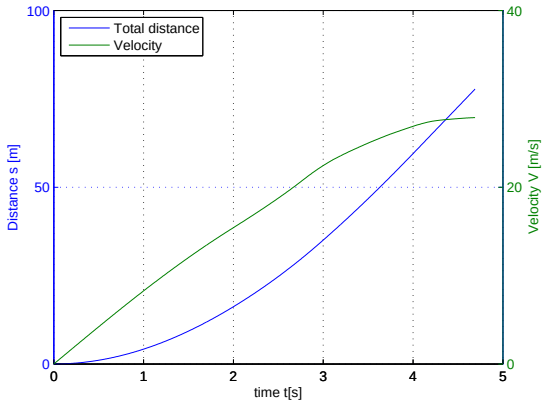

Figure 8.14: Velocity and distance profile versus time.

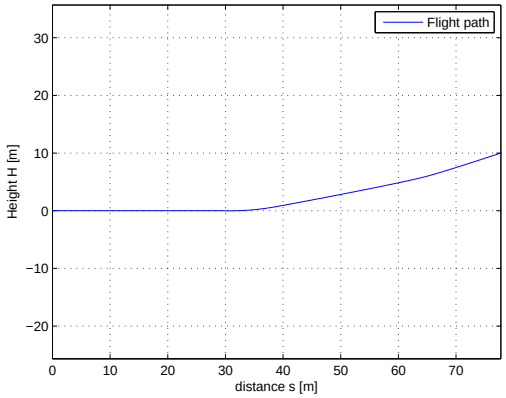

Figure 8.15: Takeoff flight path.

8.8.3 Verification

In order to check the validity of the numerical solutions, the results of the numerical simulation are verified with the analytical solutions. The analytical solutions require some input parameters. Parameters such as the liftoff velocity, screen height velocity and the flight path angle at screen height are defined. As such, the initial conditions applied, as well as the intermediate results from the simulation are used as inputs for the analytical solution. Not all of the input parameters can be obtained directly from the simulation results. Therefore, certain parameters are estimated, which results in minor discrepancies between the analytical and numerical solution.

Table 8.1: Total takeoff distance of analytical and numerical solution

Parameters	Analytical Solution	Numerical Solution
Total takeoff distance	78.22	77.76

From table 8.1, it can be seen that the results of both solutions are sufficiently close to confirm the accuracy of the numerical results.

8.9 Landing Performance

The landing motion consist of three phase. The first phase is the approach phase. This is followed by the flare phase and finally the ground roll phase. An illustration of the motion is provided in figure 8.16.

In the approach phase, the flight path angle is assumed to be constant. The flight path angle begins to decrease from the start of flare to touchdown. The magnitude of the final flight path angle has an influence on the overall landing distance. The smaller the final flight path angle, the larger the landing distance. This can easily be understood by visualising the entire landing trajectory.

This final flight path angle depends greatly on the allowable forces on the landing gear. A larger descent gradient at touchdown implies a larger impact force on the landing gear. This final descent gradient depends largely on the flare height. The larger the initial flare height, the smaller the final descent gradient since more time is provided for the aircraft to pitch up.

For all segments of the flight, the analytical and numerical solution are described. The same assumptions as for takeoff are considered. The effect of wind and ground effect are not taken into

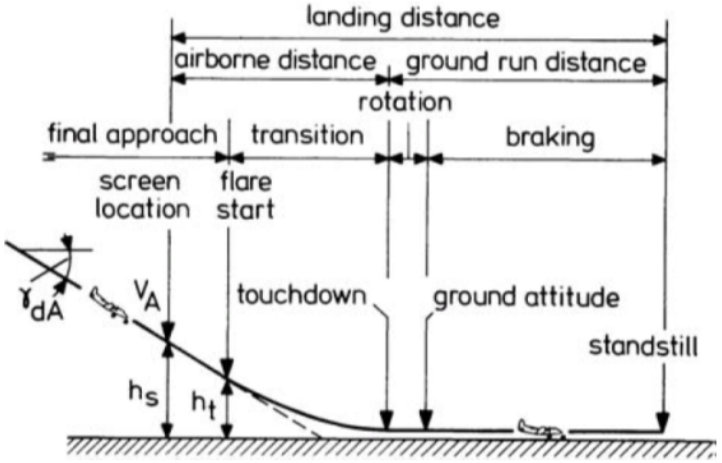

Figure 8.16: Landing motion.

account and the ground is assumed to be flat. For the analytical solution, the landing motion is split into an airborne and ground roll phase. As for the numerical solution, all three flight phases as described above are taken into account.

8.9.1 Analytical Solution

The airborne distance is calculated from equation 8.28 [30]. This equation is derived based on the assumption of steady flight during approach and zero thrust during touchdown.

$$S_{a_{land}} = \frac{\frac{V_A^2 - V_T^2}{2g} + cos\gamma_A h_{scr}}{\frac{1}{2}\left(sin\gamma_A + \left(\frac{C_D}{C_L}\right)_T\right)} \tag{8.28}$$

In equation 8.28, the drag coefficient at touchdown includes the contribution of the body including tail, landing gear and belly flap. The lift coefficient at touchdown includes the contribution of the main body and the belly flap. The formula for determining the ground run distance is given in equation 8.29.

$$S_{g_{land}} = \frac{WV_T^2}{2g(\bar{D} + \mu_r(W - L))} \tag{8.29}$$

Similar to the ground run equation for takeoff, the aerodynamic drag term in equation 8.29 consists of contribution from the body, belly flap and the landing gear. The aerodynamic drag and ground friction are calculated based on the average velocity during the ground run phase.

$$V_{av_{land}} = \frac{V_T}{\sqrt{2}} \tag{8.30}$$

8.9.2 Numerical Solution

The numerical solutions are based on the same governing equations used to derive the analytical solution [31]. The governing equations for the approach and flare phase are the same. They are presented in equation 8.31 and 8.32. The only difference is that the descent gradient remains constant during the approach phase.

$$\frac{W}{g}\frac{dV}{dt} = Tcos\alpha - D + Wsin\bar{\gamma} \tag{8.31}$$

$$-\frac{WV}{g}\frac{d\gamma}{dt} = L - Wcos\bar{\gamma} + Tsin(\alpha) \tag{8.32}$$

With equation 8.31 and 8.32, the euler integration method is applied to determine the velocity V, flight path angle γ, AoA α, pitch angle θ, horizontal distance s and height h at each time step during the landing phase. The thrust terms in equation 8.31 and 8.32 are set to zero in the program since it is realistic to assume that the thrust force is negligible during landing. The equations for determining the velocity and pitch angle are the same as the one given in equation 8.20 and 8.22.

The expressions for determining the height and horizontal distance at each time step during the airborne phase are given in equation 8.33 and 8.34.

$$h(i) = h(i-1) + \frac{dh}{dt}\Delta t = h(i-1) - V(i-1)sin(\gamma)\Delta t \tag{8.33}$$

$$s(i) = s(i-1) + \frac{ds}{dt}\Delta t = s(i-1) + V(i-1)cos(\gamma)\Delta t \tag{8.34}$$

A minus-sign is indicated in equation 8.33 since the aircraft is descending during the landing phase. The governing equation for the ground run phase is presented in equation 8.35.

$$\frac{W}{g}\frac{dV}{dt} = Tcos\alpha - D - \mu_r(W - L) \tag{8.35}$$

Similar to the governing equations for the airborne segment, the thrust term is set to zero for the ground roll simulation of the landing phase. This is a realistic assumption, considering the fact that the engine is throttle off during the landing phase. The euler integration method is again applied to determine the velocity, and horizontal distance for each time step. The results of the landing simulation are illustrated in figure 8.17 and 8.18.

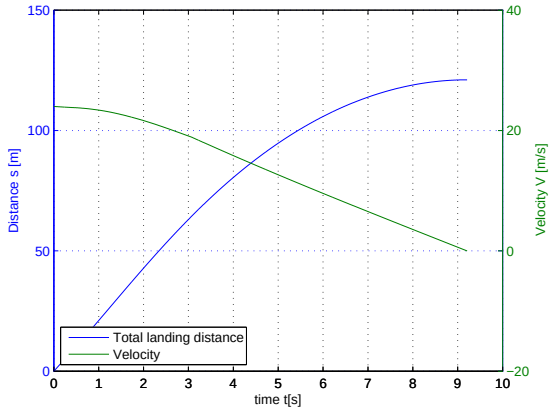

Figure 8.17: Velocity and distance profile vs. time

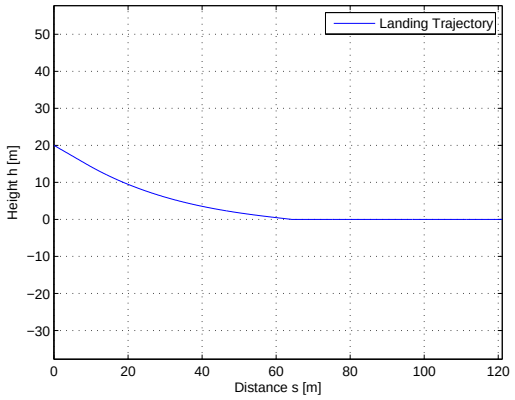

Figure 8.18: Landing flight path

Looking closely at the velocity profile in figure 8.17, it is noted that the velocity remains almost constant during the approach phase. The moment the aircraft starts to flare, the AoA increases and the aircraft velocity reduces accordingly. When the aircraft touches down, the velocity reduces linearly to zero. This velocity profile is expected during the landing phase if one compares this with the actual landing sequence.

The landing simulation was experimented initially with two different flare heights; 15m and 10m. It was found that both the final descent gradient and touchdown velocity reduce when the start of flare was initiated at a higher altitude. As such, it is beneficial to initiate flare at a higher altitude to have lesser impact load on the landing gear. The actual landing distance is calculated from the start of the 10m screen height to the last distance point irrespective of the starting flare point and initial approach height.

8.9.3 Verification

The numerical solution for the landing phase is verified with the analytical solution. As previously mentioned, the input parameters needed to calculate the analytical landing distance are partially obtained from the intermediate results of the numerical solution. Differences between both solutions still exist, since parameters such as the drag and lift coefficient at touchdown are estimated.

Table 8.2: Total landing distance of analytical and numerical solution.

Parameters	Analytical Solution	Numerical Solution
Total landing distance	114.15	102.24

From table 8.2, it can be said that the results of both solutions are sufficiently close to confirm the accuracy of the numerical results. The difference in results between both solutions is less than 10%.

8.10 Results

The performance analysis of Tip-C with the initial engine configuration (Hacker A60-7SV2 and XOAR 21' x 13' propeller) is presented in table 8.3. Certain design requirements are not met. The requirements not met are the range and climb gradient. The maximum level velocity is close to the cruise speed of Tip-C. This speed is calculated based on the lift coefficient for maximum L/D.

The propulsion system is initially designed based on a cruise speed of 30m/s. This is subsequently altered to 37m/s due to the change in aerodynamic data along the design. It was also discovered later that the climb gradient requirements are not met with the current propulsion system.

As such, it is decided within the group to increase the power/thrust of the engine. The propeller blade pitch has to be increased in order to accommodate the larger operating speed of Tip-C. The performance analysis of the final design is presented in Chapter 12. The performance parameters of the initial design is presented in table 8.3.

Table 8.3: Requirement compliance table for first design.

Performance Parameters	Values	Velocity [m/s]	AOA [deg]	Design Req.	Req. met?
Range [Km]	58.86	36.93	2	75	No
Endurance [Hours]	0.52	28.29	8	-	-
Maximum climb gradient [deg]	21.93	21.77	15	30	No
Maximum climb rate [m/s]	8.9	24.79	12	-	-
Maximum descent gradient [deg]	19.01	18.54	35	30	No
Takeoff distance (Analytical) [m]	103.64	-	-	120	Yes
Takeoff distance (Numerical) [m]	98.7	-	-	120	Yes
Landing distance (Analytical) [m]	114.10	-	-	150	Yes
Landing distance (Numerical) [m]	102.24	-	-	150	Yes
Maximum Velocity [m/s]	39.5	-	-	-	-
Stall Velocity [m/s]	19	-	-	-	-
Maximum Load factor	1.94	35	-	-	-
Minimum Turn radius [m]	44.35	24	-	-	-
Minimum time to turn [s]	10.75	26	-	-	-

8.11 Sensitivity Analysis

Besides the change in propulsion system, changes in other design parameters are considered. Qualitatively, some aspects of the sensitivity analysis are discussed. The overall lift coefficient of the UAV could be increased in order for it to fly at a lower cruise speed. Increasing the wing area also helps in reducing the overall cruise velocity. An increase in wing area leads to lower wing loading and thus shorter takeoff distance. However, a higher wing loading is beneficial for climb performance. As such, changing the wing area has a conflicting effect on various design requirements.

Finally, the increased engine power extends the difference between the cruise speed and the maximum speed for the final design iteration. The cruise speed of Tip-C is still rather large considering its weight and size. An airfoil with steeper lift slope and higher $C_{L_{max}}$ would be beneficial for cruise and especially for takeoff and climb performance. Increasing the AR of the UAV leads to higher L/D and thus better cruise, climb and takeoff performance. Lowering the total mass of the UAV would be beneficial in terms of increased range, endurance and better climb performance.

8.12 Recommendations

The effect of altitude variation on the thrust and drag curves as well as its effect on the turn performance of Tip-C could be further investigated. The effect of altitude is not taken into account in this project since Tip-C is expected to operate at an maximum altitude of 200m. Also, the simulation of the other flight phases during climb, descent and turning could be developed. The takeoff simulation model could also incorporate the case of a one engine failure. The presence of wind as well as ground effect could be taken into account in this model.

9 Landing Gear

A key component in any aircraft design is the landing gear. Its purpose is to provide clearance between aircraft and ground during taxi/takeoff and absorb the kinetic energy of the vertical velocity component during touchdown. This chapter first discusses the configuration of the landing gear, followed by the positioning and sizing of the struts, shock absorbers, tyres and brakes. After this, the retraction mechanism is elaborated and the total assembly is presented. The chapter is concluded with a cost and weight estimate, sensitivity analysis, verification and validation and recommendations.

9.1 Configuration

In the landing gear design, the decision made is to use a retractable tricycle gear as it provides the best cruise performance for the low AR UAV design. The fact that the c.g. is relatively far in the front makes the tail dragger configuration a suitable solution as well. However, due to its unstable ground behaviour and the hazard of tipping over[32], the tricycle configuration is regarded as the best option.

9.2 Positioning

To provide stability to the aircraft when operating on the ground, the placement of the three members of the landing gear is crucial. The configuration influences the load distribution over the different members during various manoeuvres. These motions can be split in two components: longitudinal and lateral. From [33, 34] it is found that the static load on the nose wheel is between 8-15% of the total weight of the aircraft. The reason for this load distribution is to make sure the nose wheel has enough pressure on its contact patch to provide enough friction to make turns and such that the main wheels can provide sufficient braking force when landing. The static load on the nose wheel is dependent on the position of both the main gear and nose wheel with respect to the c.g. Figure 9.1 indicates the position of the wheels with respect to the c.g. The static load on the nose wheel is then given by:

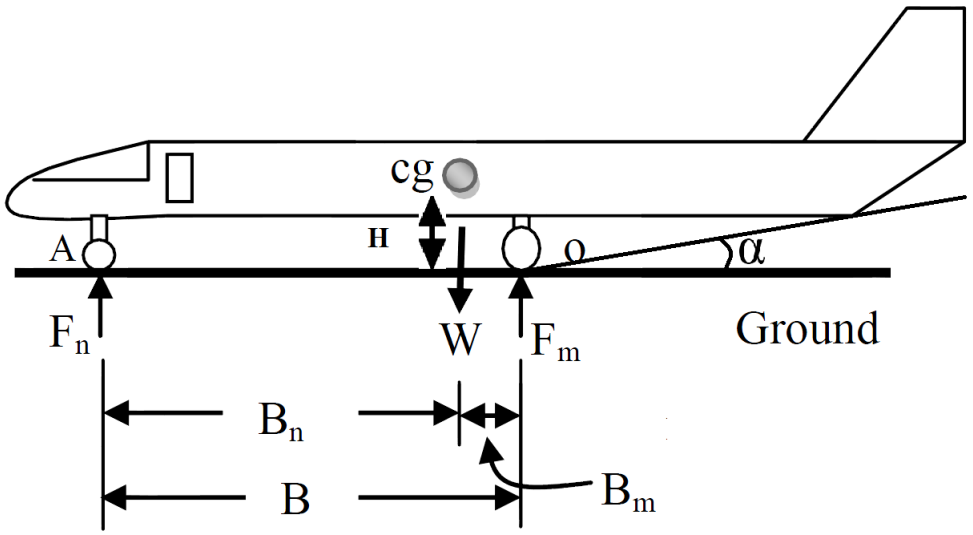

Figure 9.1: Representation of the position of the nose wheel and main landing gear to the c.g. Picture is modified from [24].

$$F_n = \frac{B_m}{B} \cdot W \tag{9.1}$$

The c.g. is preferred to be as forward as possible for stability. Located at 0.29m from the tip, the positions of the the nose wheel and main landing gear can be determined. By placing the nose wheel at 0.02m from the nose and the main landing gear at 0.32m from the nose, the resulting load on the nose wheel is 10% of the total weight, which is in compliance with conventional load distributions[33, 34]. Given the longitudinal position of the gears, the lateral position can be determined. The lateral position is determined by the turnover angle, which is indicated in figure 9.2. In figure 9.2, one can

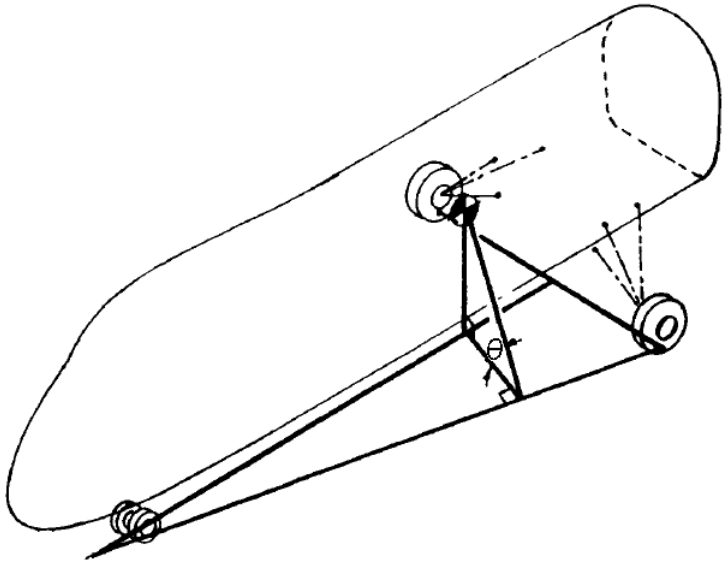

Figure 9.2: Turnover angle[34].

observe that the turnover angle depends on the height of the c.g. and the distance of its projection on the ground to a line between nose and main wheels. In order to alter this angle, there are two options; either change the c.g. height, or change the c.g.s distance to the line connecting nose and main wheels. The c.g. height from the ground will be first discussed. The height is determined by the difference between the c.g. location of the main body and the part of landing gear touching the ground. Two considerations have to be taken into account for the height of the c.g. The first consideration is the clearance between propeller and ground. It is assumed that the propeller's line of action acts through the c.g. in order to avoid creating any moment due to thrust. Given a propeller diameter of 0.55m and implementing an additional safety margin of 0.05m, the minimum length of the struts should be 0.28m in all conditions. Due to the inward compression of the shock absorber, which is discussed in section 9.4, 4cm is added to the static length, resulting in a total height of 0.32m. To determine whether this length is actually sufficient, the maximum rotation angle (α in figure 9.1) must be evaluated as well. Given the 0.32m height and the longitudinal position of the main landing gears, the highest possible rotation angle can be evaluated. Given these two parameters, the maximum rotation angle is computed to be 25° which is sufficiently high for a range of pitch angular velocity. Low turnover angles correspond to lower chances of turning over[34], hence one would like to minimise this turnover angle. To investigate on ways of lowering this angle, one should evaluate the definition of the turnover angle, as given in equation 9.2.

$$\theta = \arctan \frac{\textit{c.g. height}}{\textit{c.g. location distance to turnover line}} \tag{9.2}$$

To lower this angle, the distance between the c.g. and turnover line must be increased. To do so, the main wheels should be positioned more sidewards. For a value of 0.425m from the centre line of the aircraft, an overturn angle of 57° was found. According to [34, 33], the turnover angle should not exceed 63° for land-based aircraft. This 0.425m offset from the centre line is therefore sufficient to fulfil this requirement.

9.3 Strut Sizing

Now that the configuration and length of the struts is determined, the next step in the design phase is to size the diameter of the struts such that it can bear the impact loads during landing. Due to considerations for the shock absorbing properties of the landing gear, discussed in section 9.4, the shape of the struts is assumed to be a hollow cylinder. These struts experience three different load cases: static load when the aircraft is at rest on the ground, the impact load at touchdown and finally the deceleration load during the ground run phase of landing. These three load cases can be split up into two parts; the axial load of both the static load and touchdown and the bending moment combined with the load transfer to the front wheel. The maximum axial load during both static and touchdown manoeuvres will first be investigated. It was found that the maximum load factor can be as high as 3.0[33] during landing, which results in a total load of 647N. Since it is likely that touchdown on one of the struts can occur, each landing gear should be designed to withstand loads up to 647N. The maximum axial load on the nose wheel is experienced during the period of deceleration to a full stop. In this case, the weight of the aircraft is 'transferred' to the nose wheel. The braking forces at the wheels create a moment around the c.g., which is compensated by the reaction normal forces at the main wheels. This 'transfers' some of the load from the main wheels to the nose wheel. The maximum axial load at the nose wheel is given by equation 9.3, where the dimensions are given in figure 9.1.

$$F_n = F_{n_{static}} + \frac{F_{brake} \cdot h}{B} \tag{9.3}$$

Given a deceleration value of 3 m/s, which is a common value according to [34, 33], the maximum load on the nose wheel is 94 N. The normal stress is than given by[35]:

$$\sigma = \frac{F}{A} = \frac{F}{\pi({R_{outer}}^2 - {R_{inner}}^2)} \tag{9.4}$$

The maximum normal stress due to the the braking forces is given by[35]:

$$\sigma = \frac{M \cdot y}{I} \tag{9.5}$$

If the normal stress due to the dynamic load is added to the result of equation refeq:bending, the maximum normal stress during braking can be computed. The highest stresses in the main landing gear occur during touchdown and the highest loads on the nose wheel occur during braking. By implementing an additional safety factor of 1.5, the diameter of the struts can be computed to withstand the axial and bending loads.

9.4 Shock Absorber

One of the most crucial aspect in the design of the landing gear is that it should withstand the loads at touchdown as well as to absorb the vertical kinetic energy. In order to do so, different solutions such as steel springs, liquid springs, shock absorbers and oleo-pneumatic systems are possible. From [34], it is found that both the liquid spring and oleo-pneumatic spring are the most efficient(75-80%). However, when comparing the weights of the two types, the oleo-pneumatic system is the most optimal

option. The oleo-pneumatic shock absorber consists of a piston that moves through oil to get rid of the energy. At the top, there is a chamber filled with gas(usually dry air of nitrogen) which acts as a spring. The shock absorber gets rid of the energy by performing work. The load during impact makes the piston deflect, in which energy is dissipated. This work is not only performed by the strut itself, but also by the tyre touching the runway since it also partially compressed during touchdown. In order to size the total deflection needed for the piston, the following relation has to be solved:

$$\frac{1}{2} \cdot m{V_{vertical}}^2 = \mu_{oleo} \cdot F_{touchdown} \cdot s_{strut} + \mu_{tyre} \cdot F_{touchdown} \cdot s_{tyre} \tag{9.6}$$

Equation 9.6 shows that the stroke length is dependent on the impact load during landing, the efficiency of the shock absorber(μ) and the vertical component of the velocity. The vertical energy is a function of both the total velocity as well as the descent angle. Those two parameters have to be taken into account when designing the stroke of the shock absorbers, the total movement of the cylinder inside the shock absorbers. From [34] it is found that the oleo-pneumatic absorber has an efficiency of 80 percent, while the tyre has an efficiency of 47% which is independent of the tyre size. Taking into account these efficiencies, introducing a load factor of 3.0 and expressing the vertical velocity as a function of the descent angle, equation 9.6 can be re-expressed as:

$$\frac{1}{2} m(V_{approach} \cdot \sin(\gamma))^2 = 0.8 \cdot 3.0W \cdot s_{strut} + 0.47 \cdot 3.0W \cdot s_{tyre} \tag{9.7}$$

From the performance analysis 8, it was found that the velocity at touchdown is about 21m/s and the flight path angle is about 7°. With this data, the kinetic energy to be absorbed can be computed. In order to have a safety margin for the computation stroke length, the tyres are assumed to be inelastic. Taking into account these considerations, the total stroke length is found to be 0.14m.

9.5 Tyres and Brakes

The next step in the design of the landing gear is the tyre and brakes. The goal of this design process is to *select* the most suitable tyres and brakes, rather than to *design* the two components. This section discusses on the selection criteria for both the tyres and brakes.

9.5.1 Tyres selection

Tyre selection is predominantly influenced by the static load the tyre has to carry, as well as the dynamic load[34, 33, 24]. The sizing is usually performed in a statistical way, which gives a good indication on what the rough dimension of the outer diameter and the width of the tyre should be. Given this first indication, one can look into the data sheets of manufactures to find a tyre that can handle both the static and dynamics loads. To give a first indication on the dimensions of the tyres to be used, the statistical method generated by Raymer [36] is used. It relates the dimensions of the outer diameter and the width of the tyre to the weight on the tyres. This relations are displayed by equations 9.8 and 9.9.

$$diameter = 1.51 \cdot {W_{static}}^{0.349} \tag{9.8}$$

$$width = 0.715 \cdot {W_{static}}^{0.312} \tag{9.9}$$

Since these empirical relations are derived from data in imperial units, the weight must be converted to pounds and the given dimensions are in inches. Taking into account the static weight of the landing gear tyres, the following dimension were found:

A quick check at the traditional aircraft tyre producers, Michelin and Goodyear, revealed that the smallest tyres these manufactures produce are too big(radii of 10+ inch) for the purpose of this design. The allowable static loads of these tyres are too high[37] by the given design constraint.

Table 9.1: Dimension of the main and nose wheels respectively using Raymer's [36] statistical approach.

	Main gear	Nose wheel
Diameter (inch)	4.5	2.0
Width (inch)	1.9	0.9

It is therefore more convenient to search on websites that specialise in large radio-controlled aircraft. These aircraft has comparable weight as Tip-C and the their landing gears are easily available. These landing gears come in different sizes and are always available. Since it might not be able to buy the tyres in exactly the same dimensions as estimated, the tyres are selected in such way that the dimensions are equal or bigger than the ones computed.

9.5.2 Brakes Selection

Apart from handling the static and dynamic normal loads, the tyres have to provide braking force as well. In order to do so, a friction force between the tyre and surface has to be induced which creates a torque around the spin axis of the wheel. This torque has to be created by the braking system. This is performed by bringing to the brake shoes in contact with the internal surface area of the wheel rim. A pressurised air cylinder is used to pressurise the brake shoe on the wheel rim in order to create a braking force. By increasing or decreasing the pressure inside the system, the braking force can be either increased or decreased.

9.6 Retraction Mechanism

To improve the overall performance of the aircraft, the landing gear has to be retracted inside the aircraft body. In order to do so, multiple kinematic concepts are developed, varying from simple to complex. For the UAV to be designed, the concept displayed in figure 9.3 is chosen. The reasons for

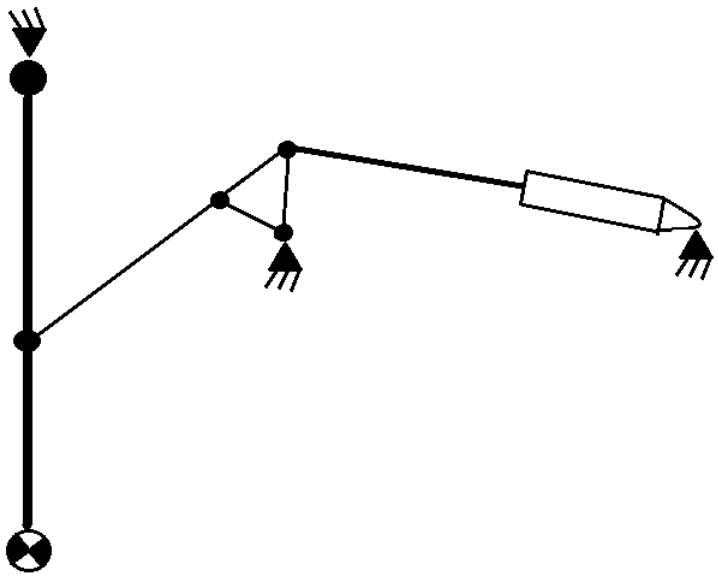

Figure 9.3: Kinematic concept retraction mechanism for Tip-C.

selecting this mechanism is that it is relatively simple to analyse and that it fits well within the body. Also, the actuator needed to retract the landing gear is available on the market. The reason why

the mechanism has to be simple is the fact that the motions of all components has to be analysed in great detail to size the required actuator force and displacement. Since multiple links would lead to more complex simulation, the decision was made to design a relatively simple mechanism, given the time and resources available. The mechanism in figure 9.3 operates as follows. The actuator body on the right side in attached to the aircraft internal structure. The piston pin is connected to a rotating triangle. When the actuator piston transverse horizontally, the triangle starts to rotate about its own connection point with the aircraft. Since the landing gear strut is also connected to this triangle, the landing gear can be retracted or deployed. The main gears retracts within the centre of the body such that the height of the aircraft c.g. changes only and the longitudinal position of the c.g. remain unchanged. For the nose wheel, this was not an option as the c.g. moves to the back when the landing gear is retracted. More details on how this mechanism is sized are given in section 9.6.1

9.6.1 Sizing

Once the design of the retractable landing gear mechanism is known, the dimensions need to be determined. This subsection discusses the method used to determine the dimensions and the calculation for the actuator. The results of this analysis will be discussed too. In order to save time, the ratios of the dimensions of the landing gear are the same reference landing gear as discussed in the previous sections. In order to make it specific for this design, an optimisation is done on these parameters.

Method

A numerical analysis is carried out for the landing gear design in order to calculate the force required to retract the landing gear and deploy it. Figure 9.4 shows a drawing of the landing gear mechanism with its dimensions.

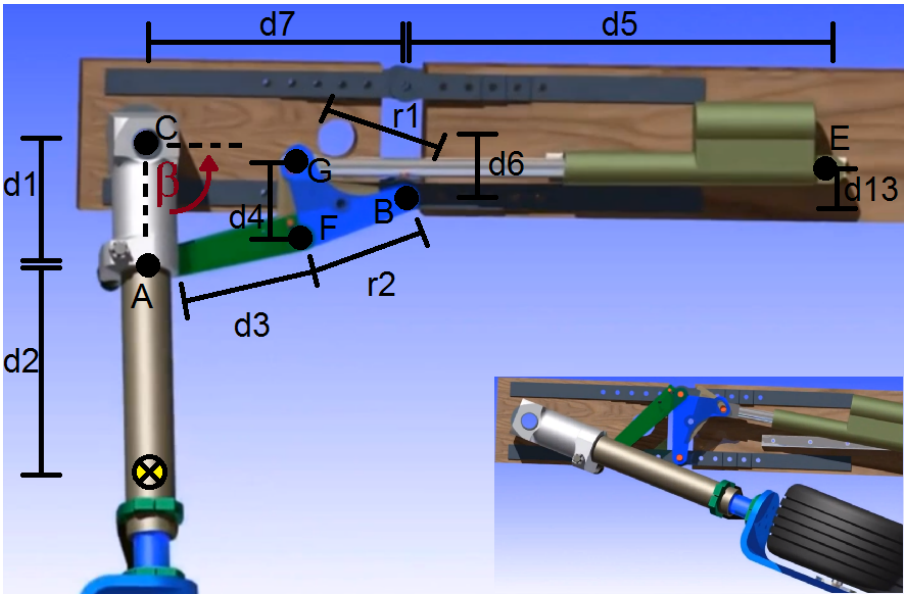

Figure 9.4: Visualisation of the landing gear in deployed and partly retracted position.

For this analysis, some assumptions are made to simplify the calculations.

- The intersection at point A is in the middle of the rod

- The locking system is not taken into account
- The friction of the hinges is neglected

Every rotating hinge and rods are a function of the angle of the landing gear with respect to its horizontal line. The landing gear angle varies between 0°and 90°. By using the cosine rule (equation 9.10) and the sine rule (equation 9.11), every angle and length between two hinges is determined as a function of β.

$$c^2 = a^2 + b^2 - 2 \cdot a \cdot b \cdot \cos(\gamma) \tag{9.10}$$

$$\frac{a}{\sin(\alpha)} = \frac{b}{\sin(\beta)} = \frac{c}{\sin(\gamma)} \tag{9.11}$$

See figure 9.5 for the definition of the sides and angles.

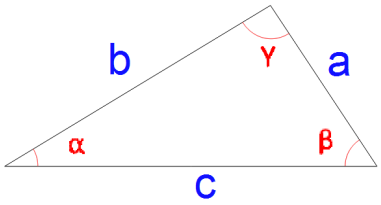

Figure 9.5: Triangle for visualisation of angles and sides [38].

In order to find the maximum force required during the whole process of retracting the landing gear, an iteration is done for the angle of β. The more iterations is done, the more accurate the results are. In the next section, the results are given for a numerical analysis with 100 iterations.

Results

In this part, the results are given and visualised in a graph. Figure 9.6 shows the force required to retract the landing gear. A maximum force of 44 N is required at the most retracted configuration (close to 90 degrees).

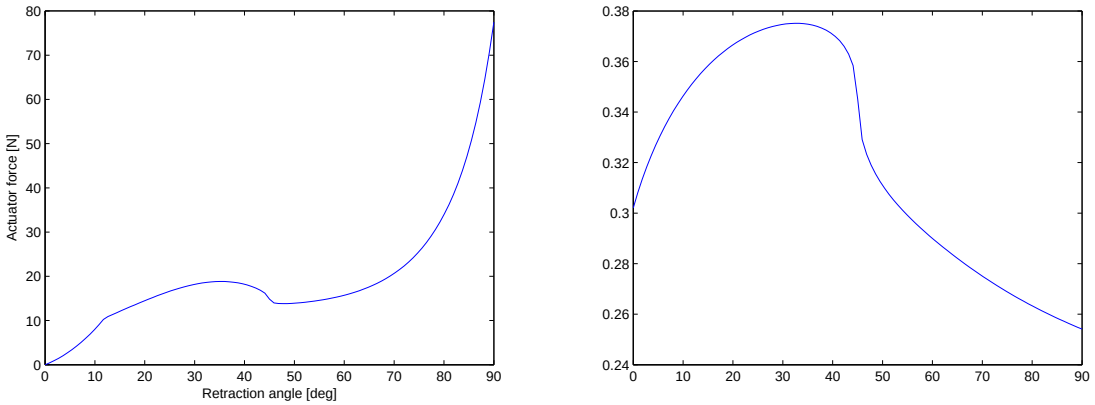

Figure 9.6: Graph of retraction angle vs. actuator force required (left) retraction angle vs. actuator length required (right).

The other parameter which is of great interest is the displacement of the actuator rod. The results of the actuator rod length are given in figure 9.6. From this data, the displacement can be determined. The maximum displacement is the distance between the maximum and minimum length of the actuator rod. From figure 9.6, it can be seen that the maximum and minimum length are 0.335 m and 0.202 m respectively. The minimum displacement required is 0.133 m.

Discussion of Results

From the first set of results (required actuator force vs. retraction angle), the graph in figure 9.6 shows a local maximum close to a retraction angle of 30°. This phenomena is due to the dynamic properties of the mechanism. As the angles and positions of the rods changed, the resulting moment arms also change. The change in moment arm length increases the force required on a certain rod to keep the mechanism moving. In section 9.6.2, the required actuator force is optimised by changing the different input variables which are given in figure 9.4. As seen in figure 9.6, the actuator rod is changing its length in a different way than what would be expected. Its length is first increasing follow by decreasing. Although this phenomena is possible in theory, it is very difficult to achieve this physically. This phenomena occurred due to the assumptions made at the beginning of the sizing. Hinge A (see figure 9.4) is located in the middle of the rod for the calculations while the original design states this hinge to be on the left side of the rod. This can be easily noticed in figure 9.4. The displacement of the actuator rod depends on the availability of resources. If a actuator of 0.14 m displacement is available, the design can be slightly changed in order to achieve this length.

9.6.2 Sizing Optimisation

In order to have a more efficient mechanism, the mechanism parameters are optimised such that an actuator which used the least space and force is required. In this subsection, the method, results and conclusion are discussed.

Method

In order to optimise this system, the variables which change the outcome are first isolated. Each one of those variables is slightly changed and the results are compared. Every variable is first increase by 2% and then decrease by 2% subsequently. Their results are given in the next section. After knowing the relation between the change of variables and their effects on the results, some variables are selected in order to obtain an even more optimum design.

Results and Discussion

In this section, the results are presented and discussed in order to do another optimisation. The first part of the optimisation is the isolation of the most influencing parameters. As seen in figure 9.7, these variables are d3 (black) and d7 (magenta).
An additional optimisation procedure for these variables is done. Their results are illustrated in figure 9.7 9.8.

A maximum actuator force of ≈ 47 N and an actuator rod length of ≈ 0.13 m are used for the sizing of the actuator. These inputs are also used for sizing the rest of the mechanism. As the optimization model did not account for the frictional forces of the hinges, the actuator selected is able to apply more force. The internal links are also designed to withstand more loads than required. The weight of these components is of less importance since these components are very small and do not affect the overall weight significantly.

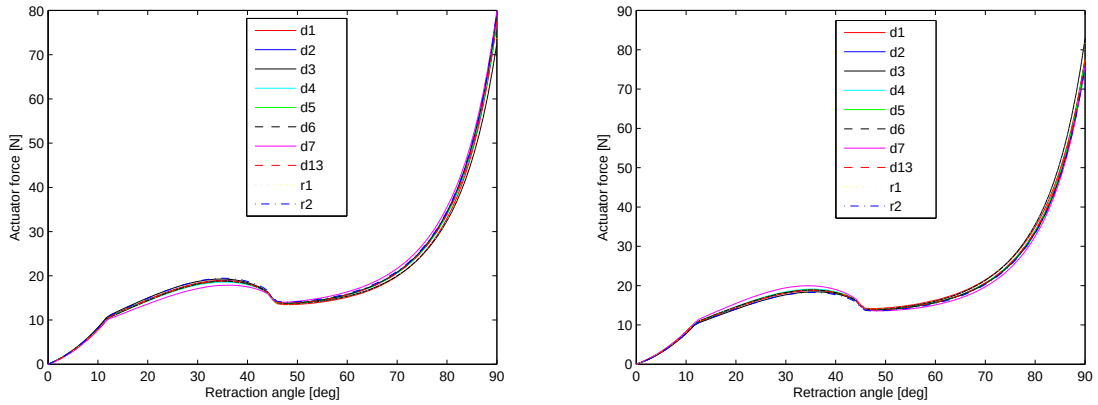

Figure 9.7: Graphs with several changed variables +2% (left) -2% (right).

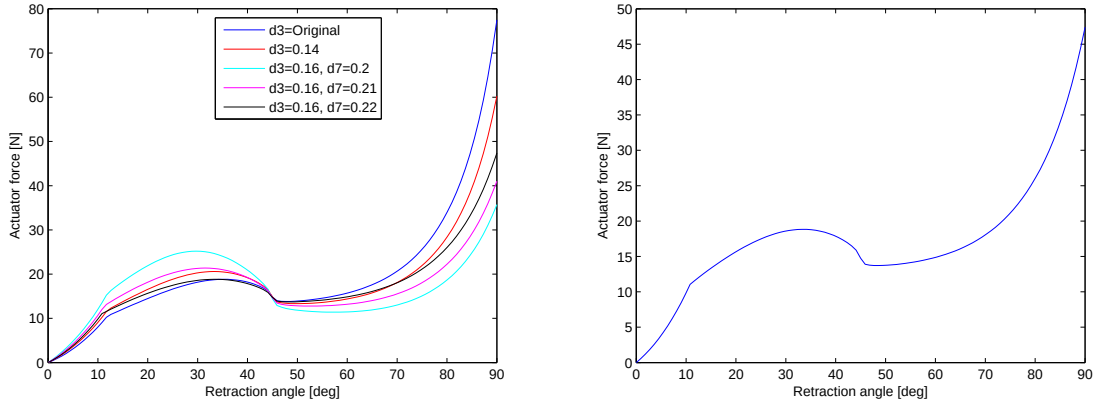

Figure 9.8: Graphs with several changes for d3 and d7 (left) final result of d3=0.155 and d7=0.19 (right).

9.7 Assembly

h The numbers computed in the above sections give an indication on the characteristic features of the landing gear. But all the components should be integrated together in the landing gear assembly. This section elaborates more on the choices made in the landing gear design. The nose wheel is connected to the oleo strut by a 'fork' connection. This connection is the most simple one since it does not introduce a bending loads into the strut. For the main landing gear, it is not possible to use a 'fork' connection since the large tyre underneath the oleo strut made the strut too long. When fully compressed, the struts would be longer than the minimum required ground clearance. The two different connections are displayed in figure 9.9. The actual sizing of the connections is left open for NPU for more detailed designs. The main landing gear struct is attached to the aircraft body by a simple pin joint to provide for rotational motion. The pin is connected to the front spar by adding reinforcements to the front spar. Since the longitudinal position of the spar is not equal to the longitudinal position of the pin joint, the landing gear load introduces a torque as well. To support these loads as much as possible, a proper connection between the front spar and the pin joint should be designed in the detailed design phase. The mechanism itself is attached to the front spar for two reasons. Attaching it to the front spar is simple and does not require any complex solution. The

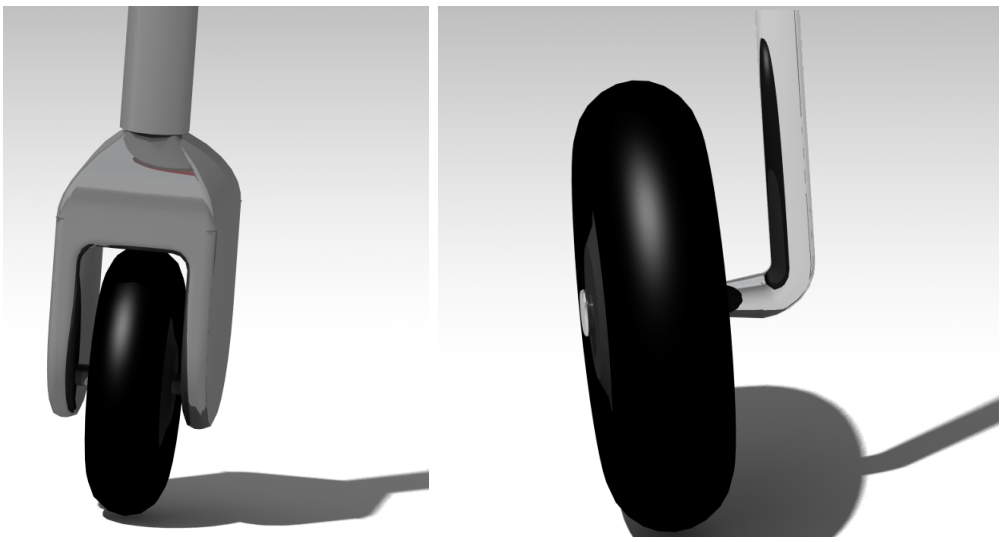

Figure 9.9: Wheel connection of the nose wheel(l) and main wheel(r) respectively.

second reason is that there should be space between the landing gear strut and the links that retract the wheel. In order to move the strut when the mechanism retracts, a pin connecting the mechanism and a ring around the oleo strut is designed, as displayed in figure 9.10

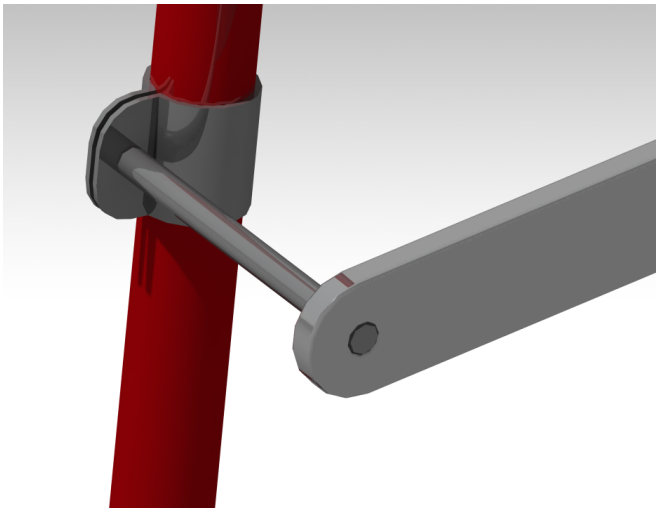

Figure 9.10: Connection between retraction mechanism and the landing gear.

The final assembly of all components is displayed in figure 9.11.

9.8 Weight and Cost

The calculations performed in the previous steps are carried out as an estimate of the first conceptual design. Numbers such as stroke length and tyre diameter can be later used for the detailed design. Given the short time span NPU has before the competition, it cannot be expected to develop all these components by itself. The weight and cost estimation is therefore based on an analysis of market products having similar properties to the ones computed in the sections above. The first components to discuss are the shock absorbers. Since it is not possible to develop an oleo strut in

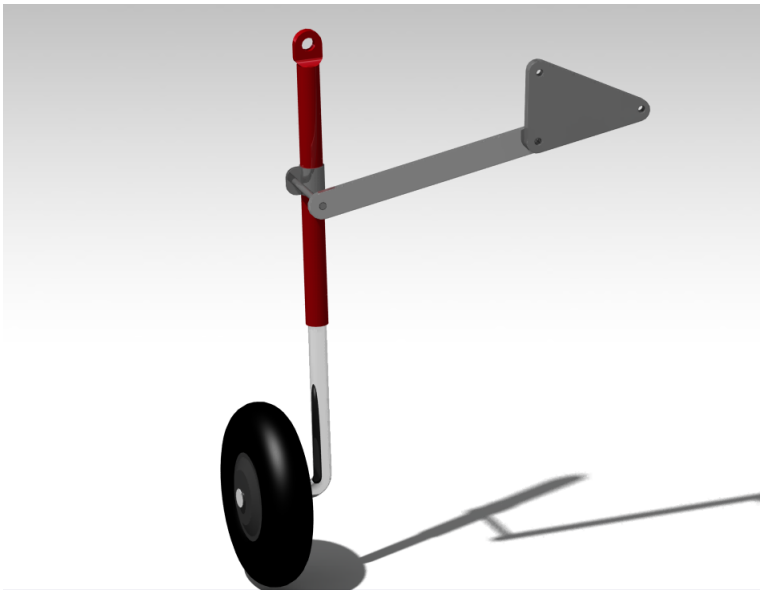

Figure 9.11: Total assembly of the right main landing gear.

such short time span, the oleo strut must be an already existing component. A thorough analysis on what is available on the market revealed that Robart[39] has the best oleo legs available. They provide oleo legs[40] for aircraft upto 55 lbs(25kg). These can take the loads during loading. It has a 16mm diameter cylinder and provide the option to adjust its length. However, the maximum length is slightly too short. Hence, some additional welding should be performed to make the strut long enough. The cost of these component are €61 each, which gives a total of €122 for the two main struts. For the strut in the front, a different leg is chosen since the loads on the front wheel are much smaller. Moreover, the wheel is smaller and the leg must provide for ground steering. Therefore, a steerable oleo strut is selected which can equip up to 4 inch tyres. The cost of this component is €139 and require some modification as well in order to make it long enough and operable by the servo. The next components are the tyres and brakes. From table 9.1, it is found that the ideal rear tyres size is 4.5 by 2.0 inch and the nose tyre is 1.9 by 0.9 inch. However, tyres in these exact sizes are not available. The compatibility of the braking system with the tyres should be taken into account too. For the tyres, two option are available; 4.5 by 1.25 inch tyres and a 5 by 1.56 inch tyres. The final choice made is the 5 inch tyres[41], since the 4.5 inch tyres have a relatively small width as compared to the values estimated. The wheels cost €61 each. For the nose wheel, a tyre of 2.0 by 0.8 inch is selected [42] which is quite close to the estimated size. It cost about €10 each. The total cost of all the tyres are €132. Since Robart did not provide any information about the weight of the oleo struts and the rear wheels, the weights in table 9.2 are estimated values. In order to make the entire braking system work, a lot of components are needed: brakes, pressure systems, controllable valves and fluid channels. Since it is a very complex process to match all these components, the chances of failure of the brakes are also quite high. Apart from the complexity of the system, it is also dependent on the tyres selected. These two reasons lead to the decision to buy a complete braking system[43] which are custom designed for the five inch tyres by Robart. Although this system is quite expensive at a cost of €203, its cost is comparable to selecting all the components separately. Since the braking system is part of the aircraft systems department, the cost and weight of this component is not included into the landing gear, but can be found Chapter 10. Although available off-the-shelf, some modifications have to be made to the components and links for the retraction mechanism have to be produced. The

links in the landing gear is estimated to have a weight of 103g. Since some of the material will be removed during machining, it is estimated that a total of 250g will be needed. At a price of €4.20/kg (estimated for the Formula Student competition), the cost are estimated to be €1 per mechanism, making it €3 for all wheels. The modification needed lengthen the struts and connect them to the body and wheels is estimated to be an additional 100g per strut, for which a total of 1kg aluminium is required.

Table 9.2: Weight and cost estimation of the landing gear

Component	Cost [€]	Weight [kg]
Main oleo strut (both sides)	122	0.9
Nose oleo strut	139	0.4
Main tyre (both sides)	122	0.3
Nose tyre	10	0.05
Mechanism links(all wheels)	3	0.3
Material for modifications	4	0.3
Total	**400**	**2.25**

From table 9.2, the total cost of the landing gear is approximately €400 and the weight is estimated to be 2.25kg.

9.9 Verification and Validation

It is important in any design process to verify and validate the results found through analysis. Although verification of the landing gear is difficult (there is only one method used), validation can be performed by comparing Tip-C to other already flying UAVs. The first design result to compare is the choice for the oleo strut and the required stroke length of 0.14m. The reference aircraft used for comparison are the Arcangel 1 and Penguin B 13, two conventional UAVs with a MTOW of 55 and 21.5 kg respectively. The first thing to notice is the fact that both aircraft use steel springs to get rid of its vertical velocity. Due to their high aspect ratio wings, their stall steed is lower, hence the vertical component of this velocity is lower as well. If possible, the steel spring is an excellent choice, due to its simplicity and lower cost. Another reason for the use of steel springs instead of oleo struts might be the smaller propeller diameter of these UAV. Since there is no risk of the propeller striking the ground, the use of steel springs allow for more compression during landing. The final reason could be the fact that some aircraft have non-retractable gears. This means that the total length of the struts is not an issue since they do not have to fit inside the body. If the legs have to fit inside the body, shorter legs are favoured, meaning that shock absorbers with short strokes lead to the shortest possible struts. The use of oleo struts is the best option for this UAV even though the reference aircraft have different solutions. The second parameter that can be checked visually are the sizes of the tyres. The sizes of the tyres can be estimated when analysing pictures, since other dimensions are known and tyres sizes can be derived from these references. The results are given in table 9.3.

From table 9.3 it can be seen that the tyres corresponds to the tyres selected for those two aircraft. The width of the tyre is slightly less, which has to do with the availability of the tyres on the market. Other parameters like the lateral and longitudinal positioning is more difficult to validate since information on these aspect are not widely available.

Table 9.3: Dimension of the main wheels of the Arcangel 1 and Penguin B respectively

Aircraft	Diameter [cm]	Width [cm]
Arcangel 1	17	5.5
Penguin B	10.5	5
Low AR UAV	12.7	4.0

9.10 Sensitivity analysis

The sensitivity analysis focuses on the influence of changing one of the design parameter and analysing its overall influences. To demonstrate this relation, the approach velocity of this aircraft (21 m/s) is lowered, while keeping the flight path angle at touchdown as it is. The first obvious effect is the reduction in the amount of kinetic energy to be dissipated during touchdown. This results in a lower stroke length for the shock absorber since smaller amount of work is required to reduce the vertical velocity of the aircraft. The smaller shock absorbers have a lower weight, which reduces the MTOW. This means that other components such as the wheel size and diameter of the struts can be reduced. Since the components selected are bought from the market rather than produced, the components itself remain the same. As there is a lack of alternatives in the market for the components, it can be concluded that a small change in any of the parameters does not affect the final design of the landing gear.

9.11 Recommendations

The landing gear components discussed in the above sections can be easily bought over the internet. However, they need to be modified to fit into the current UAV design. The oleo struts have to be made longer and must be attached with an eye on top to connect it to the front spar and a modification at the bottom has to be made such that the wheel is connected to it correctly. It was found on the website of 'Robart', the supplier of the components, that custom made components can be purchased as well. It might be an idea to contact them first to see what the cost is for the modification. If the cost is not too high, this option would be better than modifying the components since the company has a lot of experience in making such parts. It is also important to weigh all the components before fitting it into the aircraft since the weights of the oleo struts and wheels are estimated rather than actual data available from the manufacturer. The struts of the mechanism also have to be designed in more detail such that the mechanism is as light as possible. The position of the rotation points for the mechanism are designed, but the struts are not designed yet to minimise their weight. The same holds for the connection to the front spar and the connection of the wheels to the oleo struts. The final recommendation would be to investigate the opportunity to close the body after the landing gear is retracted. The most simple solution would be to place a doors of the landing gear onto the struts. When it is fully retracted, the door automatically seal the body without the need of additional mechanisms. However, this solution makes the aircraft more sensitive to cross-winds, so this option should be investigated in more detail.

10 Aircraft Systems

This chapter deals with the systems and components of Tip-C that facilitate its functioning and operation. Systems for this aircraft are broken into the electrical, mechanical and pneumatic systems. The aspects that are covered in the electrical system are the receiver, batteries, servos, electric motor speed controller (ESC) and the wiring. For the mechanical systems the mechanisms for the control surfaces are designed and sized. This is done in combination with the selection of the servos. Lastly the pneumatic systems for the landing gear retracts, brakes and belly flap are detailed. The complete aircraft systems architecture is shown in figure 10.1

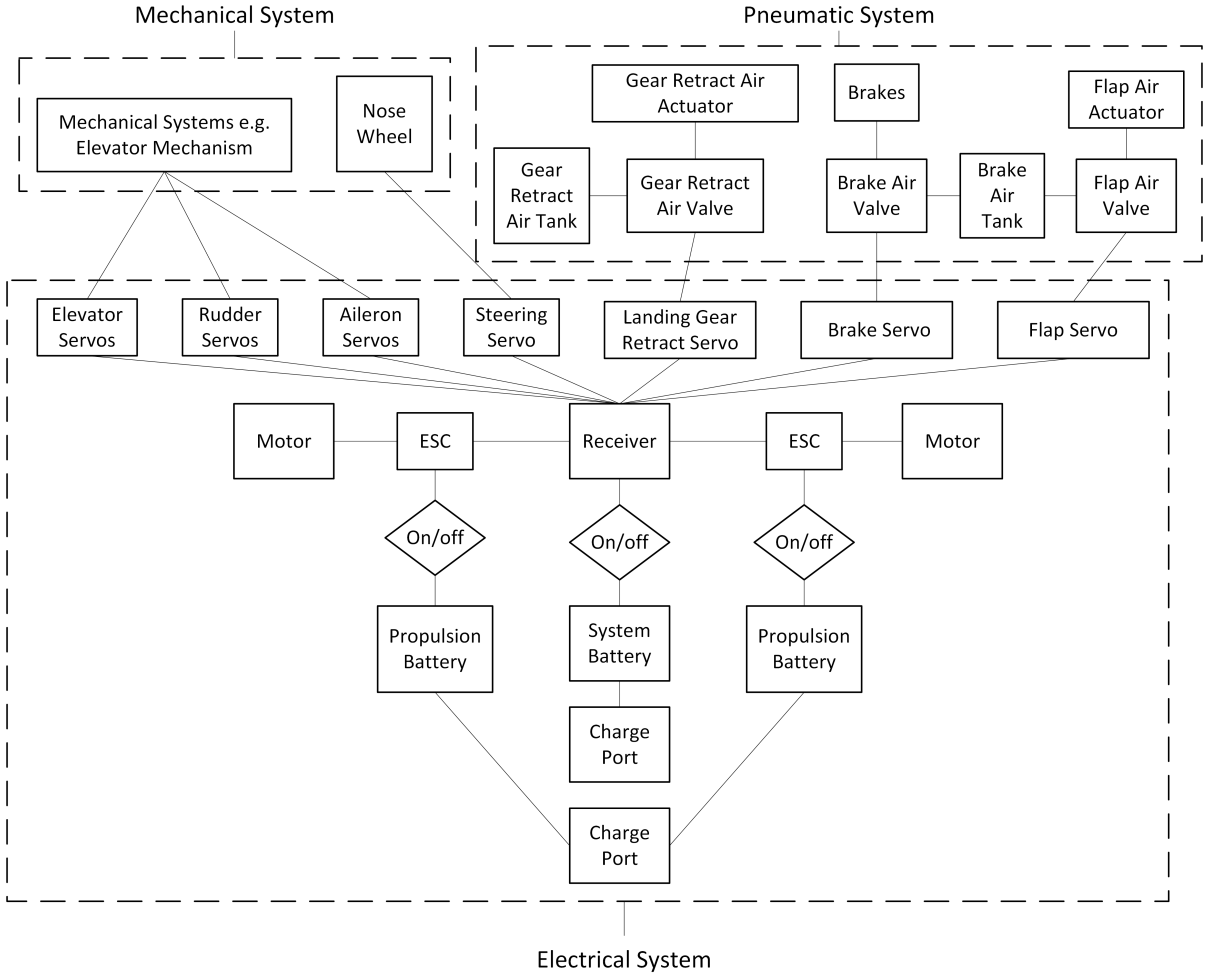

Figure 10.1: System Architecture of the UAV

10.1 Electrical Systems

10.1.1 Batteries

A logical point to begin is the source of the electrical power, namely the batteries. The aircraft uses two sets of batteries, one for the propulsion system and the other for the radio control gear, due to the different voltage requirements of the two. It also acts as a form of redundancy should the

propulsion battery become drained or fail.

The propulsion battery is a lithium polymer (LiPo) battery that provides enough energy to power the electric motors of the aircraft to meet the requirements. It is split into two packs for ease of locating them and to keep the wiring between battery and motor shorter due to the high current draw. Sizing of the batteries is done by considering the operating voltage of the motors, maximum current draw and total energy required. The motors operate on 36 V and have a maximum current of 90 A as given in Chapter 7. Total energy required is determined to be 642 Wh (Watt hours) in Chapter 8. Searching through battery suppliers and speaking to experts led to the Melasta battery company. They provide a wide selection of world class LiPo cells. Optimising the cell combination by selecting cells such that voltage, max current and total Wh are met while minimising the weight led to the selection of the LP7345150 model cell from Melasta [44]. These cells are arranged in two packs, each with ten cells in series and ten cells in parallel, providing a total of 666 Wh. The weight and cost per cell can be found in table 10.2.

The control system operates at 6 V as explained later in the servo subsection. No reliable data could be found on the current draw of the various radio gear components and thus the maximum current and total energy requirements can only be estimated from similar aircraft. A literature search on these aircraft resulted in a 6 V nickel metal hydride (Ni-MH) cell being selected with a capacity of 2300 mAh (13.8 Wh) [45]. Specifications of the cell can be found in table 10.2. This is a standard battery used for radio controlled models off this size and weight. It is advised that once the final control system setup is selected that the system is to be tested with this battery to verify that it performs as needed throughout the duration of a simulated flight.

10.1.2 Radio Receiver

Since it was chosen to control the UAV with radio waves from the pilot it needs a receiver to receive and interpret the commands sent from the transmitter. As can be seen in figure 10.1 the receiver has to have atleast 8 channels to operate all the various controls and mechanisms. It also has to operate at a distance of atleast 1 km in order to take all possible flight eventualities into account. These requirements resulted in the selection of the Futaba R6008HS receiver, as specified in table 10.2. This receiver met all requirements and operates on the 2.4 GHz type transmitters. A transmitter needs to be selected by the pilot that is compatible with this receiver. Installation of the receiver needs to be done as per the instructions of the manufacturer to prevent interference and ensure the receiver operates at the required range.

10.1.3 Servos

Choosing the servos depends on the torque they need to provide. The torque is calculated via the applied hinge moment of the control surface or moving object and the mechanism used to move it. This is done in the mechanical mechanisms section and the resulting torque, shown in table 10.1, is used here. It is found that the elevators and ailerons require a considerable torque from the servo and only a 6 V servo is suitable. This thus determines the voltage of the electrical control system. The choice of servo for each moving aircraft component is shown in table 10.2. It should be noted that the servo for the nose wheel is used for steering not retraction. The retraction of the nose gear is controlled by the main gear retract servo. During the selection it was assumed that the full 120° range of motion of the servo is used.

10.1.4 Propulsion

For the propulsion system the only component required, apart from the selected motor as given in Chapter 7, is the motor speed controller (ESC). This is chosen according to the motor type, operating voltage and maximum current draw. The chosen ESC is the Hacker MasterBasic Opto 90 as given in

table 10.2 and is also recommended by the motor manufacturer for the chosen motor. Cooling of the propulsion system is important and needs to be considered in the detailed design. The motor cooling inlets are located in the front of the motor on the side. These inlets need to be provided with cool air from outside. The outlet for warm air is at the rear of the motor and there needs to be an exit through the fuselage to allow this air out, promoting flow through the motor. The ESC also needs cooling air flowing over it and as such needs an inlet and exit duct for airflow. It is recommended that the ESC and motor share cooling ducts so as to minimise the impact on drag.

10.1.5 Miscellaneous Electrical Items

Other, smaller, items are needed to ensure the correct functioning of the electrical system. Two charging ports are needed to facilitate charging of the systems and propulsion batteries since they have different charging requirements. There needs to be an on/off switch between the receiver and systems battery to turn the system on and off. Two switches are also needed between the propulsion batteries and motor ESCs to isolate them. All the components need to be connected with appropriate wiring. Care must be taken with the wiring for the propulsion system due to the high current draw. Wire thickness should be at least as thick as that which is shipped with the ESC and motor and length must be minimised to limit power loss. All connections should be thoroughly checked and taped together as extra precaution to prevent them coming apart during flight. An airspeed sensor could be recommended to ensure the correct takeoff, cruise and approach speeds. These airspeed sensors are cheap, lightweight and simple to use, such as the MPXV7002DP from jDrones.

10.2 Mechanical Systems

In this section the design and sizing of the mechanical mechanisms to move the control surfaces is discussed. The deflection and hinge moments of the control surfaces are determined in the controllability Chapter 6, and used here to calculate the required linkage dimensions and servo torque. Figure 10.2 shows the design of the elevator, aileron and rudder control surface mechanisms. This same design is used for each of them due to its simplicity, reliability effectiveness and popularity with similar radio controlled model aircraft. Each mechanism has different dimensions depending on the required individual control surface deflections and resulting forces on the linkages. Dimensions of the mechanisms are given in table 10.1 with the variables representing those in figure 10.2. These dimensions were calculated by assuming stainless steel as the material (common for large RC aircraft such as this) with a compressive yield strength of 290 MPa and applying a factor of safely of 2.5 due to possibly inaccurate hinge moments, stress concentrations and gust loading on control surfaces. A similar material could be chosen such as aluminium alloy but due to the small dimensions, weight savings would be marginal so cost should be the driving factor. The required torque the servo needs to provide at maximum deflection is also shown in table 10.1. Clevis pins, as shown in figure 10.2, are commercially available and it is recommended that the steel versions are used so as to handle the loads such as those from Du-Bro [46].

Table 10.1: Control surface mechanism dimensions all in mm.

Control Surface	Servo Torque [kg.cm]	h_1	h_2	h_3	t_1	t_2
Elevator	12.18	4	8	58	1.6	4
Aileron	16.08	10	20	55	1.5	4.7
Rudder	1.68	5	10	43	1	1.6

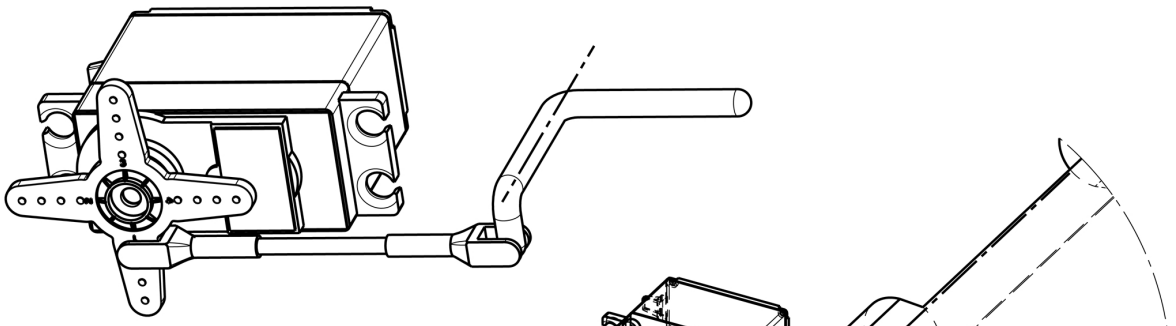

Isometric view
Scale: 1:1

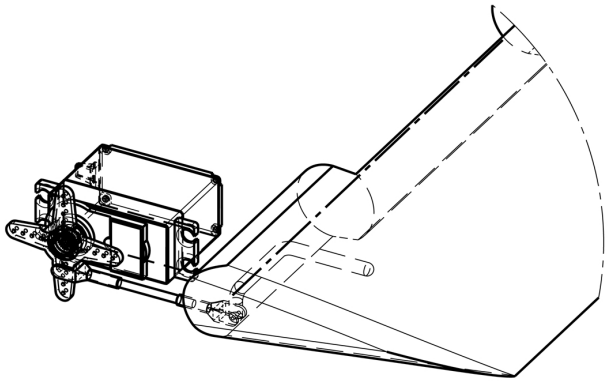

Detail with surface
Scale: 1:2

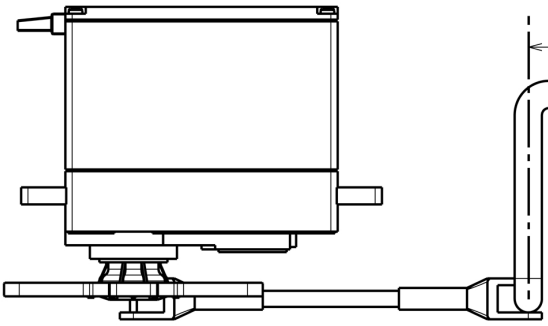

Top view
Scale: 1:1

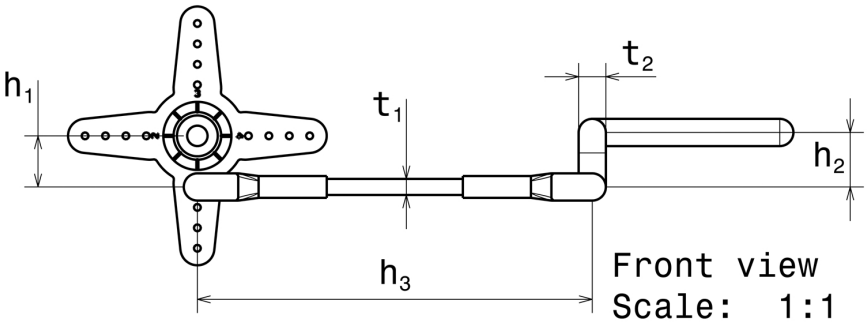

Front view
Scale: 1:1

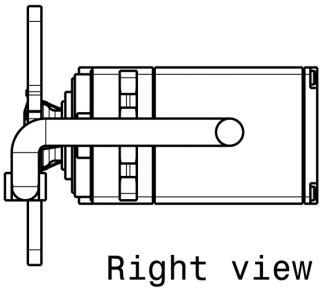

Right view
Scale: 1:1

This drawing is our property.
It can't be reproduced
or communicated without
our written agreement.

DASSAULT SYSTEMES

TipC: Aircraft Systems

DRAWN BY	DATE	SIZE	DRAWING NUMBER		
M.T.H Brown	2013/06/25				
CHECKED BY	DATE	A4	Elevator Mechanism		
M. Schmeetz	2013/06/26				
DESIGNED BY	DATE	SCALE 1:1			SHEET 1/1
DSE Group 17	2013/06/25				

Figure 10.2: Detailed drawings of the mechanical control surface mechanism

10.3 Pneumatic System

A pneumatic system is used to retract the landing gear and to activate the brakes. It will also be used to operate the belly flap. The brakes have to be pneumatic for this aircraft size and due to the long extension requirement of the landing gear mechanism only a pneumatic actuator is feasible. This is common in radio controlled model aircraft, especially in this size class. The pneumatic system is split into 2 separate systems, one for the landing gear and the other for the brakes and belly flap. This is done for redundancy, to maintain high pressure for the brakes to have adequate braking and due to the fact that the brakes come as a complete system as described later. The layou of the two systems can be seen in figures 10.3 and 10.4

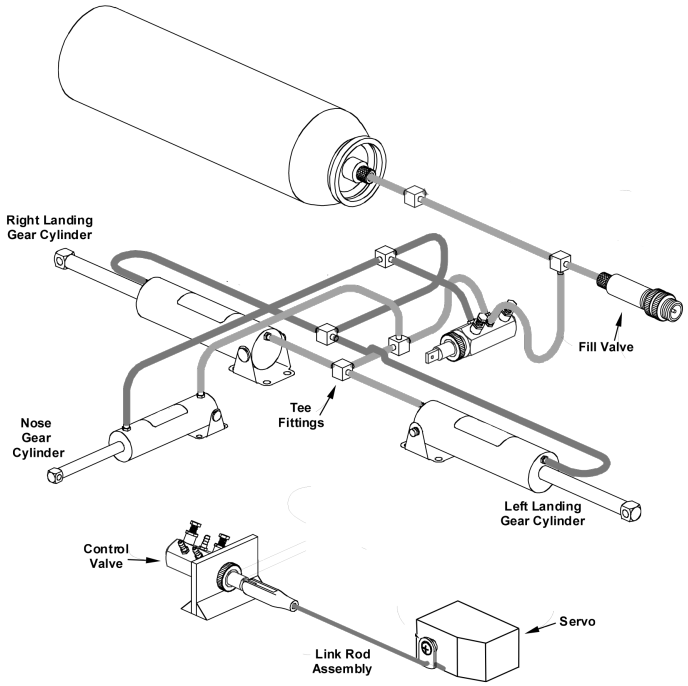

Figure 10.3: Layout of the landing gear retract pneumatic system

Sizing of the landing gear actuator is done considering the amount of extension and force required by the retract mechanism as found in Chapter 9, resulting in the actuator shown in table 10.2. It must be noted that each landing gear has a separate mechanism and thus its own actuator. The landing gear retract system has been designed to operate at 690 kPa air pressure. The air tank for the gear retract is sized such that it can facilitate at least 3 complete cycles (retract and deploy) on one charge of air. 3 cycles was chosen to allow for takeoff, one flight display with the gear down, landing and a go-around or balked landing. The system can then be recharged using a compressor or bicycle pump via the air fill valve. The speed of the retraction and deployment of the landing gear can be adjusted on the retract valve to prevent the gear moving too quickly and damaging the mechanism.

The braking system set comes complete with an air tank, proportional electronic valve, brake actuator and discs, air fill valve and connectors. The complete set is chosen since it is cheaper than buying the various components separately. The proportional electronic valve allows proportional braking to minimise the landing distance and help avoid skidding. Unfortunately the weight of the braking system could not be determined because the manufacturer would not provide the information. Thus the brake system must be weighed before it is installed in the aircraft to check and maintain the

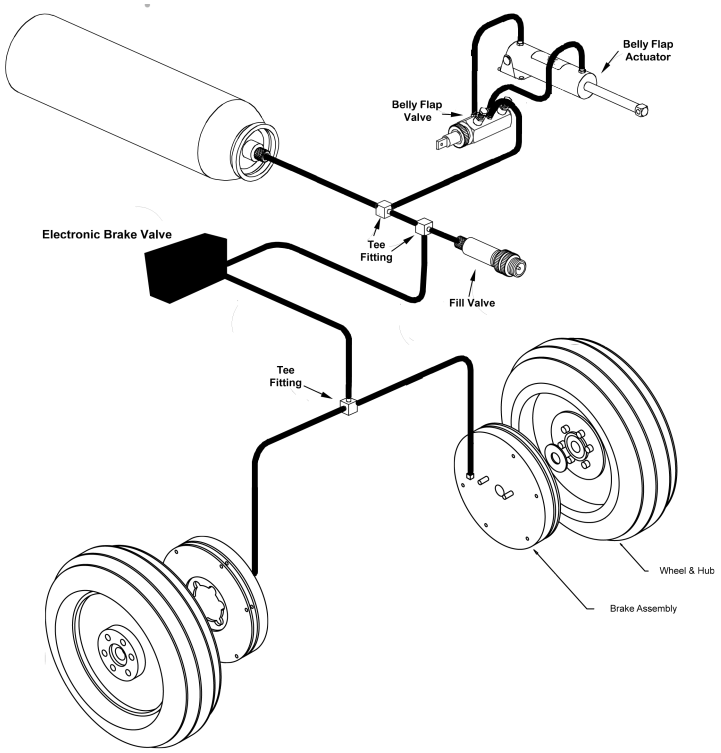

Figure 10.4: Layout of the brake pneumatic system

MTOW and c.g.

Regarding the belly flap very little reliable information could be found on the hinge moments exerted by belly flaps. Thus, since it is deflected to 90° and is designed to create as much drag as possible, being perforated, it was assumed that the full dynamic pressure would be acting on the flap. This could result in an over design of the mechanism thus testing should be done in order to verify the assumption. These assumptions at the maximum flap deployment speed of $20m/s$ resulted in a hinge moment of $1.2Nm$. This moment, along with the 90° deflection could not be met by an electrical servo and mechanism. Thus only a pneumatic actuator is suitable. A simple mechanism with a suitable moment arm is designed. The chosen pneumatic actuator is the Sierra Giant Scale AC-43750 which is shown in table 10.2 and will be attached to the braking air system with its own valve and servo.

10.4 Recommendations

As mentioned throughout the section there are various activities that need to be carried out during the detailed design before the aircraft can be put into production. These activities are:

- Check the capacity of the systems battery
- Select a suitable radio transmitter that is compatible with the receiver
- Once the final control surface hinge moments are known the mechanism sizing and servo selection needs to be checked
- If the motor specification changes the chosen ESC needs to be verified

- The brake system needs to be weighed so as to determine its weight for MTOW and c.g. calculations
- Hinge moments for the belly flap need to be verified and then the mechanism and chosen pneumatic actuator need to be checked that they meet the required force and stress limits.

Table 10.2: Parts list of the aircraft systems with weight and cost per unit

Group	Component	Make and Model	Weight [g]	Cost [€]	Quantity
Electrical System					
Batteries	Systems Battery	HobbyKing 9169000008	148	5.73	1
	Propulsion Cells	Melasta LP7345150	110	20.56	40
Radio Gear	Receiver	Futaba R6008HS	13.5	99.40	1
	Elevator Servo	Futaba S9155	61	90.98	2
	Aileron Servo	Futaba S9352HV	72	114.50	2
	Rudder Servo	Futaba S3156	9.3	30.59	2
	Belly Flap Servo	Futaba S3154	7.9	26.76	1
	Gear Retract Servo	Futaba S3154	7.9	26.76	1
	Brake Valve Servo	Futaba S3154	7.9	26.76	1
	Nose Wheel Servo	Futaba S9155	61	90.98	1
Propulsion	Motor ESC	Hacker MasterBasic 90	112	190.00	2
Mechnical System					
Control Surface Mech.	Elevator	Custom	9	4	2
	Aileron	Custom	12	4	2
	Rudder	Custom	4	4	2
Pneumatic System					
Gear System	Actuator	Sierra Giant AC-437500	85	42.05	3
	Air tank	Hobby King 300CC	45	3.17	1
	Valve	Robart 167VR	15	25.19	1
Brake System	Complete Set	Robart 139SET	n/a	204.11	1
Belly Flap System	Actuator	Sierra Giant AC-437200	34	29.05	1
	Valve	Robart 167VR	15	25.19	1
Total			**6149**	**2357.20**	

11 Structure

In this chapter, the structure of the UAV is discussed. A low AR aircraft has a simpler and lighter structure compared to the conventional aircraft because the loadings are lower on the root. Since the fuselage and wings are integrated to one simple shape, the configuration helps for saving structural weight and increasing structural efficiency. A hybrid structure is chosen because of its advantages for the chosen design. This chapter discusses several aspects for the final structure design. The load cases are first discussed where the worst case is determined. Since the structure design is an iterative process, optimisation is done throughout the whole design process. Next, the materials used are discussed. Cambridge Engineering Selector (CES) is used to find and study material choices. After the material is chosen, a full iteration of the whole design is done. This results in final changes in the structure. These changes are based on analysis and changes of other parameters from other disciplines (for example, changes in the size of the landing gear can result in a different structure).

11.1 Load Cases

11.1.1 Manoeuvres & Gusts

For both the first and second load case a velocity versus load diagram, V,n-diagram, is used to represent the loads as a function of flight velocity. The Federal Aviation Regulations part 23 [47] (FAR-23) is used for both diagrams. The first load case to be handled is manoeuvres. In order to construct the diagram the maximum and minimum load factors are found to be 3.80 and -1.52 respectively [48]. Next, the relevant velocities needed are found and listed in table 11.1. The stall speed and the cruise speed are defined in Chapter 8 while the rough-air speed and dive speed are calculated in 11.1 and 11.2. Finally, the $C_{N_{max}}$ curve is determined by using equation 11.3. The V,n-diagram for manoeuvres can be seen in figure 11.1.

$$V_B = V_S \cdot \sqrt{\frac{K_g \cdot U \cdot V_C \cdot C_{L_\alpha}}{\frac{2}{\rho} \cdot m \cdot g}} \tag{11.1}$$

$$V_D = 1.25 \cdot V_C \tag{11.2}$$

$$C_{N_{max}} = 1.1 \cdot C_{L_{max}} \tag{11.3}$$

Table 11.1: Flight-phase and gust velocities.

Flight-phase	[m/s]	Gust	[m/s]
Stall, V_S	19.00	-	-
Cruise, V_C	37.93	Cruise, U_C	20.12
Dive, V_D	47.04	Dive, U_D	15.24
Rough-air, V_B	29.30	Rough-air, U_B	7.62

The second load case looked at is gusts. During flight the UAV experiences gusts of varying magnitude and these introduce peak loads to the structure. The V,n-diagram for gusts mostly uses the same input as the diagram for manoeuvres. The minimum and maximum load factor remain unchanged, the velocities remain identical and the same curve for $C_{N_{max}}$ is used. The difference lies in the use of the gust speeds expected during flight and these are shown in table 11.1 [48]. The shape of

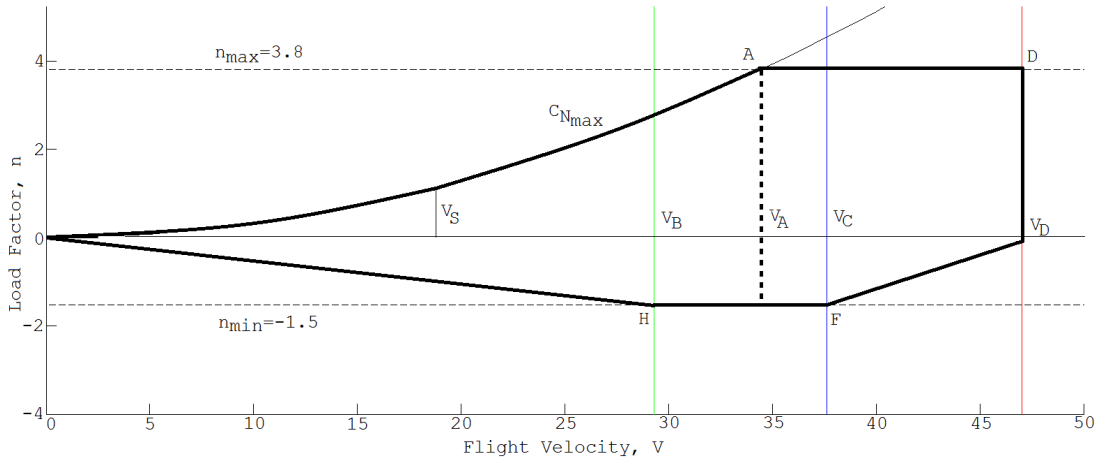

Figure 11.1: V-n diagram for manoeuvres.

the V,n-diagram is mostly determined by the intersection of the flight speeds with the corresponding gust speeds. The V,n-diagram for gusts is shown in figure 11.2. Note that from both graphs it can be seen that the minimum flight speed at n_{max}, V_A, is equal to 34 m/s.

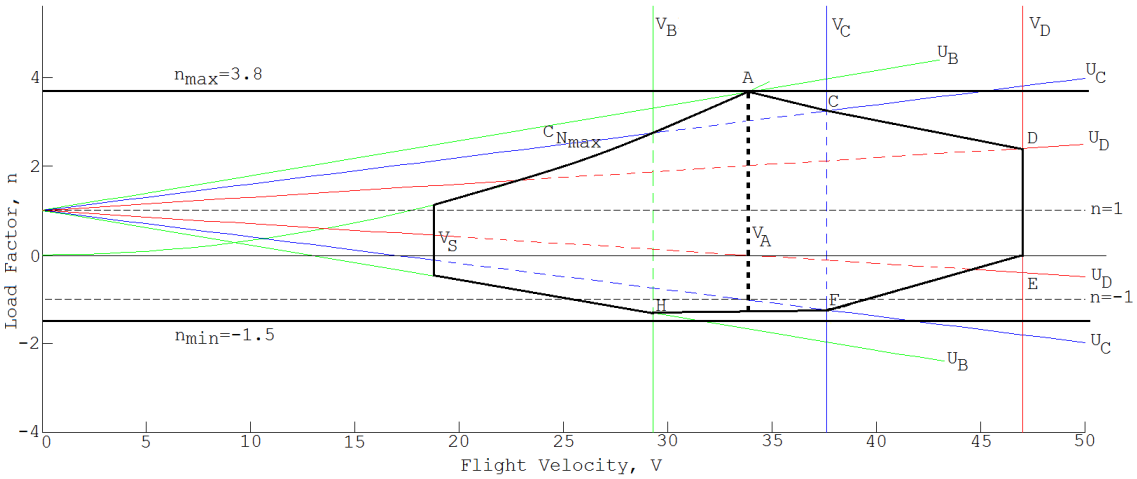

Figure 11.2: V-n diagram for manoeuvres.

11.1.2 Landing

During landing of the aircraft, high loads are introduced into the structure. Also the loading during landing is significantly high. The loading due to the landing is already discussed in Chapter 9. The value of the loading factor during touchdown is 3.

11.1.3 Taxiing

The last discussed load case is taxiing. The unique feature of this case is that it has no lift force. All the forces are pointed downward and only the gravity is acting on the aircraft. For this case, only the weight of the whole aircraft is taken into account.

11.2 Structure Layout

In this section, the structure layout is discussed. The layout is determined by using numerical analysis which is discussed in section 11.4. Since the design does not contain many moving parts and the wing span is small, the structure is designed to be simple and lightweight compared to higher AR aircraft.

After referring to literature and discussing with experts, the final structure design is decided on. The body is made out of a main structure consisting of two main spars and four ribs. They support the whole structure and are the main load carriers. The spars are designed to withstand bending around the longitudinal axis while the ribs prevent the aircraft from bending around the lateral axis. The space between is filled with foam to withstand the shear loads. Cutouts are made in the foam for placement of mechanisms, payload and batteries and a hatch is used to close the cutout. A skin layer is applied on the foam for aerodynamic properties. The skin is reinforced by the foam below which makes buckling difficult to occur. The foam is easily manufacturable which makes the integration of mechanisms possible.

11.3 Material Choice

During the design of the structure, different possible materials are also investigated. The materials considered include different types of metals, wood and composites. Comparison is done between these materials with regards to strength, stiffness, fracture toughness, crack propagation, resistance, density, impact resistance, corrosion, manufacturing approach and cost. The preferences of NPU, who are going to produce the UAV, are also very important deciding factors. Based on these factors, the materials are chosen.

Based on the preference of NPU and advantages of material characteristics, the final material chosen for the structure is spruce. Foam is used between the structure for shear loads. The foam type used is "ROHACELL 51 IG/IG-F" because of its high specific material properties. Both materials can be found in table 11.2.

Table 11.2: Material Characteristics

Material	ρ [kg/m^3]	σ_c [MPa]	σ_t [MPa]	τ [MPa]	E [MPa]	G [MPa]
Spruce	520	45.2	76.2	9.3	13,400	990
ROHACELL	52	0.9	1.9	0.8	70	19

As can be concluded, there is not only one material used everywhere on the structure. The preferences of NPU has a big influence on the material choice which does not mean that the most logical material is chosen.

11.4 Analysis

After the basic strucutre is chosen, analysis on this structure is done. The analysis is done for the front view and the side view. The design of the spars and ribs are discussed in this section and after that the C-wing is discussed.

11.4.1 Loadings

Figure 11.3 shows all forces from the front view and the side view. With all forces visualised in the free body diagram, numerical calculations are done to obtain the moment and shear force diagrams. Numerical analysis is then done to determine the M_x and V_z loadings.

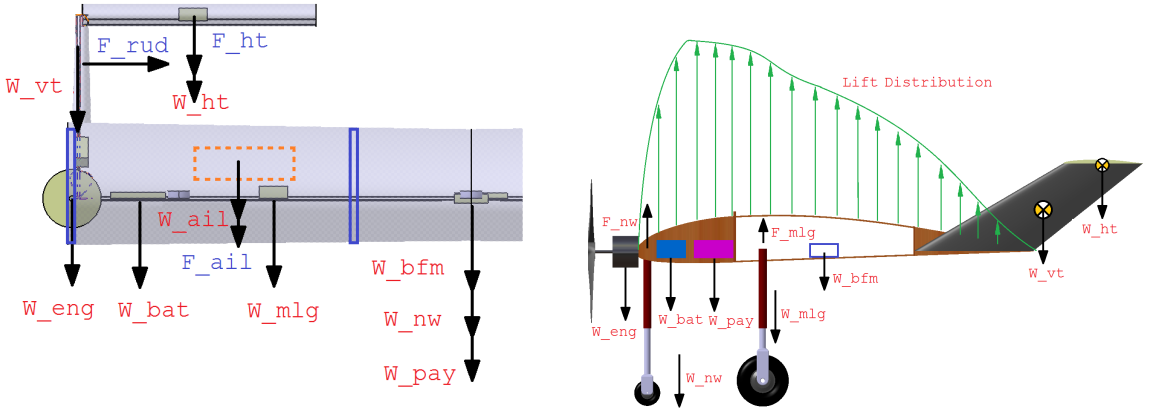

Figure 11.3: Free body diagram of half aircraft frontview (left) and sideview during landing (right) - force and weight definitions can be found in the nomenclature

Front View

In this subsection, the analysis used for the front view are discussed. First the method is explained and second the results are given and discussed.

Numerical Analysis of Internal Shear Force and Moment

In order to determine the Moment and Shear loadings, the aircraft is assumed to be symmetric (from the front view) and assumed to be able to be analysed like a beam. Since the aircraft is assumed to be symmetric, only one side of the aircraft is analysed. The data for the other side is easily subtracted from the calculated first side. Using the numerical method, the beam is cut in sections. Figure 11.4 shows a visualisation of how to analyse the beam. A cut is made at an arbitrary point to determine the reaction moment and force. The wing is cut in a large amount of sections (e.g. 200) and the moments and forces at every section are calculated.

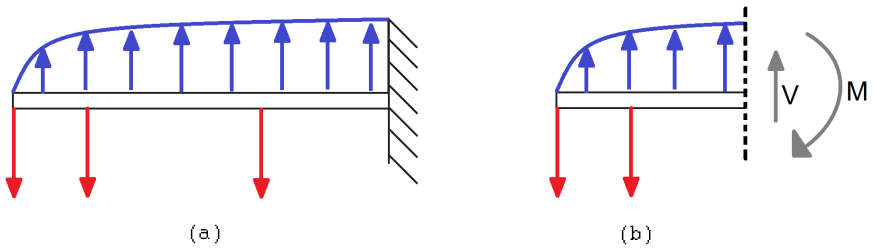

Figure 11.4: General beam analysis with a complete beam (a) and a beam which is cut (b)

In figure 11.5, an example is given to visualise the method of using numerical analysis. The total moment is made up of the distributed lift over the wing and the component weights shown in equation 11.4. The lift component of each segment (L_i) and is multiplied with the distance to the cut (y_i).

$$M_{total} = M_{x_{lift}} + M_{x_{comp}} = \sum_{i=1}^{n} L_i \cdot y_i - \sum_{i=1}^{n} w_i \cdot y_i \tag{11.4}$$

Where:

$$L_i = c_l \cdot \frac{1}{2} \cdot \rho \cdot V^2 \cdot MAC \cdot i_{width} \tag{11.5}$$

$$i_{width} = \frac{1}{2} \cdot \frac{b}{n} \tag{11.6}$$

The lift coefficient c_l is determined from aerodynamic properties while n represents the number of segments the beam is cut into. In order to simplify the analysis, the surface of a segment used in equation 11.5 is taken to be the width of the segment multiplied by MAC.

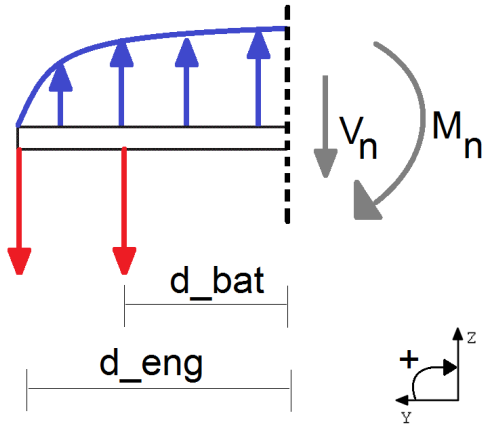

Figure 11.5: A cut beam for analysis

The same method is used to analyse the shear force along the span of the wing. Again, the total shear force is made up of the lift distribution and the component weights. Equation 11.7 is used to determine the shear force.

$$V_{z_{total}} = V_{z_{lift}} - V_{z_{comp}} = \sum_{i=1}^{n} L_i - \sum_{i=1}^{n} w_i \tag{11.7}$$

Where L_i is given by equation 11.5. The calculations can be improved since the chord of the aircraft has a negative taper. But since the differences are negligible, the calculations are kept simple.

The results of the numerical analysis are discussed in this subsection. The moment diagram is shown in figure 11.6, which shows that the largest moment created by the lift and components is negative. Due to the sign convention (given in figure 11.5), the components are creating a bigger moment than the distributed lift force. The absolute value obtained from the calculations is: $M_x = 41Nm$. This value is relatively small with respect to the moment created by the landing gear during landing (see Chapter 9). The shear forces acting on the wings are visualised in a graph which can be found in figure 11.5. As can be concluded from the graph, the maximum shear force can be found at a location of 0.4m from the center. The landing gear is positioned at this location. The maximum (absolute) shear force value along the span is: $V_z = 107.2N$. Because of symmetry, this value can b found on both sides of the aircraft.

The values found so far are during flight. During touchdown, the loads are much higher with a load factor of 3 (as mentioned in Chapter 9). The new moment and shear loads are shown in figure 11.7. The maximum values are $M_x = 261Nm$ and $V_z = 602N$.

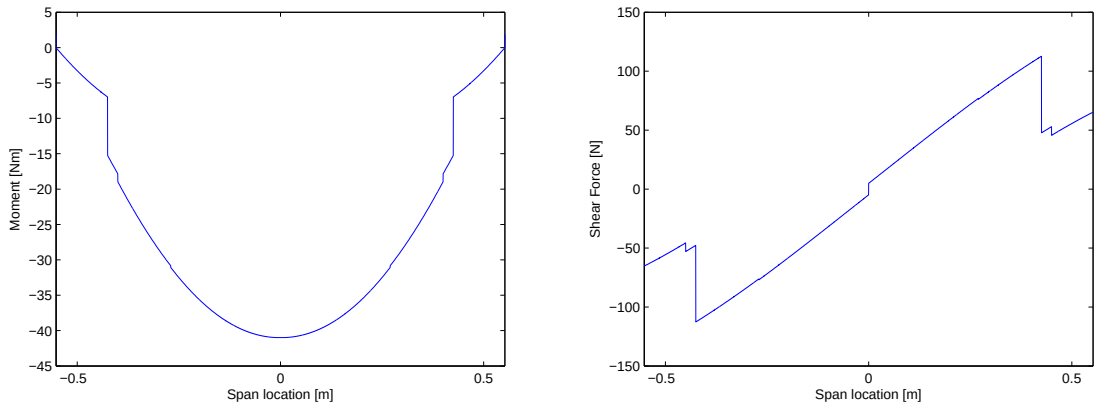

Figure 11.6: Graph of the moments (left) and the shear forces (right) acting on every location of the beam (200 measuring points)

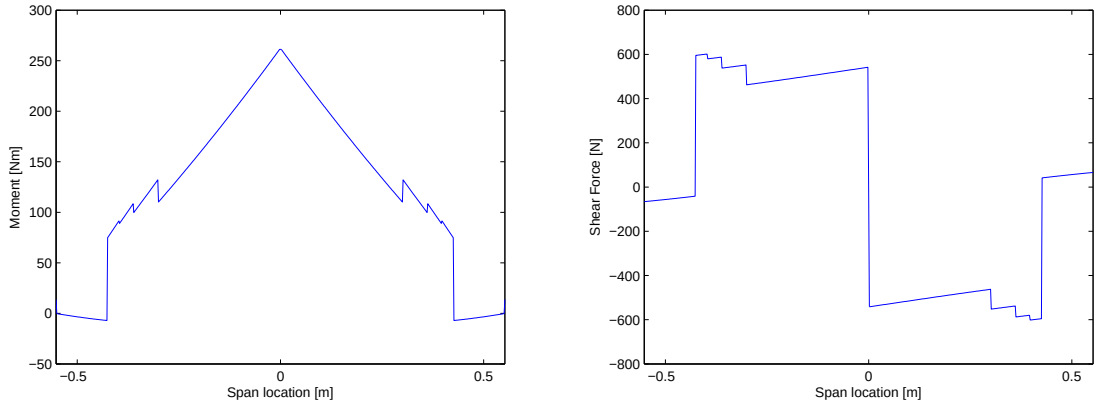

Figure 11.7: Graph of the moments (left) and the shear forces (right) during touchdown

Side View

For the side view, analysis are also done but in a different way. No internal moments and forces are determined explicitly but a FEM analysis is done. Figure 11.3 is used to do the analysis.

11.4.2 Spars

In this subsection, the sizing of the spars is discussed. First the spar design is explained in detail and then the more technical aspect of the spars is discussed.

Design of Spars

As it is explained in section 11.2, 2 spars can be used to prevent bending around x axis. Because the resultant lift force acts at the a.c. at quarter-chord of the airfoil, one spar must be located there. Another spar is placed at the C-wing connection to the body due to the larger moment in this area. The spar heights are defined based on the airfoil thickness at the spar locations (see figure 11.8). Spars must also be able to carry the internal shear forces calculated in section 11.4.1. And since it is assumed that the skin does not carry any load, the spars alone must withstand the torsion. By

looking at normal stresses in the spars due to bending, the number and size of spars are designed. After that, the shear stresses due to internal shear forces are checked for failure. Last but not least, the shear stresses due to torsion are checked. In case of failure, the thickness are increased.

To simplify the shape of the body for calculations it is assumed that the curved leading edge is a straight line. Since the curved shape increases stiffness of body geometrically, this assumption is valid (results in over designing). Because the airfoil's chord increases from center to the tip of the body, the front spar is placed at the distance of average aerodynamic center of airfoil at the centre and the tip from the leading edge.

Normal stress

Normal stress due to the moment can be calculated by equation 11.8[49],

$$\sigma_y = \frac{M_x \cdot z}{I_x} \tag{11.8}$$

where M_x is the moment around x direction, z is the maximum distance from the centroid and I_x is the area moment of inertia. As it is explained in section 11.4.1, the maximum moment occurs at the centre of body due to the impact force during landing on one of the main landing gear. Applying a safety factor of 1.5, this moment equals to 401 Nm.

To design the spars, equation 11.8 can be rewritten and solved for the second moment of inertia (see equation 11.9),

$$I_{x_{req}} = \frac{M_x z}{\sigma_{ult}} \tag{11.9}$$

where $I_{x_{req}}$ is the required area moment of inertia, and σ_{ult} is the ultimate strength of the selected material for the spar. After calculating $I_{x_{req}}$, the sizes of the spars can be determined.

Cross-section Equation 11.8 shows that a larger area moment of inertia (I_x) results in a smaller normal stress. I-beams are most desirable for bending resistance as they have large area moments of inertia with low weight. However, due to the increase in thickness of the body from root to tip, the production of the I-beam becomes harder. After some discussion with NPU, a solid rectangular cross-section is selected based on NPU's preferences.

Centroid Since the thickness of the spars are not designed yet, it is assumed that the centroid is in the middle of the airfoil (in vertical direction). The exact position of the centroid can be calculated by iteration after sizing the spar thickness by using equation 11.10[49]

$$\bar{z} = \frac{A_{s_1}\tilde{z}_{s_1} + A_{s_2}\tilde{z}_{s_2}}{A_{s_1} + A_{s_2}} \tag{11.10}$$

where A is the area of each spar and $\tilde{z}$ is the centroid of each spar from the reference point (see figure 11.8)[49]

Area moment of inertia Total moment of inertia can be calculated by equation 11.11

$$I_{tot} = I_{s_1} + A_{s_1} d_{s_1}^2 + I_{s_2} + A_{s_2} d_{s_2}^2 \tag{11.11}$$

where I_s and A_s are the area moment of inertia and area of each spar respectively. d_s is the distance between the centroid of each spar to the centroid of airfoil. I_s and A_s can be calculated by equations 11.12 and 11.13[49]

$$I_s = \frac{1}{12} b_s h_s^3 \tag{11.12}$$

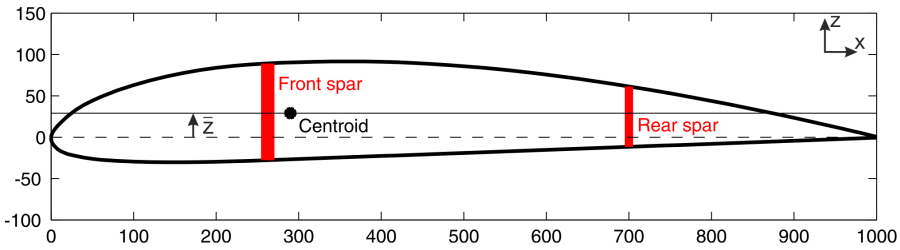

Figure 11.8: Location of cog

$$A_s = b_s h_s \tag{11.13}$$

where b_s is the thickness of the spar and h_s is the height of the spar (see figure 11.9). To be able to solve for thickness of each spars, it is assumed that the thickness of spars have the same ratio as their height (see equation 11.14).

$$\frac{b_{s_1}}{b_{s_2}} = \frac{h_{s_1}}{h_{s_2}} \tag{11.14}$$

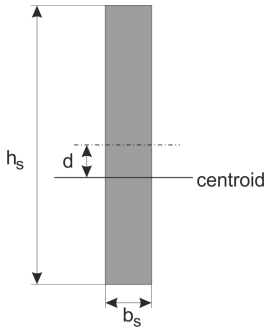

Figure 11.9: Spar sizes

Results As it is explained in section 11.2, spruce wood is selected for structure of the body. Since the compression strength ($\sigma_c = 45.2MPa$ [50]) of spruce is smaller than its tensile strength ($\sigma_t = 76.2MPa$ [50]), the compression strength is used as the ultimate strength in equation 11.9. As explained before moment is 401 Nm, and z is the half of the height of the front spar in the beginning. Since height of the spars are defined based on the airfoil thickness at the position of the spars the only unknown in equation 11.11 is the thickness of the spars. The results of the calculations are shown in table 11.3

Table 11.3: Spars positions and sizes

$I_{x_{req}}$ $[mm^4]$	$\bar{z}_{initial}$ $[mm]$	x_{s_1} $[mm]$	x_{s_2} $[mm]$	h_{s_1} $[mm]$	h_{s_2} $[mm]$	b_{s_1} $[mm]$	b_{s_2} $[mm]$	$\bar{z}_{final}$ $[mm]$
5.578×10^5	30.69	262.5	700	116.9	73	3.61	2.25	29.03

In table 11.3 x_s is measured from the leading edge of the airfoil. By comparing the initial centroid ($\bar{z}_{initial}$) and final centroid ($\bar{z}_{final}$) it can be seen that it is shifted about 5% which could be neglected.

Shear stress due to internal shear forces

The shear stress due to the internal shear forces is calculated by equation 11.15 [35]. In this way, by using the sizes of the spar calculated in the section "Normal Stress", the shear stress in each spar is calculated. If the shear stress is larger than the shear strength of spruce the thickness of the spars must be increased.

$$\tau_{yz} = \frac{q_{yz}}{t} \tag{11.15}$$

where q is the shear flow and t is the thickness of the spar (in here b_s). Shear flow is defined by equation 11.16[35],

$$q_{yz} = -\frac{I_{xx}S_x - I_{xz}S_z}{I_{xx}I_{zz} - I_{xz}^2}\int_0^s \mathrm{tx}\,\mathrm{d}s - \frac{I_{zz}S_z - I_{xz}S_x}{I_{xx}I_{zz} - I_{xz}^2}\int_0^s \mathrm{tz}\,\mathrm{d}s \tag{11.16}$$

where I_{xx} and I_{zz} are the area moment of inertia around x axis and z axis, respectively. I_{xz} is assumed to be zero by assuming that combination of two spars in the airfoil is symmetric around x axis. $S_z = 875.53N$ is the resultant forces in the z direction. Lift during touchdown $L_{touchdown} = 72.93N$, MTOW $W = 209.54N$ and impact force of main landing gear $F_im = 629N$ are shown in figure 11.10 . To study the worst case scenario it is assumed that there is gust during landing, therefore, lift is multiplied by gust load factor of 3.8. In addition safety factor of 1.5 is used for the other loads. S_x is neglected compared to the loads in z direction. t is the thickness of each spar (in here b_s). Simplifying equation 11.16 results in equation 11.17 for each spar,

$$q_{yz} = -\frac{S_x b_s}{I_{xx}}\int_0^s \mathrm{x}\,\mathrm{d}s \tag{11.17}$$

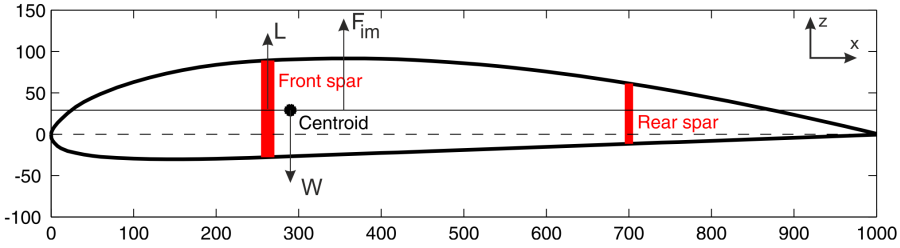

Figure 11.10: Loads and locations on the body from side view

In equation 11.17, x defined as $-\frac{h_s}{2} + s$. By substituting x and solving the integral equation 11.18,

$$q_{yz} = -\frac{S_z b_s}{I_{xx}}(-\frac{h_s s}{2} + \frac{1}{2}s^2) \tag{11.18}$$

As figure 11.11 shows maximum shear flow occurs in the middle of the spar, therefore, by solving the integral for the boundary of 0 to $\frac{h_s}{2}$ maximum shear flow can be derived which is shown in equation 11.19,

$$q_{yz_{max}} = \frac{S_z b_s}{I_{xx}}(\frac{1}{8}h_s^2) \tag{11.19}$$

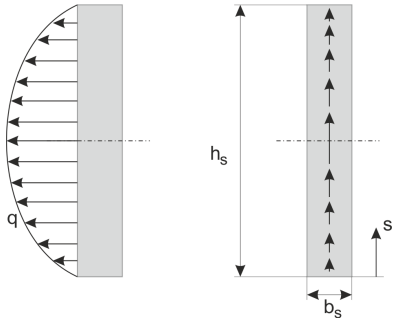

Figure 11.11: Shear flow distribution in each spar

Table 11.4: Maximum shear flow and shear stresses in spars

$q_{yz_{max_{s_1}}}[\frac{N}{mm}]$	$q_{yz_{max_{s_2}}}[\frac{N}{mm}]$	$\tau_{yz_{max_{s_1}}}[\frac{N}{mm^2}]$	$\tau_{yz_{max_{s_2}}}[\frac{N}{mm^2}]$
10.09	2.46	2.79	1.09

Results By substituting the required area moment of inertia ($I_{xx} = 5.578 \times 10^5$) and thickness of spars ($b_{s_1} = 3.61mm$ and $b_{s_2} = 2.25mm$) calculated in the section "Normal Stress" and h_s in equation 11.19 shear flow is calculated. Then by substituting these values in equation 11.15, maximum shear stress is calculated. The results are shown in table 11.4.

By comparing the maximum shear stresses shown in table 11.4 by the shear strength of spruce ($\tau_{spruce} = 9.3MPa$), it can be seen that there is no failure due to the internal shear forces.

Shear stress due to torsion

As it is explained before, the torsion is carried only by the spars. In order to calculate the shear stress in each spar by using equation 11.20[35], the torque on each spars must be calculated first.

$$\tau_{yz} = \frac{Td}{J} \tag{11.20}$$

where T is the torsion at each spar, d is the maximum distance from the centroid (in here $\frac{h_s}{2}$) and J is the torsion constant (for a rectangular cross-section $J = \frac{1}{3}h_s b_s^3$).

Torque at each spar can be calculated by equation 11.21,

$$T = GJ\frac{d\theta}{dz} \tag{11.21}$$

where G is the shear modulus and $\frac{d\theta}{dz}$ is the rate of twist. Total torque equals to the summation of torque at each spar ($T_{tot} = T_{s_1} + T_{s_2}$). By assuming that the rate of twist is equals for both spars, then equation 11.22 can be written,

$$\frac{T_1}{GJ_1} = \frac{T_2}{GJ_2} = \frac{T_{tot}}{G(J_1 + J_2)} \tag{11.22}$$

now by rewriting equation 11.22, the formulas for T_1 and T_2 can be derived as shown in equations 11.23 and 11.24,

$$T_1 = \frac{J_1}{J_1 + J_2}T_{tot} \quad (11.23) \qquad T_2 = \frac{J_2}{J_1 + J_2}T_{tot} \quad (11.24)$$

To calculate total torque (T_{tot}) shear centre must be calculated. Shear centre is the point through which the loads must act if there is to be no torsion. In other words, at the shear center the torque due to the external forces and internal shear flows must equals zero. The shear centre is always located on the axis of symmetry, therefore, by assuming that $\bar{z}$ is a symmetry line, the shear centre is on $\bar{z}$ line (see figure 11.8).

In figure 11.12 shows that shear centre is assumed to be at distance x from the front spar. By calculating the resultant moments abot shear centre, the unkown x can be defined (see equation 11.25),

$$\Sigma M_{@sc} = Lx + F_{q_1}x - W[x - (d_w - d_L)] + F_{im}[(d - x) - (d + d_L - d_{lg})] - F_{q_2}(d - x) \tag{11.25}$$

where L is the lift during touchdown, W is the MTOW and F_{im} is the impact load during landing on one landing gear. F_{q_1} and F_{q_2} are the internal forces due to the shear flows in the spars. These internal forces can be calculated by equation 11.26.

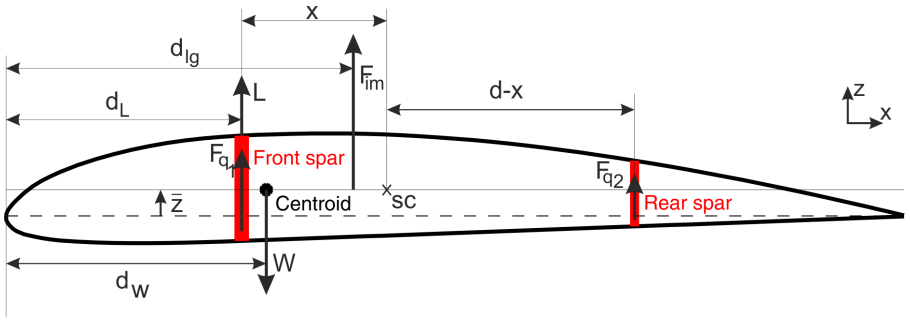

Figure 11.12: Shear centre and position of the loads

$$F_q = \int_0^s \mathrm{q_{yz}}\,\mathrm{d}s \tag{11.26}$$

By substituting q_{yz} from equation 11.18 and evaluating the integral, the shear force can be defined as,

$$F_q = -\frac{S_z b_s}{I_{xx}}(-\frac{h_s s^2}{4} + \frac{1}{6}s^3) \tag{11.27}$$

where again by using the boundary of 0 to h_s, shear force on both spars can be calculated by equation 11.28,

$$F_q = \frac{S_z b_s}{I_{xx}}(\frac{1}{12}h_s^3) \tag{11.28}$$

Now by substituting internal shear forces (F_q) of each spar in equation 11.25, the shear centre can be defined. After that by calculating the moment around shear centre only by using external forces, the total torque (T_{tot}) can be defined by equation 11.29,

$$T_{tot} = F_{im}(d_L + x - d_lg) - W(d_L + x - d_w) - Lx \tag{11.29}$$

Then by substituting T_{tot} in equations 11.23 and 11.24, torque on each spar can be calculated.

Table 11.5: Internal shear forces in spars due to the shear flows, shear centre and torque at each spar

$F_{q_{s_1}}[N]$	$F_{q_{s_2}}[N]$	Shear centre [mm] from front spar	$T_{s_1}[Nm]$	$T_{s_2}[Nm]$
786.41	119.91	57.52	5.66	0.86

Table 11.6: Shear stresses in spars due to the torsion

$\tau_{yz_1}[MPa]$	$\tau_{yz_2}[MPa]$
180.32	112.68

Results Using the same values for loads used in the previous section the shear center, torque at each spar are calculated (see table 11.5). To calculate J, the sizes of spar determined in section "Normal Stress" are used.

By substituting these values in equation 11.20, the shear stress due to torsion are calculated (See table 11.6.

These stresses are larger than the shear strength of spruce ($\tau_{spruce} = 9.3MPa$) which means failure occurs. To prevent this failure the thickness of the spars must be increased. To find the minimum size for spars the thickness of spars are increased by steps of 0.02 mm and in every step the new shear stress is calculated. This process continued till the shear stress become smaller than the shear strength of spruce. The final results are shown in table 11.7.

Table 11.7: Final shear stresses in spars due to the torsion

b_{s_1} $[mm]$	b_{s_2} $[mm]$	$\tau_{yz_1}[MPa]$	$\tau_{yz_2}[MPa]$
9.75	6.09	9.16	5.72

As it can be seen the thickness of the spars are increased about 2.7 times. This increment in sizes is expected since the open cross-sections have lower properties in torsion. It has to be noted that as it is mentioned before, it is assumed that all the torsion is carried only by the spars although it is not the case. There is foam between the spars which helps to withstand the shear stresses due to the torque. This assumption is made to simplify the calculations.

11.4.3 Ribs

In this subsection the design of the ribs is explained and the FEM analysis is discussed. After that, the results are given.

Design of Ribs

Ribs, as explained in section 11.2, are used to give the shape of the airfoil and withstand the bending about y direction. To simplify the calculation it is assumed only ribs are carrying the moment and shear forces. This assumption results in over designing the ribs as in reality, the foam between the ribs also takes some forces. Because of the connections of C-wing and internal systems to the body at the tip, one rib is placed at each tip of the wing (see figure 11.13). Furthermore, for the nose gear connection two ribs are positioned in the middle of the body.

As it can be seen in figure 11.13 most of loads are applied to the front and rear of the ribs while in the middle, the loads are not high. Therefore to save some weight, cutouts are made in the middle part of the ribs. This reduces the weight of the ribs by 35%.

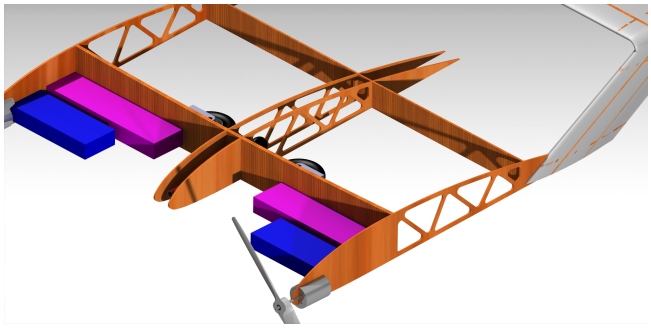

Figure 11.13: Ribs in the body

Due to the complex shape of the ribs and cutouts, hand calculation is not possible. Therefore, Finite Element Method (FEM) is used. Instead of analysing the whole aircraft only one of the ribs is studied using FEM. This simplified FEM model gives more reliable results. One of the ribs at the tip is analysed as these are carrying the most loads generated by the landing gear and the C-wing.

Rib Loading

In order to size the ribs, the loading on the ribs need to be determined. Since there is more load acting on the outer rib, this load is used to size all ribs. All the forces acting on the aircraft during landing are taken into account since this is the highest load case. Figure 11.14 shows the distances needed for the numerical analysis. The rib loading is determined with simple moment equilibrium and force equilibrium equations. The same method used in subsection 11.4.1 is also used to analyse the rib loading. The rib loading distribution is 84% for the outer ribs and 16% for the inner ribs.

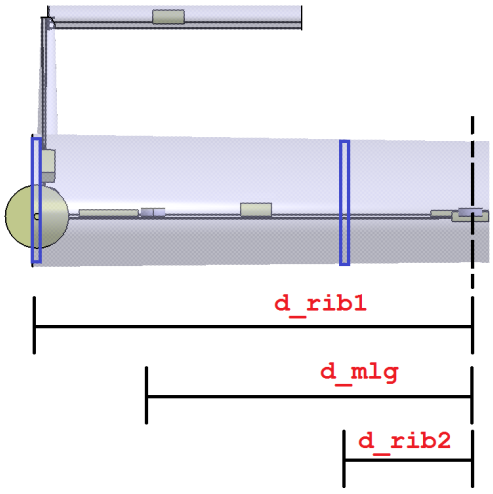

Figure 11.14: Distances from ribs and main landing gear to the center

FEM analysis

For FE analysis, the Abaqus [51] software is used and the mesh can be seen in figure 11.16. At some areas due to the curvature and sharp edges the mesh is refined. Figure 11.16 shows the loading on the rib. The spars (shown in red color in figure 11.16) are supported in such way that they are fixed in all axes. Since the landing gear is not attached to the the ribs, the impact load during landing on one landing gear is distributed over the front area of the rib. As it is explained before about 84% of the impact load is carried by the outer rib. The connection of the C-wing is attached to the rear part of the ribs, therefore, the loads and moments are distributed in the the whole rear area of the rib. Furthermore, the lift during landing is equally distributed over the top and bottom of the rib (shown by small arrows in figure 11.16).

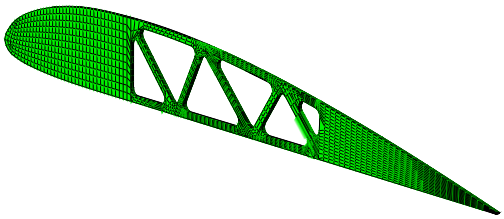

Figure 11.15: Mesh of rib in Abaqus

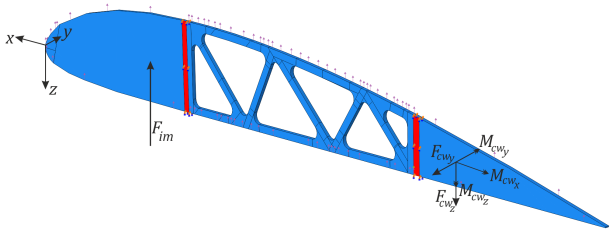

Figure 11.16: Loadings on the rib in Abaqus

The loads due to landing impact and the C-wing used in the FE analysis are shown in table 11.8. It is assumed that there is gust during landing , so the lift is multiplied by gust load factor of 3.8. For the other loads a safety factor of 1.5 is used. In addition, mechanical properties of spruce is used for this analysis.

Table 11.8: All the loads used in the FE analysis by taking into account the gust load factor and safety factor

$F_{im}[N]$	$L_{touch-down}[N]$	$F_{cw_y}[N]$	$F_{cw_z}[N]$	$M_{cw_x}[Nm]$	$M_{cw_y}[Nm]$	$M_{cw_z}[Nm]$
792.5	233	30.45	133.35	24.9	58.95	10.69

Results The result of the FE analysis is shown in figure 11.17. The maximum von Mises stress in the rib is about 20 MPa in the cutout. As it is expected there are large stresses (about 15 MPa) next to the rear spar (area B in figure 11.17) due to the C-wing loads and moments. Furthermore, there are large stresses (about 19 MPa) next to the front spar (area A in figure 11.17) as a result of the impact load. To check that if failure occurs in the ribs, the stresses must be compared to the von Mises stress of spruce. The von Mises stress of spruce wood can be calculated using equation 11.30[35],

$$\sigma_y = \sigma_1^2 + \sigma_2^2 - \sigma_1\sigma_2 + 3\tau^2 \tag{11.30}$$

where σ_y represents the von Mises stress (failure criterion). σ_1 and σ_2 are principle stresses which in this case are tensile and compression stresses of spruce. τ is the shear stress of the spruce. By substituting these values the von Mises stress of spruce is 68.3 MPa. Although the stress in the rib is much smaller than the failure criteria, a thickness of 5 mm is selected for the ribs for easier handling during production. Dimensions of the cutouts can be founnd in the CATIA document. As can be seen

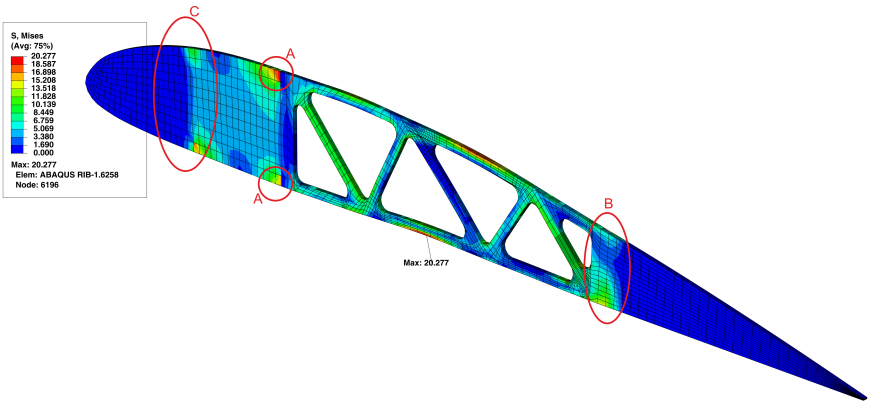

Figure 11.17: Von Mises stress in the ribs

in figure 11.17 there is a strange behaviour in area C where no explanation could be found. Further investigation is needed to fix this problem or find a reason for this behaviour. Even though the results are unexpected they are still well below the limiting failure stress.

11.4.4 C-wing

In this section the structure of the C-wing will be discussed. Since the C-wing is only fixed to the body at one end, relatively high stresses will be encountered at this connection and higher levels of deformation are to be expected. An isometric view of the C-wing is shown in figure 11.18. For the following calculations the C-wing will be split into two sections: a horizontal section and a vertical section, see figure 11.19 for a Free Body Diagram of both sections in front view. To maintain a clearer overview the reaction moments acting at the root of the C-wing, M_x, M_y and M_z, are not displayed. One thing to note is the lift force of the horizontal section is acting downwards.

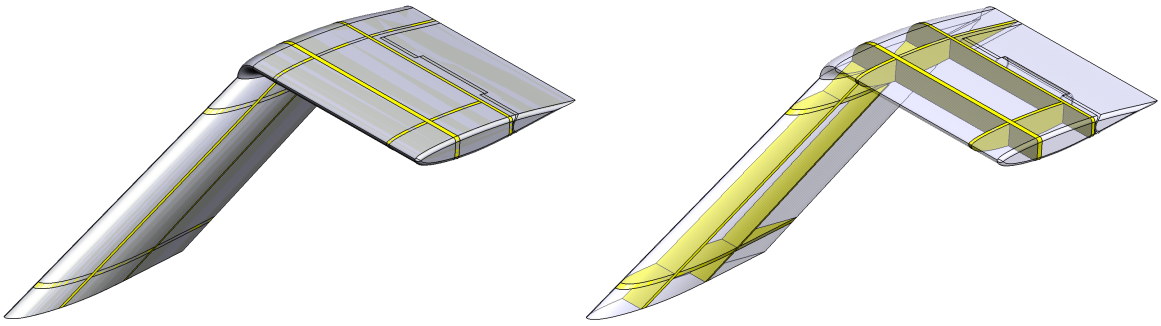

Figure 11.18: Isometric view of the C-wing, with skin (left) and without skin in combination with transparent foam (right).

C-wing Structure

The structure of the C-wing, as can be seen in figure 11.18, consists of two continuous spars and four ribs, made of spruce. The spars start at the connection with the main body and end at the tip of the horizontal stabilizer. The first spar is located on the quarter chord line, where the resulting lift force will act, and the second is located just in front of the control surface of that section (i.e. rudder or elevator) in order to maximise inertia while acounting for control surface spacing. The ribs are located

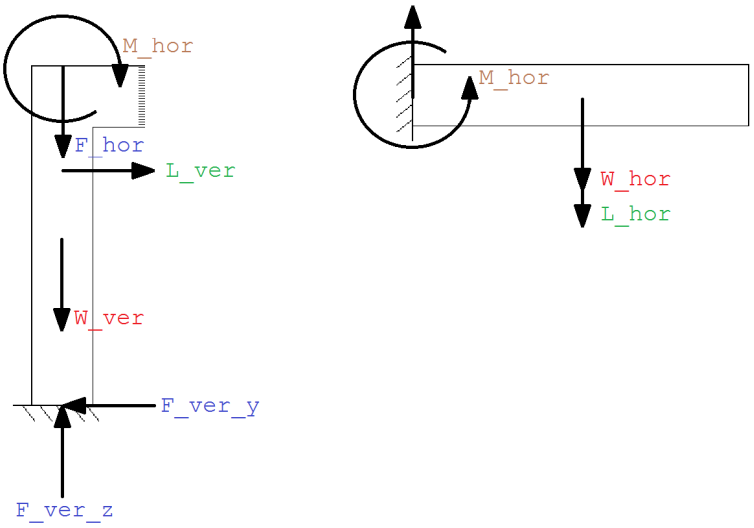

Figure 11.19: Free body diagram of the C-wing split into two sections, the vertical (left) and the horizontal (right) - definitions of parameters can be found in the nomenclature.

at the sides of the control surfaces except for the rib at the C-wing tip, this placement will allow for optimal control surface intergration. Furthermore, the space in between the spars, ribs and skin will be filled with solid foam. The thickness of the spars will be determined by the highest load that the structure needs to be able to withstand.

Assumptions & Simplifications

Several assumptions and simplifications were made in order to make the calculations feasible, these are summarised here:

- For the deflection angle the vertical component is simplified to a straight vertical (no sweep) beam, clamped to the body.
- For the deflection angle the horizontal component is simplified to a horizontal beam, clamped to the vertical.
- The weight and lift force of the horizontal component are assumed to act at the quarter chord line at half the span of the horizontal.
- The weight force of the vertical component is assumed to act on the half chord line at half the span of the vertical.
- The lift force of the vertical component is assumed to act on the quarter chord line at three-quarters of the span, measured from the root.
- The cross-section used for inertia calculations is assumed to be symmetric around the chord-axis.
- The cross-section used for inertia calculations for the vertical section is assumed to be constant (no taper) and equal the cross-section at the tip (smallest inertia value).
- The drag on the C-wing is assumed to be neglectable.

Table 11.9: Deflection angles for the horizontal section, vertical section and total C-wing.

Component	Deflection [rad]	Deflection [deg]
θ_{hor}	0.0045	0.2583
θ_{ver}	0.0115	0.6612
θ_{tip}	0.01600	0.9194

Table 11.10: Normal stresses experienced by the spars and the tensile & compressive strength of spruce.

Component	Stress [N/mm^2]
σ_{h1}	20.48
σ_{h2}	28.00
σ_{v1}	20.73
σ_{v2}	33.57
Tensile strength	76.20
Compressive strength	45.20

- For the torsion calculations the cross-section is assumed to have double symmetry for shear centre calculations.

Angle of Deflection

The deformation due to the loads on the C-wing needs to be within acceptable limits. The acceptable angle of deflection for the tip of the C-wing should be 1° or less. The deflection angle, θ, of the C-wing tip is determined by equations 11.31, 11.32 and 11.33 (in radians).

$$\theta_{hor_x} = \frac{L_{hs} \cdot (0.5 \cdot b_h)^2}{2 \cdot E_{spruce} \cdot I_h} \tag{11.31}$$

$$\theta_{ver_z} = \frac{L_{vs} \cdot \left(\frac{3}{4} \cdot b_v\right)^2}{2 \cdot E_{spruce} \cdot I_v} + \frac{M_h \cdot b_v}{E_{spruce} \cdot I_v} \tag{11.32}$$

$$\theta_{tip} = \theta_{ver_z} + \theta_{hor_x} \tag{11.33}$$

The deflection angles for a spar thickness of $4mm$ is shown in table 11.9.

Normal Stresses

As the spar thickness is determined by the deflection calculation, the ability of the C-wing to withstand the experienced normal stresses can be checked with equations 11.8.

The respective normal stresses (per section, denoted by 'h' and 'v', and per spar, denoted by '1' and '2') are displayed in table 11.10 along with the compressive strength and tensile strength of spruce. As can be seen from the table neither the tensile strength nor the compressive strength will be reached, the structure will not fail.

Table 11.11: Shear stresses experienced by the spars due to internal shear forces and the shear strength of spruce.

Component	Stress [N/mm^2]
τ_{h1}	1.07
τ_{h2}	1.25
τ_{v1}	0.96
τ_{v2}	1.22
Shear strength	9.30

Table 11.12: Shear stresses experienced due to Torsion by the vertical spars and the shear strength of spruce.

Component	Stress at 4mm thickness [N/mm^2]	Stress at 10mm thickness [N/mm^2]
τ_{v1}	93.55	5.99
τ_{v2}	73.52	4.71
Shear strength	9.30	9.30

Shear Stress due to Internal Shear Forces

The shear stress due to internal shear forces is given in equation 11.34. The shear stresses per section per spar are listed in table 11.12 along with the shear strength of spruce. As can be seen in the table the shear stresses in the spars are far below the shear strength of spruce which means that the structure holds.

$$\tau = \frac{F \cdot Q}{I \cdot t} \tag{11.34}$$

Shear Stress due to Torsion

The shear stress due to torsion is given by equations 11.20 to 11.29. The shear stresses per spar of the vertical section are listed in table 11.12 along with the shear strength of spruce. At a vertical spar thickness of 4mm the shear stresses due to torsion are too high. However, as can be seen the shear stresses at a spar thickness of 10mm are sufficiently low to avoid failure. Note that this update in vertical spar thickness is not implemented due to time constraints and further research is recommended to be done, preferably without the aforementioned simplifications. This increase in thickness will lead to an increase in tail weight which will affect MTOW and stability.

11.5 Component Connections and Skin

In this section, the skin along the whole body is discussed, and the skin close to the engine and payload storage is discussed more specifically. In the second part the connection of the C-wing to the main body is discussed, in the third part the connection of the engine and the connection of the payload and battery is discussed.

11.5.1 Skin

Since the skin is not assumed to take any loads, the skin is made quite thin. It can be made of several different material but the easiest material to use would be a easily deformable material. The

skin is made around the solid foam. The foam provides stiffness to the skin and determines the body shape. The skin is used in order to close the structure and improve the aerodynamic properties. For now, plastic film is chosen for the skin material as it is lightweight, cheap, and has good aerodynamic properties. For the final production, the material choice is left open for NPU; it can be made of thin wood, plastic of even fibre if it is preferred for this application. During the design of the skin, it has to be kept in mind that the hatch made on top of the payload and batteries (to close the gap) is not allowed to be made of plastic as the batteries will heat up and melt the plastic. The material will deform which influences the aerodynamic properties significantly.

11.5.2 C-wing Connection

As for the connection between C-wing and body it is recommended to investigate two options. The first option is to add aluminium braces at the critical points: between the body and the C-wing as well as between the horizontal and vertical section. These braces will reinforce the spruce connections and assist in transferring the loads. The second option is to use a solid wood base for the C-wing and if deemed necessary, a solid wood connection between the horizontal and vertical section to avoid failure at these points. A third, lighter, option is to have the spars of the C-wing interlock with the spars of the main body, they would slide into each other and can be glued in place or can be done in combination with aluminium braces.

11.5.3 Engine Mounting and Integration

The propeller engines are mounted at the aircraft's wingtips. Due to symmetry, the resultant moment created by the engines is zero in the center line of the aircraft. The moments need to be introduced into the structure in a proper way. The front spar transfers the moments to the other side of the structure. First the mounting of the engine itself is discussed, after which the way moments are introduced is discussed.

To mount the engine onto the structure, an engine mounting is used to have an easier way of holding the engine. The engine manufacturer has designed a mounting which is strong enough to withstand the engine forces and moments. The engine used for the UAV is discussed in Chapter 7. The mounting produced by the same manufacturer is shown in figure 11.20. The engine in the figure is not the engine used for the UAV, the picture is only used to show the engine mounting.

Figure 11.20: Engine mounting produced by the engine manufacturer [52] (left) bottom view of the UAV, engine integration (right)

Since the motor is not placed close to the spar, a connection is made. The engine is producing large

normal forces and a moment in the opposite direction with respect to the rotation of the propeller. A reinforcement is added to the structure to bear the loads. Figure 11.20 shows the connection between the engine and the front spar. The orange dashed lines indicate the engine mounting as can be seen in the left of the figure. The brown diagonal truss is placed to deal with the shear loadings due to gusts, side slip and other situations. The red part indicates a material which introduces the moments and normal forces into the rib and front spar. Since the rib is quite thin and not rigid against torque, the connection is made all the way to the front spar. This can be made by wood or other lightweight materials which are strong enough. Due to the lack of time, analysis on this integration is not possible and it is recommended that NPU considers this in more detail.

Since the engine is partly outside the body of the aircraft (see figure 11.21a), the airstream is slightly disturbed. The red connection shown in figure 11.20 and figure 11.21b is used to fully integrate the engine. Figure 11.21b shows the sideview of the engine integration. The aerodynamic properties are less interrupted by the connection than by the engine without casing.

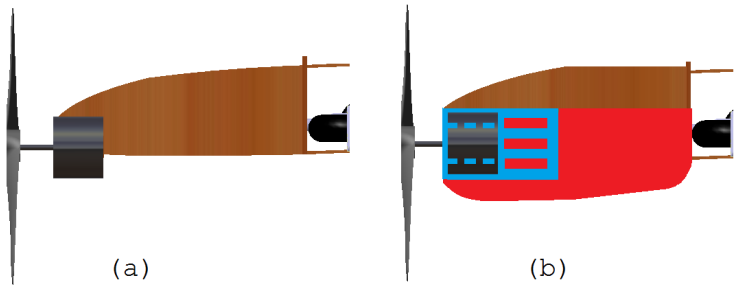

Figure 11.21: Sideview of the engine mounting and integration, without integration (a) and with integration and connection (b)

11.5.4 Payload and Battery Storage

The way to store the payload and battery is kept quite simple. A box is made and filled with the payload or batteries. The box is used to retrieve the batteries and payload easily, and to separate them from the rest of the structure. Figure 11.22 shows a visualisation of how the boxes are integrated in the structure. These boxes are made of plastic and the type of plastic depends on how warm the batteries will become during flight. The boxes are placed on top of the diagonal truss mentioned in the previous subsection (see figure 11.20). The gap in the skin is closed with a hatch. This prevents the loss of aerodynamic properties.

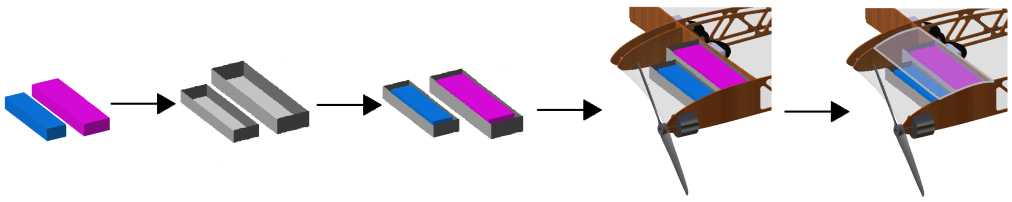

Figure 11.22: Visualisation of the payload and battery storage

11.6 Weight and cost

In this subsection the weights and costs of the whole structure (with respect to the materials) is discussed. The manufacturing is not discussed since this is done by NPU and the manufacturing costs are unknown to us.

In the table 11.13, the weights and costs of each part of the structure are shown. The weight of each part is measured in the CATIA model. The price is price density multiplied by the weight and the safety factor. The price of spruce wood is €0.50 per kilogram [53] while the price of one kilogram of Rohacell foam costs €100.97 [54].

Table 11.13: Weight and cost of structural components of the body

Part name	No	Material	Weight [kg]	Price [€]
Front spar	1	Spruce	0.687	1.50
Rear spar	1	Spruce	0.259	0.60
Inner ribs	2	Spruce	0.267	1.20
Outer ribs	2	Spruce	0.35	1.50
Foam	-	Rohacell 51	3.710	561.91

Table 11.14 shows the component weights and costs of the C-wing.

Table 11.14: Weight and cost of structural components of the C-wing

Part name	No	Material	Weight [kg]	Price [€]
Front spar	2	Spruce	0.067	0.3
Rear spar	2	Spruce	0.040	0.3
Vertical ribs	4	Spruce	0.033	0.3
Horizontal ribs	4	Spruce	0.025	0.3
Foam	-	Rohacell 51	0.157	23.62

11.7 Sensitivity

The structure is sensitive for many types of change in the design. The most sensitive changes come from Aerodynamics, Stability, and the Landing gear. In case of changing any of the aerodynamic parameters, the structure has to be checked. For example, a thicker airfoil results in a larger and heavier structure. Different lift distribution results in a different structure configuration. Changes made with respect to stability can also affect the structural design. For example, if the tail is swept back more for a larger tail arm, the connection between C-wing and the body has to be reinforced. A change in location of the control surfaces and stabiliser surfaces is also affects the structure greatly as this affects the locations of the ribs and spars. The landing gear influences the structure by defining the location for the connections of the mechanisms and by the load factor it creates during landing. Smooth and really good shock absorbers can half the impact force. Any changes for these parameters result in an increase of structure characteristics required. All the changes made for the structure and materials, result in a change of MTOW and change of the c.g. location. This also influences the structure and hence the structure design is an iterative process.

11.8 Recommendations

Since the connections with the body are not detailed designs, it is recommended to start with detailed designs of each existing connection. Finding specific wood samples with the exact mechanical properties is also difficult as data sheets for woods are not readily available, as compared to that of metals. The only way to find the right spruce wood is to compare their densities; companies usually have the required information.

For the structure of the UAV, a trade-off between weight and cost exists. The structure can be made from advanced materials such as carbon fibre, which is expensive but much lighter. For example, using carbon fibre would decrease the thickness of spars by a factor of 3, reducing the structure to one-third its original weight. The selection of spruce wood was based on NPU's suggestion due to its low cost. However, advanced materials could be used to improve efficiency, sacrificing cost for weight.

Furthermore, by changing the rectangular cross-section of spars to I-beams, the second moment of inertia would remain the same, but weight will be reduced by about 60%. However, this change would require advanced tools, such as the 5-axis milling machine, which are very expensive.

12 Iteration

Before the final design is obtained, some iterations are performed. Iterations are necessary since the aircraft has to meet performance requirements. Before a design iteration is performed, the parameters to be changed are selected. It should be pointed out that changing the other design parameters, such as wing area and AR, have a major influence on the overall performance, aerodynamics, structural and stability characteristics of the UAV. Hence such a design change was not incorporated due to lack of time. The main iteration is started by an increase of the engine power. This is discussed in section 12.1. The other disciplines are also affected by the change of the engine power, this chapter discusses the results of the whole iteration of the UAV design. Every discipline is classified in a section.

12.1 Performance and Propulsion

It was found from initial performance results that the range and climb gradient requirement are not met and the maximum velocity is too close to the cruise speed. As such, the maximum engine power as well as the propeller pitch has to be changed to accommodate higher flying speed. Due to these reasons, the group decided to increase the maximum achievable power and thrust of the engine. The designed operating rpm of the propeller was adjusted from 5900rpm to 6800rpm. The static thrust of the propeller was increased from approximately 70 KN to 95 KN per engine. This came at a cost of heavier engine and battery mass. The battery capacity was also increased in order to meet the range requirement. It should be pointed out that the increase in engine power improves both takeoff and climb performance with little weight penalty. It was found that the increase in total mass due to the use of larger engines is lesser as compared to design parameter changes such as wing area or aspect ratio. Design parameter changes such as wing area or aspect ratio has a large influences on the overall structural mass. The performance analysis of the initial and final UAV design are shown in table 12.1, and are compared with the results in table 8.3.

Table 12.1: Iteration results performance and propulsion.

Performance Parameters	Value	Velocity [m/s]	AoA [deg]
Range [km]	96.82	36.93	2
Endurance [Hours]	0.85	28.29	8
Maximum climb gradient [deg]	40.94	22.58	16
Maximum climb rate [m/s]	15.96	24.79	12
Maximum descent gradient [deg]	19	18.54	35
Takeoff distance (Analytical) [m]	78.22	-	-
Takeoff distance (Numerical) [m]	77.76	-	-
Landing distance (Analytical) [m]	114.15	-	-
Landing distance (Numerical) [m]	121.07	-	-
Maximum Velocity [m/s]	46	-	-
Stall Velocity [m/s]	19	-	-
Maximum Load factor	2.6	35	-
Minimum Turn radius [m]	42.28	26.43	-
Minimum time to turn [s]	9.24	35	-

There is an significant improvement in the maximum range and climb gradient of the final UAV design. The maximum climb gradient was increased from 21.93° to 40.94°. It should be pointed out

that the battery capacity was increased from 666 watt hours to 917 watts hours. This is mainly due to the increase in engine power requirement as well as the need to meet the range requirements. It should be pointed out that the actual battery capacity provided differs from the battery capacity required since this depends greatly on the actual type of battery cell used and its configuration. Hence, the final achievable range will exceeds the design requirement. The increased thrust provided by the new propulsion system provides better turn performance at the expense of higher manoeuvre load on the entire structure. Also, the increase in thrust has negligible impact on the landing distance. Although there is an increase in engine and battery mass, the overall mass stay almost constant since the total structural mass was reduced for the final design iteration. As such, the required landing distance before and after iteration stays almost constant. Finally, it should be pointed out that the only design requirement not met in the final design iteration is the maximum descent gradient. Although it is possible to increase the maximum descent gradient through an artificial increase of the drag during the descent phase, such a enhancement is not considered to be 'innovative' and defeats the purpose of designing a low AR UAV in the first place. The result of this iteration would be verified in the requirement compliance matrix.

12.2 Aerodynamics

The main change for the aerodynamic performance is the propeller change. This means larger induced velocities are present which means generally better aerodynamic performance. It becomes clear that the lift to drag ratio increases with 3.7%, the according angle of attack is slightly lower (0.5^circ). This results in a larger C_L in cruise, which allows for lower speeds or larger weights. With the new weight of 23.13kg, the speed can only go down by 0.6m/s to maintain vertical equilibrium.

12.3 Stability

After the iteration, the changes that affects stability of the UAV is the change in MTOW, c.g. location and the MMOI. The new values used for the iterated design are:

- MTOW $= 21.94kg$
- c.g. location $= 0.292m$
- $I_{xx} = 1.95\frac{kg}{m^2}$
- $I_{yy} = 1.825\frac{kg}{m^2}$
- $I_{zz} = 3.667\frac{kg}{m^2}$
- $I_{xz} = 0.256\frac{kg}{m^2}$
- $I_{xy} = 0.1972\frac{kg}{m^2}$
- $I_{yz} = 0.0125\frac{kg}{m^2}$

With the new values, the new model is analysed in Tornado and AVL for cruise condition and the results are compared to the cruise condition before iteration. The comparison can be seen in figure 12.1

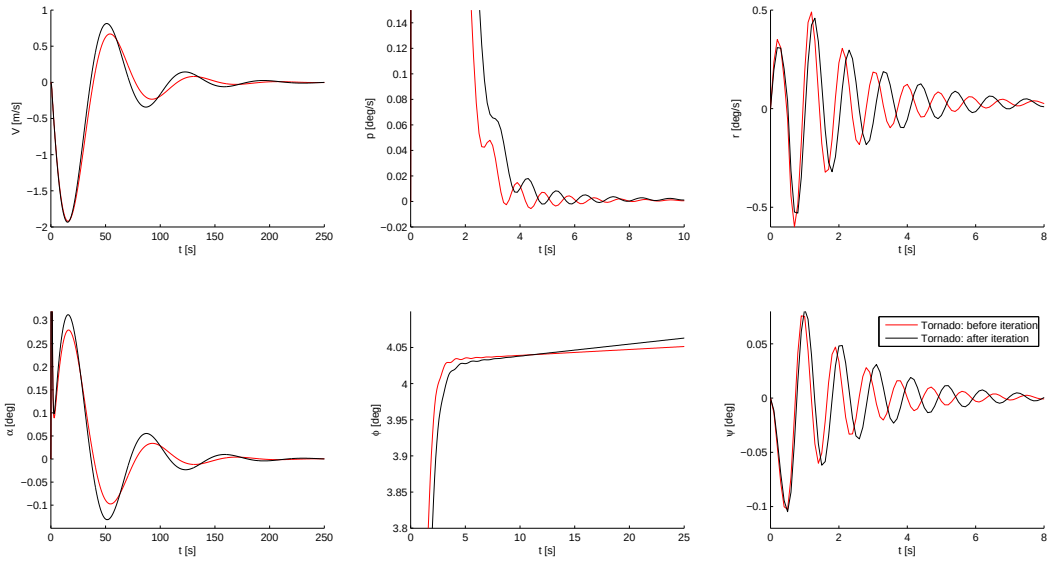

Figure 12.1: Comparison of response curves for Tornado before and after iteration.

The comparison is only plotted for the Tornado results as these are slightly more accurate than AVL results. Also, the changes before and after iteration in AVL closely mirrors the Tornado changes. From figure BLA, it can be seen that the change in stability is negligible. For the symmetrical motions, the elevator is more effective after iteration as the initial peak after the deflection is higher for both

Table 12.2: Time to half amplitude for symmetric and asymmetric motions before and after iteration

	$T_{1/2}$ Symmetric [s]	$T_{1/2}$ Asymmetric [s]
Before iteration	25.2	1.4636
After iteration	28.6	1.7312

V and AoA. This not the case for asymmetric motions as the initial peaks for both roll and yaw are higher for the before iteration case. The $T_{1/2}$ for both symmetric and asymmetric motions are shown in table 12.2. It can be seen that for the short period, the $T_{1/2}$ increased after iteration by about 13.5%, which means that the design after iteration is less stable as more time is required to damp the perturbations out. For the asymmetric motions, the $T_{1/2}$ is also found for the yaw motion. From the values shown in table 12.2, it can be seen that after iteration, the $T_{1/2}$ increased by about 18.3%. The roll rate also damps out slower for the iterated design and the increase in roll angle is more obvious. Hence for asymmetric motions, the iterated design is less stable as well.

It can be concluded that by increasing the engine power, the stability of the design decreases. The effectiveness of the elevator increase but this is not the case for the rudders and ailerons. However, this decrease in stability is not very significant as the change in speed and angles is in the order of 10^{-1} for symmetric motion and 10^{-2} for asymmetric motions. The decrease in stability can also be reduced by shifting the batteries and payload forward so that the S.M. is larger.

12.4 Controllability

For the first iteration the power is increased. This increased power leads to an increase of MTOW as well as a c.g. shift from 0.2900 to 0.2917. As a result the S.M. decreases, but the moment arm of the control surfaces decreases as well. Because of the increase in MMOI, the pitch, roll and yaw damping increases. This *can* make the control surfaces less effective. Only the cruise phases is investigated for this iteration. The result for trim is an elevator deflection of -8.49716° for AVL and -7.743° for Tornado. Compared to the previous values of table 6.7. The decrease in S.M., decrease of moment arm and increase in MMOI resulted in a slightly higher trimmability.

12.5 Landing gear

The iteration of Tip-C, where the trust increased, did not have direct influence on the landing gear design. Although the engine increased in size and therefore the total maximum takeoff as well. The thicknesses did increase slighty due to the increase in loads on the struts. However since the components are bought from the market and the variety in these components is not too big, this small change in MTOW did not change the design of the landing gear after iteration.

12.6 Aircraft Systems

For the aircraft system, the changes in parameters are negligible. The system components depend on the availability of buying it somewhere. This already means there is a margin since the aircraft components are not always perfectly designed. In the case of the increasing power, in the end, no aircraft systems are changed.

12.7 Structure

Due to the increase of engine power (and a bigger engine), the structure has its changes. Only the increase in MTOW is influencing the structure significantly. The main aspect which is taken into account is the extra force created during landing due to the increased MTOW.

12.7.1 Loads

For the loadings acting on the aircraft, the change in engine weight is influencing the loading diagrams but does not affect the maximum loading. The main influencing factor is the force introduced by the landing gear during landing. Figure 12.2 shows the new shear force and moment diagrams after the change of the design during the first iteration. As can be concluded, the changes are marginal with respect to the values found earlier. But the changes are high enough to make changes in the structure. The new maximum loads are $M_x = 280[Nm]$ and $V_z = 636[N]$.

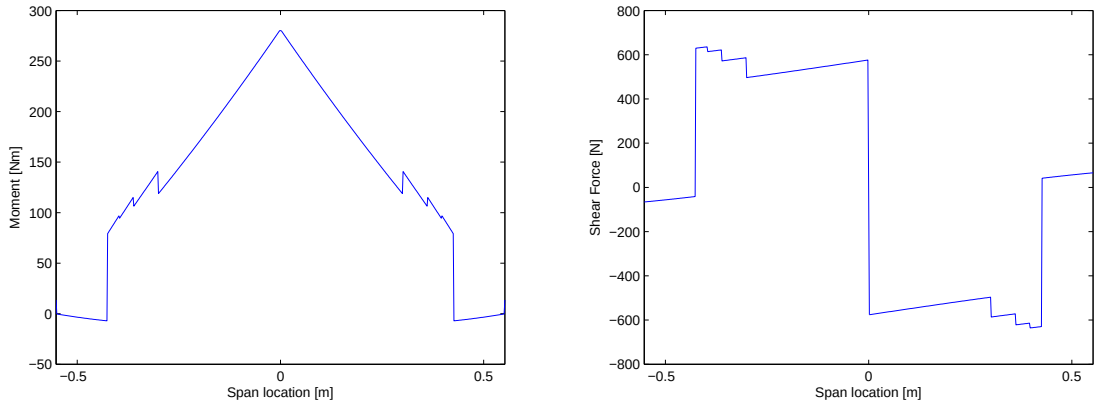

Figure 12.2: Moment diagram (left) and shear force diagram (right) after iteration

12.7.2 Body

Due to the larger loads the sizes of the spars increases. The results after iteration are shown in table 12.3.

Table 12.3: Final shear stresses in spars due to the torsion after iteration

b_{s_1}	b_{s_2}	$\tau_{yz_1}[MPa]$	$\tau_{yz_2}[MPa]$
10.32	6.45	9.24	5.77

As it is explained in section 11.4.3 the von Mises stress in the ribs are very smaller than the failure criterion of spruce, therefore, due to the sake of time no iteration FE analysis is done. In conclusion, the sizes of the spars stays the same.

12.7.3 C-wing

The influences the iteration has on the C-wing is negligible. The structure of the C-wing remains unchanged.

13 Comparison to Reference Aircraft

In order to get an idea about how well the design performs, it is compared to similar existing aircraft. These aircraft are all low aspect ratio aircraft, having an AR of 3 or less. They are not necessarily conventional aircraft, some being flying wings and other having non-conventional tail layouts etc. The structural efficiency, aspect ratio, wing loading and power loading of these aircraft are presented in table 13.1 along with the data for Tip-C for comparison. An illustration of the data are given in figures 13.1, 13.2 and 13.3. Additionally, the Tip-C is compared to other UAV's in this weight and size class with the data shown in table 13.2. Reference is made to conventional aircraft; conventional being full scale, general aviation, high AR (>4) and fuselage, wings and aft tail layout.

As can be seen from table13.2, the structural efficiency of Tip C (0.23) is comparable to UAV's of similar weight class (≈ 0.3) but it is lower compared to other large scale low AR aircraft ($\approx .0.5$) in table 13.1. Very little data can be found on the aerodynamic performance of the reference aircraft. For the data found, Tip-C has a better L/D ratio. This compensates the lower structural efficiency, resulting in a higher transport efficiency than would otherwise be.

It is also found from table 13.2 that the structural efficiency of these small scale aircraft (UAV) is much lower than the full scale low AR aircraft in table 13.1. This could explain why Tip-C (small scale) has a lower structural efficiency than the full scale low AR aircraft. This lower structural efficiency leads to a comparatively lower transport efficiency compared to full scale low AR aircraft.

As noted earlier, low AR aircraft traditionally have higher structural but lower aerodynamic efficiency than conventional aircraft. Tip-C is found to have a very similar structural efficiency compared to the Cessna 150, being a conventional aircraft, conventional as explained before. It should be pointed out that since the Lift to Drag ratio of Tip-C is slightly higher than these aircraft, the overall transport efficiency of Tip-C is found to be similar (1.85 vs. 1.8).

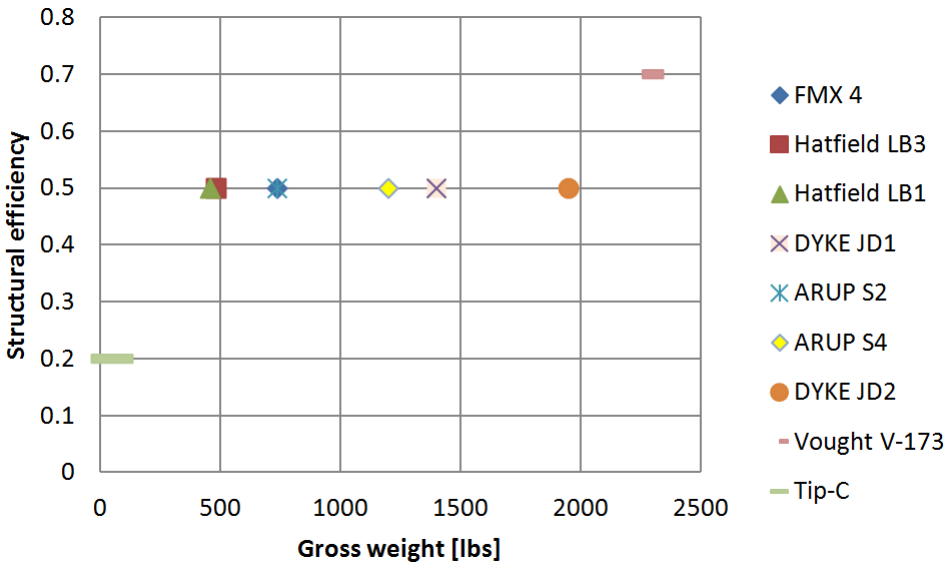

Figure 13.1: Power loading versus wing loading of low aspect ratio UAV.

Table 13.1: Reference data for low AR aircraft

Aircraft type	Gross weight [lbs]	Useful Load [lbs]	Structural eff. (W_{pay}/MTOW) [-]	L/D [-]	Transport eff. (W_{pay}/MTOW) [-]	W/S [N/m^2]
FMX-4	740	370	0.5	7.2	3.6	164.8
Hatfield LB3	483	230	0.5	unknown	unknown	unknown
Hatfield LB1	458	210	0.5	unknown	unknown	152.1
DYKE JD1	1400	675	0.5	unknown	unknown	unknown
ARUP S2	740	340	0.5	3.0	1.5	168.0
ARUP S4	1200	650	unknown	unknown	unknown	210.2
DYKE JD2	1950	890	0.5	unknown	unknown	542.3
Vought XF5U-1	16722	13107	0.8	unknown	unknown	1687.3
Vought V-173	2258	1655	0.7	unknown	unknown	227.3
Sack AS-6	1984	unknown	unknown	unknown	unknown	4540.0
Tip-C	51	11	0.23	8.1	1.6	189

Aircraft type	Wing area [m^2]	V_{stall} [m/s]	Takeoff dist. [m]	Landing dist. [m]	AR [-]	Wing span [m]	W/P [N/W]
FMX-4	19.9	14.9	304.8	unknown	1.1	4.6	0.0892
Hatfield LB3	unknown	unknown	unknown	unknown	1.8	unknown	unknown
Hatfield LB1	13.4	11.3	unknown	unknown	2.0	5.2	0.1014
DYKE JD1	16.0	19.2	unknown	unknown	2.2	6.9	unknown
ARUP S2	19.6	10.3	unknown	unknown	2.4	5.8	0.1220
ARUP S4	25.4	10.3	unknown	unknown	1.8	6.7	0.1027
DYKE JD2	16.0	33.5	213.4	304.8	2.9	6.8	0.0648
Vought XF5U-1	44.2	20.6	283.5	unknown	2.2	9.9	0.0363
Vought V-173	44.2	20.6	61.0	unknown	1.1	7.1	0.0837
Sack AS-6	19.6	unknown	unknown	unknown	1.3	unknown	0.0493
Tip-C	1.14	19.0	78	102	1.1	1.1	0.044

Table 13.2: Reference data for UAV's in the same size and weight class

UAV name	MTOW [kg]	W_pay [kg]	Structural eff. [-]
Blue Bird Aero System Boomerang	10	1.3	0.13
Bayraktar Mini UAV (B version)	4.5	1.5	0.33
Institu Scan Eagle	20	1	0.05
Arcangel 1	25	10	0.40
Penguin B	21.5	10	0.47
Mini Panther UAS	12	2	0.17
Micro V	45.5	8	0.18
Tip-C	21.94	5	0.23

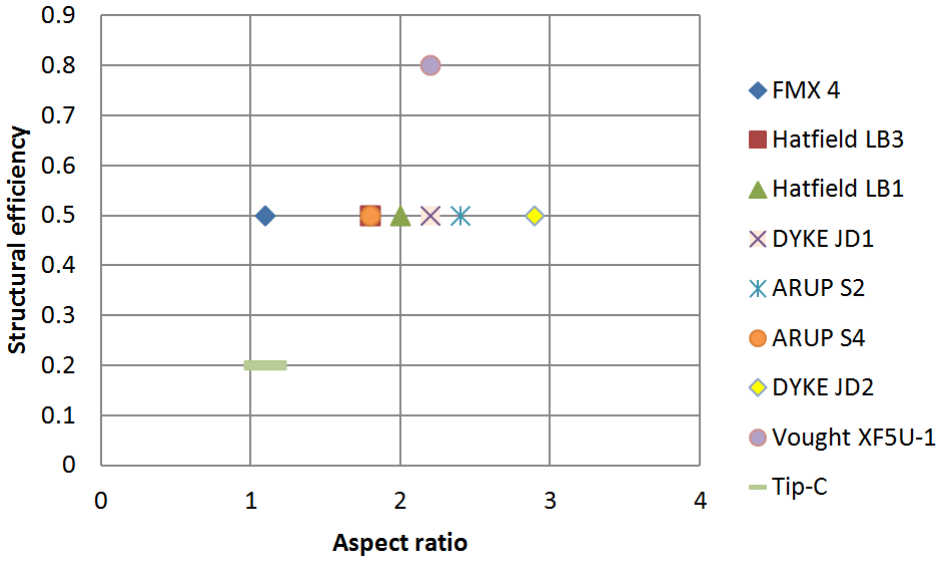

Figure 13.2: Structural efficiency versus aspect ratio.

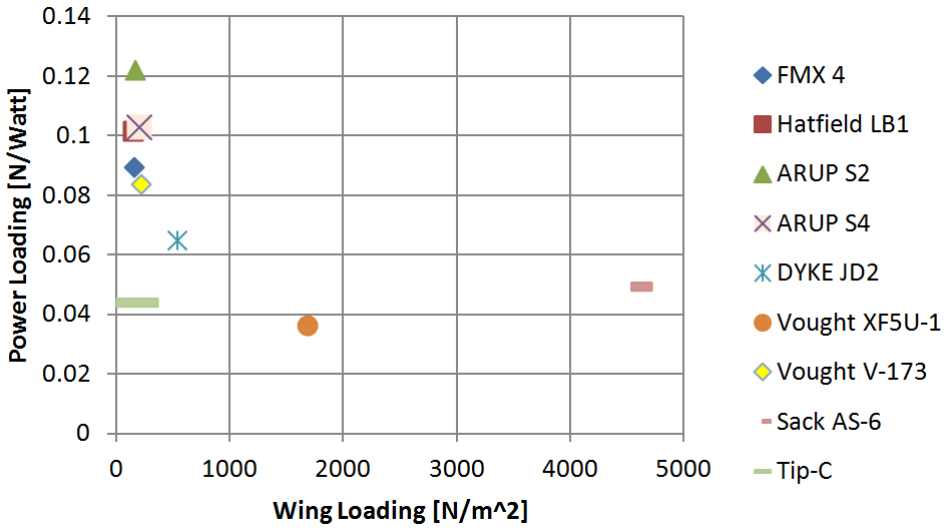

Figure 13.3: Structural efficiency versus gross weight.

14 Production Plan

In this chapter the production plan of the UAV is explained in general. The production is mostly related to the structure since other components must be bought. As it is explained in chapter 11 the structure is made out of spruce wood and foam. To buy the raw material it is recommended to add about 50% of the material needed because of waste material during production and some margin. The thicknesses shown in chapter 12 are the results of calculations. For example it is not practical to make the thickness of wood to 10.32 mm therefore it is suggested to round up the thicknesses to accuracy of 0.5 mm. For each part of structure some production methods as suggestions are explained briefly below.

Spars Although Spars has a simple rectangular cross-section, their height are defined based on the thickness of the body or C-wing which increases from center to the tip (see appendix A). To make this curvature, the drawing of the spar can be printed full scale on number of A3 papers and tape them together and placed it on the wood and mark it and cut it by hand saw. Another way is using CNC machine which is more expensive. This way your product is very accurate. At the end of both process sanding is needed to have a good finishing surface.

Ribs Shape of ribs has more curvature and needs to be more accurate since it give the shape of the airfoil to the body. In addition, the cutouts make it harder to do it by hand. It is recommended to use CNC machine for the ribs. In case of no CNC machine available, jewelry saw (see figure 14.1 can be used. For marking the shape by printing the shape in scale as explained for spars can be used. Sanding has to be done for a good finishing surface.

Figure 14.1: Jewelry saw for cutting curved shapes [55].

As it can be seen in CATIA drawing in appendix A, in the intersection between the ribs and spars, ribs are cut. To have larger tolerance, it is highly recommended to make the ribs in one peace to the shape of the airfoil and then cut the areas where spars goes through.

Foam Foam fills all free space in the body. Making the foam with all the cutouts for components must be done after the detail design of the components' connections by NPU. They can make a solid foam (with the cutouts) in the CATIA model, and produce it by using CNC machine. Due to the double curvature of the body it is not possible to make it by hand.

Connection of each component is not detailed designed, therefore NPU has to come up with the production plan.

15 Flight Test Plan

Before Tip-C is flown at the competition, it has to be tested first to make sure that it performs as expected. Through a flight test, some features which cannot be accurately simulated with CFD or wind tunnel data can also be found. This is useful not only for the fine-tuning and flying of the design, but also for validating the innovative features. Hence, a test plan is formulated to ensure that the testing of the design is done in a systematic order.

A 1:1 scale model of Tip-C should first be made for the test. The dimensions, weights and locations of parts should be as accurate as possible with the final design. The test should first start with testing out the mechanical systems such as the servos and actuators to make sure that they are working. Tests should also be carried out to make sure that all expected deflection angles of the control surfaces and the belly flap can be reached within the designed deflection rates. The extension and retraction of the landing gear should be correct and the brakes should work as expected. The engine and propellers should also be tested on the ground to make sure that the their performance meets the requirements. Static as well as dynamic loading tests should be done on the landing gear as well as the structure to ensure that they are designed to carry the expected loads during the entire mission.

After all "on-ground" tests are done on the aircraft, flight tests should be done to assess Tip-C in the air. The test flight should first start with testing Tip-C under more "gentle" flight conditions. This means that the climb gradient and rate should be kept low while a low AoA is used during cruise. A more gentle descent should also be done first. The aerodynamic properties of Tip-C during the flight phases should be recorded with a flight computer. During the testing of each flight phase, the stability should be assessed through pulse deflections of control surfaces to simulate gusts. The controllability of Tip-C can also be found with step inputs to the control surfaces and obtaining the pitch, roll and yaw rates following the input. In this phase of the test flight, the inputs for control surface deflections should be kept small, about $-0.25°$.

After the initial test flight shows that Tip-C is capable of performing its mission, the requirements for the test should be increased gradually to test the aircraft to its limit. The climb gradient and rate should be tested to its maximum and this should also be done for descent. During cruise, the AoA should be increased until stall occurs to obtain an accurate stall angle. The control surface deflections should also be gradually increased to simulate larger gusts to test for stability. For controllability, the control deflections should be tested until satisfactory pitch, roll and yaw rates are reached. In this phase of the test, it is also important to investigate the case of takeoff with one engine inoperative as it is an important factor in the design of the vertical tail fins. The entire flight mission with one engine inoperative should also be done. This is not only to ensure that Tip-C is still capable of flying in this condition, but also to let the pilot familiarise with such a situation in case it happens at some point during the competition.

16 Design Summary

In this chapter the final design is summarised. The most important results are shown together with values. After this, the requirements compliance is checked and evaluated. Finally, a general sensitivity analysis is performed.

16.1 Final Design

In this section the final design is summarised. For every department the most important findings are listed.

Aerodynamics

- The body airfoil is the Clark Y.
- The horizontal and vertical stabiliser use a Eppler 360 airfoil.
- The planform is an inverted plaster.
- The final body size is: b = 1.1045m, c_{root} = 1m, c_{tip} = 1.1m, AR = 1.06.

Stability

- For takeoff, climb rate, climb gradient, cruise and descent the Dutch Roll and Aperiodic Roll are stable, the Spiral is slightly unstable.
- The final tail size is: $C_{v_{root}}$ = 0.3m, $C_{v_{tip}}$ = 0.27m, b_v = 0.22, C_h = 0.27m, b_v = 0.3, x_h = 0.375m.
- The horizontal tail has an incedence angle of -2°.
- The vertical tail should have a to-be-defined toe-in angle.
- The final c.g. location is 0.2917m.

Controllability

- The elevator size is: b_e = 0.25m, C_e = 0.1m.
- The aileron size is: b_a = 0.25m, C_a = 0.15m, location from longitudinal axis b_{a_i} = 0.3314m.
- The rudder size is: b_r = 0.14m, C_r = 0.09m.
- For cruise Tip-C is controllable.
- For higher AoA and crosswind, the controllability should be checked.
- The belly flap size is: b = 0.1557m, C = 0.2506m, the longitudinal location is: 60% MAC.

Propulsion

- The maximum shaft power required is 2200W.
- The combined propeller and motor efficiency is 0.79.
- The propeller airfoil used for modelling is the Clark Y.
- The propeller diameter is 0.558m.
- The selected propeller is the XOAR PHJ-E 21x14.
- The selected engine is the Hacker A60-14L.

Performance

- The endurance is 0.85h.
- The range is 96.82 km.

- The maximum climb gradient is 40.94 deg, for a velocity of 22.58 m/s and an AoA of 16deg.
- The maximum climb rate is 15.96 m/s, for a velocity of 24.79 m/s and an AoA of 12deg.
- The takeoff distance is approximately 78m.
- The landing distance is approximately 118m.
- The maximum velocity is 46 m/s.
- The stall velocity is 19 m/s.

Landing Gear

- The nose gear is placed 0.02 from the reference axis.
- The main gair is placed at 0.32m from the reference axis.
- The minimum strut length is determined to be 0.32m.
- The maximum rotation angle is 25°.
- The load taken by one strut equals 647N.
- The diameterof the main gear wheel is 4.5inch. Of the nose wheel is 2.0inch.

Aircraft Systems

- The battery to be used is the HobbyKing 9169000008.
- The battery consists of 40 propulsion cells.
- Ten servos are used.
- The landing gear has its own separated linkages and actuator.
- The operating pressure of the landing gear retraction system is 690kPa.
- A pneumatic actuator is selected for the belly flap.

Structure

- The structure is hybrid and kept simple and light.
- It consists of a wingbox with 2 spars and 4 ribs.
- The chosen material is spruce wood and ROHACELL foam.
- The body and the C-wing consist of foam and spruce wood (spars and ribs).
- A plastic film would be used as the skin of the entire structure.

16.2 Requirements Compliance

In this section, the requirements are shown in table-format. If the requirement is not met, an explanation is given why it is not, and a possible solution is addressed. Only the most important requirements are checked. For example 'easy transportation' is not checked because it is not measurable. As seen in table 16.1, the maximum descent gradient is 19° which is lesser than the stated requirement of 30°. A solution to increase the descent gradient is to increase the drag artificially. This can be achieved by using rudders. They should be deployed asymmetrically to avoid any yaw moment. The other requirement not met is the structural efficiency. The structural efficiency is determined by dividing the payload weight by the MTOW. To increase the structural efficiency, the MTOW should decrease. This can be achieved by making the overall structure lighter. By doing so, the landing gear mass can also be decreased.

Table 16.1: Requirement Compliance.

Performance Parameters	Value	Velocity [m/s]	AoA [deg]	Design Req.	Req. met?
Range [km]	96.82	36.93	2	75	Yes
Endurance [Hours]	0.85	28.29	8	-	-
Maximum climb gradient [deg]	40.94	22.58	16	30	Yes
Maximum climb rate [m/s]	15.96	24.79	12	-	-
Maximum descent gradient [deg]	19	18.54	35	30	No
Takeoff distance (Analytical) [m]	78.22	-	-	120	Yes
Takeoff distance (Numerical) [m]	77.76	-	-	120	Yes
Landing distance (Analytical) [m]	114.15	-	-	150	Yes
Landing distance (Numerical) [m]	121.07	-	-	150	Yes
Maximum Velocity [m/s]	46	-	-	50	Yes
Stall Velocity [m/s]	19	-	-	-	-
Maximum Load factor	2.6	35	-	-	-
Minimum Turn radius [m]	42.28	26.43	-	-	-
Minimum time to turn [s]	9.24	35	-	-	-
Aspect Ratio [-]	1.06	-	-	1 to 3	Yes
Structural Efficiency [-]	0.22	-	-	0.25 to 0.45	No
MTOW [kg]	21.94	-	-	25	Yes
Carry Payload (5kg)	-	-	-	-	Yes

16.3 General Sensitivity Analysis

A sensitivity analysis is performed in order to research the impact on the design choices when a parameter changes in the design. In this section a general sensitivity analysis is performed to see which parameters affect the design the most. The design consists of parameters that change during the iterative process and parameters which do not change. The fixed parameters do not change since requirements fix these parameters to a certain value or a final value is reached because of another limiting factor. For example, the landing distance, the takeoff distance and AR range are fixed by the requirements. The most sensitive in this Final Report phase is the c.g. location and MTOW. Earlier, during the Mid-Term phase a N2-chart was created. Figure 16.1 on the next page displays the N^2-chart for the low AR UAV design. It displays the relation of the different design steps. The blocks are sorted time-wise, which means that processes lower on the diagonal are executed later than higher placed processes. Relations on the top of the diagonal indicate simple input-output relations. The output from the higher placed design steps can be used as input for the lower placed processes. For the relations underneath the diagonal the relation is also a input-output relation. This time however, the relation is going back to a higher placed process, i.e. an earlier design step.

For the Final Design phase also a Department Communication Diagram ("Malcom Diagram") is created. In this diagram the communications between the different departments is shown. If something is changed in your department, the arrows indicate to which department it should be communcated. The black circle around the departments show the MTOW and c.g. location. These are inputs which affects every department and can cause large changes.

- MTOW - AR - Oswald factor - Stall speed - TOP - Landing distance - CL_{max} - C_{batt} - Endurance - Range										
Class I Weight Estimation	MTOW									
	- Wing loading/ power loading diagram - Design point	Wing Area AR	Power Required	Amout of energy storage required						
		Planform Sizing			Wing span Chord length					
Engine Weight			**Propulsion Selection**			Thrust properties		Ground clearance propeller		Power Thrust Pitch
Battery weight Endurance Range				**Battery selection**						Energy
		Leading edge shape			**Planform layout**	Planform properties			Outer dimensions	L/D Stall angle Clmax
						Stability	Stabiliser location	c.g. location	Stabiliser locations	c.g. location
Control surface/ tail weight							**Controllability**		Control surface location Control surface mechanism	Manoeuvrability
Landing gear weight						c.g. location		**Landing gear**	Landing gear strut positions	Additional drag
Structure Weight							Inertia		**Structure**	Inertia
Endurance									Load Factor	**Performance**

Figure 16.1: N^2-chart.

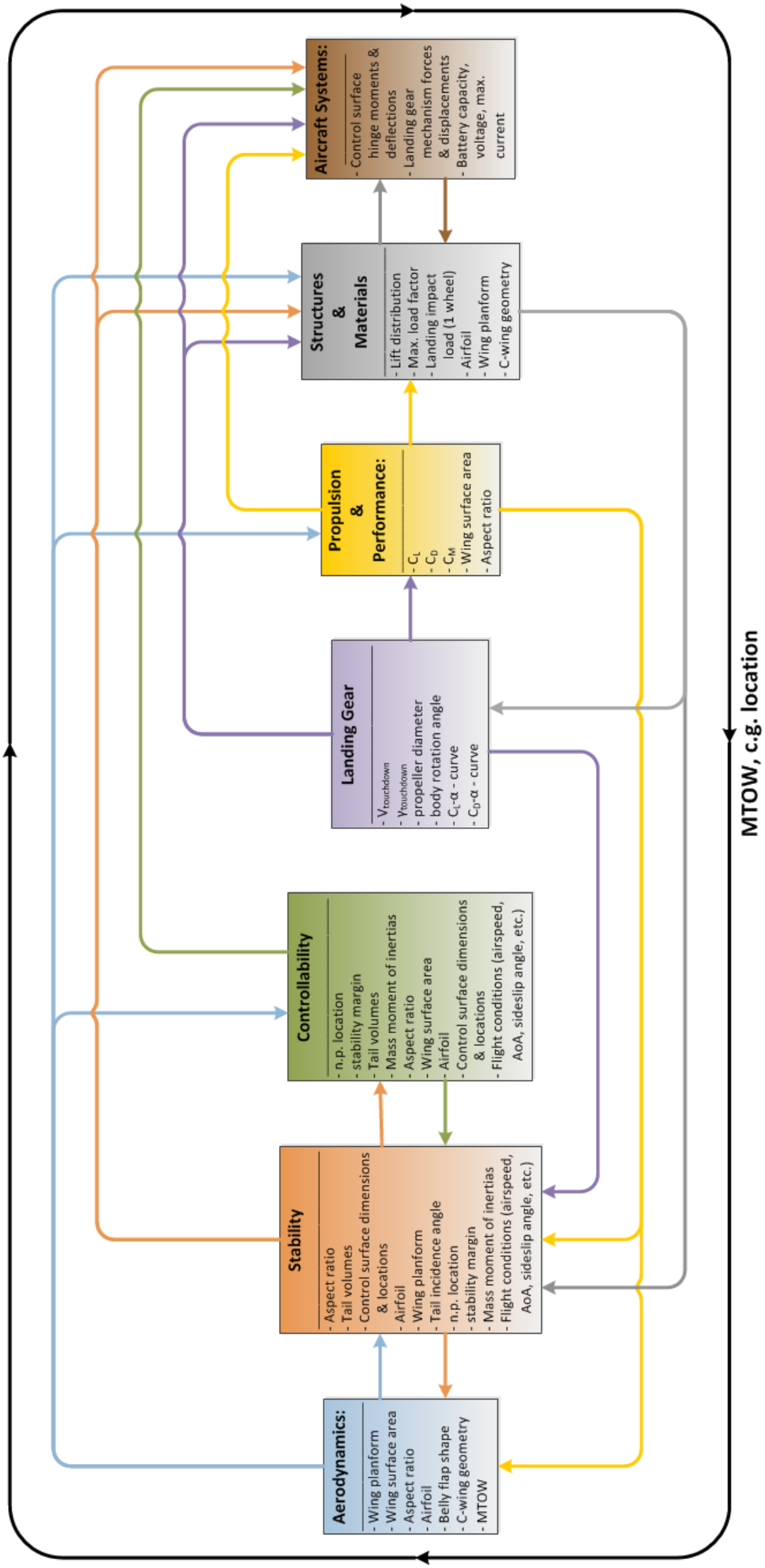

Figure 16.2: Department Communication Diagram.

17 Risk Management

While for the midterm report the risks of all the function concepts are discussed, in this chapter the risks of several aircraft disciplines are discussed. These disciplines are propulsion, landing gear, A/C systems, control/stability, main structures/materials, aerodynamics, manufacturing. Each of these components has their own risk criteria. For example, for a landing gear the manufacturing risk is determined and for aerodynamics the analysis risk is discussed. Based on this risk management, a better overview of the risk sensitive disciplines is found. More afford is put into a specific part if the risks are high. The different disciplines are also put in one figure to compare them.

17.1 Risk per Discipline

Each component has its own criteria. To start with aerodynamics.

Aerodynamics The same as for Control/Stability, the analysis errors risk and inaccurate results risk is determined. The analysis of the aerodynamic calculations are considered to be more difficult than the one of control and stability. The probability of analysis errors is therefore higher. The same goes for inaccurate results. However, the consequences of these inaccurate results are larger. There is no safety factor for aerodynamics, inaccuracy in the calculations result immediately in a worse performance. The risks can be found in figure 17.1.

Control/Stability This discipline is analysed on two completely other criteria. The risk for analysis errors and the risk for inaccurate results are taken into account. The analysis errors are a result of working with the wrong data of making mistakes during calculations or derivations. The inaccurate results are the result of software inaccuracy and rounding errors. As can be seen in figure 17.1, the analysis errors have an higher risk than the accurate results. This is quite obvious since an analysis error is happening more often and the if the result is made in the beginning, it works through the whole calculation/derivation. The inaccurate results are more or less taken into account, therefore a safety factor is used. The probability is therefore smaller and the consequence is suppressed by the safety factor.

Propulsion and Performance The risk criteria for propulsion are design, manufacturing, performance, maintenance and mission. The mission risk is considered to have the highest probability of occurrence and the highest consequence. For model air planes the risk of having a propulsion failure during mission is medium. The consequence are catastrophic. The aircraft is uncontrollable in case of having failing propulsion. Since the UAV does not have many engines, it is not able to land safely without damaging anything. The other criteria are given in figure 17.1.

Landing Gear The risk criteria for the landing gear are the same as for the propulsion. The mission risks are also rather high. The risks for the landing gear during the designing process and the manufacturing process are higher. This is because of the fact that the propulsion system is bought by a company with much experience producing these things while the landing gear involves some more afford from the people producing and designing the UAV. These people have less experience with this process than the companies which makes the propulsion system for years by now. The risk criteria with their corresponding is visualised in figure 17.1.

Aircraft Systems For the aircraft systems, the same criteria are used as for the previous two disciplines. As can be notices in figure 17.1, the risk of failing A/C system during mission is incredibly

high. The probability it happens is almost 100%. The consequences of this failure are catastrophic for the mission. Whether it happens during flight or during taxiing, it is not able to continue its mission. Maintenance and repairs have to be done first. The other criteria are more or less even to the previous risks of propulsion and landing gear.

Main Structure/Materials The risk criteria are the same as for the previous three disciplines. As can be noticed from figure 17.1, the mission risk is smaller than the mission risk of the other three disciplines. This is because the main structure and the materials are not moving or changing during mission. This results in a lower probability of occurrence. The designing process risk is a lot higher in this case. That is obvious because it mainly depends on how it is designed. The other criteria and score can be found in the figure.

Manufacturing This discipline has totally different risk criteria. This is because it is not a designing aspect. During the designing process, it is kept in mind. The manufacturing risks are determined for the executions process errors, structural complexity, preparation failure and insufficient experience. The execution process errors always happen somewhere but are rather small. It is always possible to make mistakes during manufacturing, this is very human. The consequences are a bit larger since errors during the manufacturing process result in weaker structure and other aspects. The preparation of a mould for example can go wrong very easily. Components made out of composite fibers in a mould can be damaged very easily if no release agent is used. Since the UAV is build in China in a place where there are many experienced people, the risk due to inexperienced people is quite small. The risks of manufacturing can also be found in figure 17.1.

Combined Design Disciplines All the seven disciplines are taken together and put in one figure. From this figure, a conclusion can be drawn about which disciplines have more/higher risks. As can be seen in figure 17.1, the landing gear is a high risk discipline while the controllability and stability the risk is small.

17.2 Results

Having discussed the risks in section 17.1, conclusions are drawn. The consequences of any failure of the landing gear is quite catastrophic and it happens quite a lot. To lower the risk of the landing gear, more afford is put in this discipline to lower the probability of errors. For the propulsion and aircraft systems, the risks during mission are significant higher than for the other criteria. This risks are reduced by increasing the maintenance time for these components of the aircraft. The risks of the main structure and materials are higher during the design than during the mission. More afford is put into the designing process of this discipline. For the aerodynamics discipline, the analysis errors are worse than the analysis errors for the control and stability discipline. For aerodynamics, this is checked stricter than for the control and stability. The manufacturing can only be checked theoretically. The people in china should decide how much extra attention they pay to this discipline.

The overall design disciplines are plotted in one figure (see figure 17.1, right bottom). The landing gear contains the highest risk. This is based on more or less the average of all the values in the other figures. Close behind the landing gear, the main structure/materials, aerodynamics and aircraft systems have an high risk. The others can be considered to have low to medium risk.

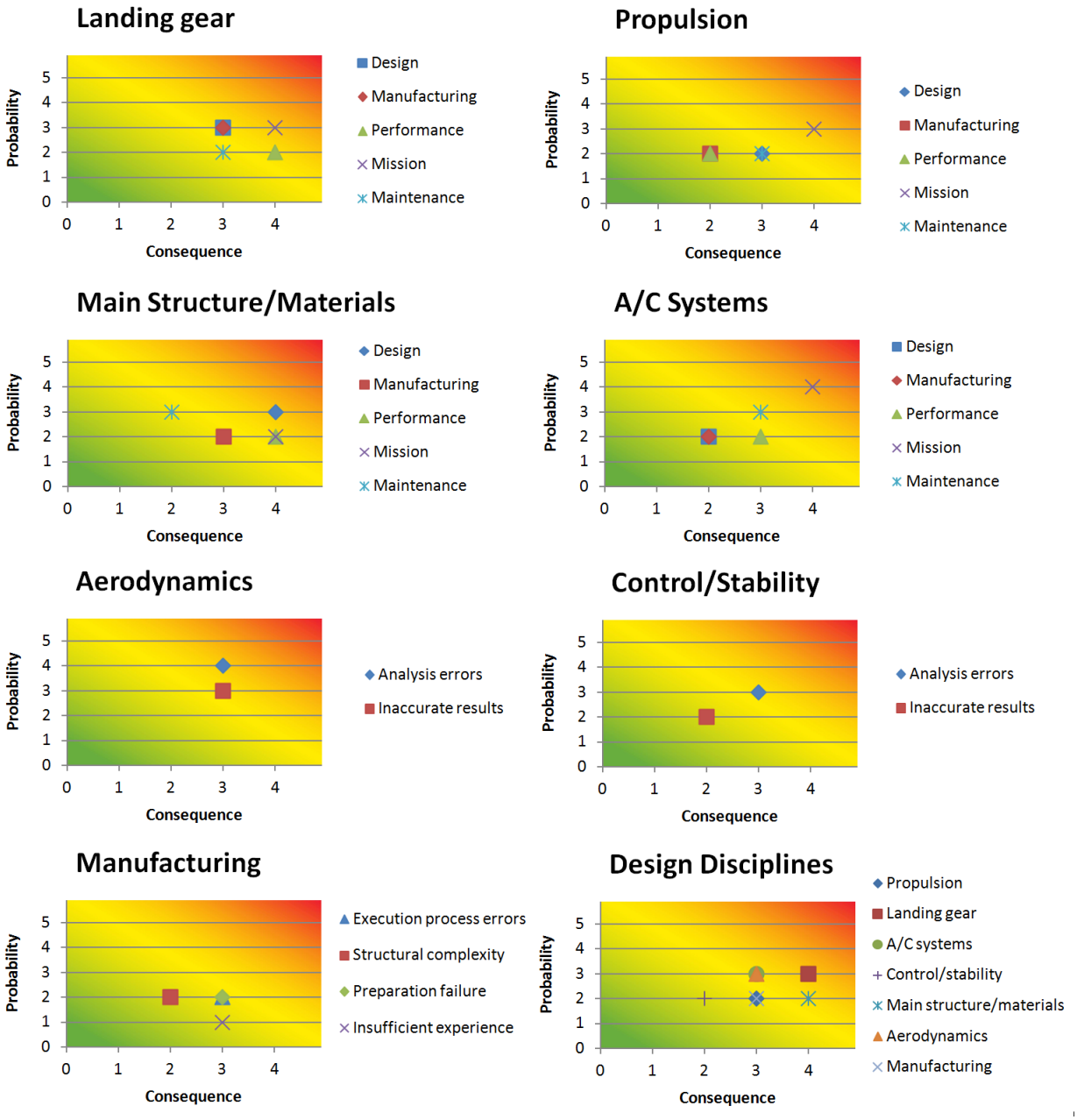

Figure 17.1: Risk maps of the discipline risks

18 Sustainable Development Strategy

The sustainable character of Tip-C is assured by several aspects. As the vehicle is electrically driven, the operating CO_2 emission is zero. This propulsion system also allows for very low noise levels. As a result, the use of ecologically friendly resources is the way to go.

The first tackle point is the power source. Nowadays, lithium-ion batteries are the most commonly used batteries, these are less polluting than common alkaline batteries. However, nickel metal hydride batteries contain no toxic heavy metals at all and they are recycled easily. These advantages come with the price of the weight and volume. In the design process the sustainability of the different batteries is taken into account.

Next to the batteries, the production materials are sustainable as well. Tip-C is not only made out of recycled materials, but it is used as much as possible. One could think of wood, recycled plastic or recyclable aluminium. Materials as carbon fibre are to be considered but they are difficult to recycle and their quality decreases during the process. Current research shows that the quality decrease can be avoided by solvolysis. This however increases the recycle cost considerably. Therefore, one should make a trade-off between sustainability, recycle cost and performance of the chosen material.

Sustainability should also be taken into account in the production process. Energy intensive processes should be avoided, unless these contribute enormously to the aircraft performance. Again, a trade-off should be made.

Another sustainability aspect is the climb and descent performance of the aircraft. The magnitude of climb rate and descent rate are much higher than they are for a conventional aircraft. When implementing the aircraft in the personal transport sector, smaller runways can be used. Smaller runways are easier to integrate in inhabited areas where there is not much space left for large airports.

Due to the low AR, the structural efficiency is very high, this allows for a less complex and a less heavy structure. A less complex structure is beneficial for production, which makes the process easier. A less heavy structure is beneficial in case of energy consumption. Less weight requires less power, the heavier the structure, the more power required. When using the aircraft in the general aviation sector, it is really important to save weight. The lower the Operational Empty Weight (OEW) the more payload the airline can transport, the more money they earn.

Another advantage of the low AR is the storage. Since the wing span is very much shorter, smaller boxes or hangards are required to park and maintain the aircraft. This reduces the space required near airports.

The final costs of Tip-C are not only materials, components and production costs, but also the designing costs. Design Life-Cycle Costing (LCC) is implemented in all the steps that are taken. This includes purchase prices, installation costs, operating and maintenance costs, and remaining value at the end of life. During the design cycle, time is used efficiently. The final design should be reliable such that maintenance costs are limited.

The manufacturing aspect has a large potential to be sustainable. Tip-C will be manufactured in China, which is very beneficial for transport costs (since the competition is in China). Most of the components, such as batteries and cables, are produced in China, so they do not have to be transported all over the world. This saves transport costs but it also reduces the CO_2 emission.

If a sustainable development analysis is done, not only the use of environmental friendly working is required. If the newer design replaces something which is not environmental friendly at all, sustainability is also achieved. The aircraft coming from the designs, mentioned in this report, easily replace an aircraft which uses kerosene or other environmental unfriendly fuel and production methods.

19 Market Analysis

In this chapter, the specific market analysis is discussed. This kind of market analysis is different from a general market analysis because at this point, the final design is known. The analysis is done for this specific design. There are four possible markets for these designs: military aircrafts, civil passenger aircrafts, model airplanes and personal air travel. For the militairy application Tip-C can be used to follow an enemy. Due to the steep climb and descent, Tip-C can descent quickly, complete its mission (throwing something on the ground, espionage something close to the ground) and climb quickly to a safe altitude. It can also be used for supply. If something must be transported between two army bases, Tip-C can steeply climb to a safe altitude and descent quickly at the target base. There the payload is unloaded and Tip-C flies back to its original base. A less suitable, but still doable other application is using Tip-C for surveillance. Due to the low AR the cruise performance is not as high as for high AR UAV, but it is still high enough to fly for a long time on one battery, if the surveillance is around for example an army base, Tip-C can land, the battery can be replaced and it can continue with its mission.

Another application is for reconnaissances missions. The aircraft is small, silent, difficult to trace and is capable of flying a wide range. For large passenger aircrafts it is not of great use. The cruise performance of a high AR aircraft is still better and if offers more space for passengers. Two markets are left, the model airplane market and the civil personal air travel market. For the last market, several aspects like safety, costs, fuel efficiency and the difficulty of flying one of these concepts, are discussed. The regulations of a model aircraft are less strict than the regulations for a human carrying aircraft.

The very first criteria, for carrying people on board of an aircraft, is the safety. Safety of an aircraft starts the moment a person is entering the area were the vehicle is parked. Since the aircraft is negligible dangerous if it is not turned on, the real risks are increasing from the moment the passenger/pilot enters the vehicle. After that controlling the aircraft along the runway can be quite challenging since most people are not well experienced in piloting the aircraft, but still want to fly on their own. To make this possible, stability and controllability have to be considered. The use of a vertical and horizontal stabilizer is increasing the safety up until the aircraft becomes to difficult to control. If it is too stable, the pilot can not control it properly which makes it dangerous. Landing must be as easy as possible. The used tricycle landing gear has good stability properties during ground control and landing. When Tip-C is used for personal air travel, safety is a big issue. The scale model designed by now should be made on larger scale.

For the second criteria, model aircraft, the regulations are less strict than for a human carried vehicle. But safety and maintenance do still play a big role on the market share it will have if it will be taken into production. For model aircraft, the more innovative a design is the more it attracts peoples attention.

20 Resource Allocation

In this chapter a summary is given on the total cost and weight distribution for the different departments. The MTOW is specified to be 25 kg. The budget is ¥50,000 which is around €6200.

20.1 Mass Distribution

In this section the final mass of all components is shown. The details are already presented in the department chapter (4-10). The structure is splitted in wood and foam.

Table 20.1: Total mass distribution.

		Mass [kg]
Payload		5.00
Structure		
	Foam	3.87
	Spruce Wood	2.65
Landing Gear		2.25
Electrical System		0.61
Mechanical System		0.05
Pneumatic System		0.36
Battery		5.13
Engine		1.82
Propeller		0.22
Total		**21.94**

20.2 Cost Distribution

In this section the final cost of all components is shown. The details are already presented in the department chapter (4-10). For the structure an extra of 50% is added to account for the waste.

Table 20.2: Total cost distribution.

		Price [€]
Structure		
	Foam	585.53
	Spruce Wood	6.00
Landing Gear		400.00
Electrical System		1122.80
Mechanical System		24.00
Pneumatic System		412.86
Battery		828.13
Engine		598.00
Propeller		54.00
Total		**4031.32**

21 Conclusion and Recommendations

In this report, the detailed design of a low AR UAV with tip-mounted propellers is presented. The finished design will be sent to NPU for further development and testing before it is produced and sent to Beijing for the AVIC Cup - International UAV Innovation Grand Prix. This design is optimised for steep climb and descent with satisfactory cruise efficiency, so that the concept of airports within city centres can be realised. Innovation is aimed for throughout the design process, while also keeping aspects such as sustainability into account. The final configuration of Tip-C has an inverted plaster planform with tip-mounted propellers and a C-wing which also acts as vertical and horizontal stabiliser. Retractable landing gears are used to reduce drag during cruise. Below, the conclusions and recommendations of each technical department are listed:

Aerodynamics
The aerodynamics are analysed using mainly the programs XFLR5 and QProp. The final airfoil chosen for the main wing is the Clark Y. For the vertical surface of the C-wing, the Eppler 360 is chosen, and for the horizontal surface an inverted Eppler 360 is chosen. The final planform dimensions are: $c_{tip} = 1.10$, $c_{root} = 1.00$ and $b = 1.1045m$. The vertical tail is designed with a 2° toe-in angle and the horizontal tail, a -2° incidence angle. Using tip-mounted propellers is found to give only a 1% increase in L/D. When the tail is added, the L/D is decreased by 15.7%. When including trim drag, the final L/D has a value of 8.1. Due to inaccuracies and limitations of the software used, it is suspected that the drag values are underestimated and the results near the stall angle are not accurate.

Stability
The stability of the design is analysed using the Vortex Lattice Method software Tornado and AVL. Tip-C is longitudinally stable in all flight conditions except for climb. However, in this phase, the instability is barely noticeable so it is acceptable. For asymmetric motions, the Dutch roll and aperiodic roll are stable for all flight conditions while the spiral is always slightly unstable. The instability is extremely small and is not uncommon for an aircraft. However, all analyses are performed without taking propellers into account. It is predicted that with the propellers activated, the lateral and longitudinal static stability decreases. The effect of propellers on stability should be tested with CFD or wind tunnel tests. Another important aspect is to investigate the stability during takeoff with one engine inoperative or when flying with crosswind.

Controllability
The controllability of the design is calculated, based on the control derivatives calculated with Tornado and AVL. During cruise, controllability meets the requirements. In the other flight phases at high AoA, high trim deflection angles are required, which reduces controllability. For takeoff, the calculated pitch rate is $12 - 20^\circ/s$ while required pitch rate is $30^\circ/s$. Crosswind has not been analysed. Hinge moments should be verified with extensive CFD. The belly flap has $b = 0.1557m$, $c = 0.2506m$ and a 23% porosity, based on literature.

Propulsion
Initially, the engine Hacker A60-7SV2 is chosen. This is later changed to the more powerful Hacker A60-14L in order to meet the performance requirements. The XOAR beechwood propeller with a 21" diameter and 14" pitch is selected. The blade diameter is relatively large as this is highly influenced by the large static thrust requirement for takeoff while the large propeller pitch is chosen to accommo-

date the high operational speed of Tip-C. The combined engine and propeller efficiency is 0.79. This is more efficient as compared to other engine types such as the turboprop (approx. 0.39),turbofan (approx. 0.33) and fuel cell (approx. 0.44).

Performance
The performance of Tip-C is verified by comparing its performance characteristics with the design requirements. It is found that all of the performance requirements are met except for the descent gradient. The required descent gradient is 30°, but the achievable descent gradient for Tip-C is 19°. In order to increase the descent performance, artificial drag inducers can be added. For the performance modelling, one recommendation would be to include the presence of wind (headwind, tailwind, crosswind, etc) and ground effect in the program. It is also highly recommended to analyse the takeoff performance with one engine inoperative. Other flight phases such as climb, descent and turn can also be simulated to verify the analytical solutions. The overall transport efficiency of Tip-C (1.85) is found to be almost similar to these general aviation aircraft.

Landing Gear
A retractable tricycle landing gear configuration is chosen to reduce drag during climb and cruise. Compared to conventional tricycle landing gears, the main landing gear of Tip-C is closer to the nose. This is because of the forward location of the c.g. It is also longer to account for the ground clearance of the large propellers. The main gears are located $0.03m$ behind the c.g. at 32% of the chord, while the nose gear is located $0.02m$ behind the nose at 2% of the chord. Commercial off-the-shelf landing gears have been sought online from the company "Robart", but the components found are shorter than the designed length. Hence it is recommended to approach the manufacturer to see if the parts can be modified. If this is not possible, modifications should be done during production.

Aircraft Systems
The final mass of the main batteries used for the engines is $4.98kg$, and an additional $0.148kg$ is needed to power the electrical systems. Servos are used to move the control surfaces, while pneumatic actuators are chosen for the landing gear, brakes and belly flap. A $2.4GHz$ onboard radio is used for ground communications. Currently, the hinge moment used to size the control surface mechanisms are provided by Tornado and AVL, but this is not possible for the belly flap as it cannot be implemented in the software. Hence it is recommended to verify the estimations made for the belly flap hinge moments. It should then be checked if the chosen actuator meets the required force and stress limits.

Structures
The structure of Tip-C is kept simple as there are no complicated loads or large moments acting on it. The simple structure is also desirable for easy manufacturing. The structure is made up of a wingbox with 2 spars and 4 ribs. Rectangular cross-sections are used for the spars, taking into account manufacturability as well. The loads on the C-wing are found to be small. Spruce wood is used for the main structure while foam is used to fill up the remaining empty spaces. The MTOW is found to be 21.94 kg.

Even though a lot of work has already been done on optimising and analysing the design, there are still many areas to improve on. Due to time limitation and the lack of available software, the analysis could not be done on a more detailed level. Hence, recommendations and suggestions are made which hopefully prove useful for NPU or other parties who are interested in the further development of this design.

Bibliography

[1] Gundlach, J., *Designing Unmanned Aircraft Systems - A Comprehensive Approach*, American Institute of Aeronautics and Astronautics, 1st ed., 2012.

[2] Aeronautics, N. and (NASA), S. A., "Wake Vortex Study," 1996.

[3] McCormick, B. W., *Aerodynamics, aeronautics and flight mechanics*, John Wiley and Sons, Inc., 1995.

[4] Demasi, L., "Investigation on Conditions of Minimum Induced Drag of Closed Wing Systems and C-Wings," Tech. rep., University of Washington, Seatlle, 2007.

[5] Hueners, R. L. and Rasmussen, C., "XFOIL project," Tech. rep., California Polytechnic State University, Aerospace Engineering Dept, 2000.

[6] Anderson, J. D., *Fundamentals of aerodynamics*, McGraw-Hill, 2011.

[7] Maskew, B., *Program VSAERO Theory Document: A Computer Program for Calculating Nonlinear Aerodynam Characteristics of Arbitrary Configurations*, National Aeronautics and Space Administration, 1987.

[8] Drela, M., *QPROP Formulation*, MIT Aero and Astro.

[9] Brown, M., Gamme, S., Laan, R., Abadi, P. M. S., Padmos, S., Regtuit, R., Schmeetz, M., Tan, Y., Timmer, B., and Wang, X., "DSE - mid-term report, Design of a Low Aspect Ratio UAV," 2013.

[10] Kroo, I., "Nonplanar wing concepts for increased aircraft efficiency," Tech. rep., Stanford University, June 2005.

[11] Roy H. Lange, Bennie W. Cocke, J. A. J. P., "Langley Full-Scale Tunnel Investigation of a 1/3-scale Model of the Chance Vought XF5U-1-airplane," Tech. rep., Bureau of Aeronautics, Navy Department, 1949.

[12] ONLINE http://www.http://en.wikipedia.org/wiki/Cessna_150, [Online; accessed 23-June-2013].

[13] Schroijen, M. J. T., Veldhuis, L., and Slingerland, R., "Propeller Empennage Interaction Effects on Vertical Tail Design of Multiengine Aircraft," *Journal of Aircraft*, Vol. 47, No. 4, July-July 2010.

[14] Eshelby, M. E., "The Influence of Running Propellers on Low Speed Longitudinal Static Stability Trim Curves," Cranfield Report Aero 34, Cranfield Institute of Technology, April 1977.

[15] Katzoff, S., "Longitudinal Stability and Control with Special Reference to Slipstream Effects," Report 690, National Advisory Committee for Aeronautics, 1940.

[16] Stewart, K., Wagener, J., Abate, G., and Salichon, M., "Design of the Air Force Research Laboratory Micro Aerial Vehicle Research Configuration," *American Institute of Aeronautics and Astronautics*, Vol. 45, 8-11 Jan. 2007.

[17] Stanford, B., Abdulrahim, M., Lind, R., and Ifju, P., "Investigation of Membrane Actuation for Roll Control of a Micro Air Vehicle," *Journal of Aircraft*, Vol. 44, No. 3, May-June 2007.

[18] Royer, D. A., Keshmin, S., Sweeten, B. C., and Jones, V., "Modeling and Sensitivity Analysis of the Meridian Unmanned Aircraft," *American Institute of Aeronautics and Astronautics*, 20-22 April 2010.

[19] Traub, L. W., "Experimental Investigation of Annular Wing Aerodynamics," *Journal of Aircraft*, Vol. 46, No. 3, May-June 2009.

[20] ONLINE http://web.mit.edu/drela/Public/web/avl/avl_doc.txt, [Online; accessed 17-June-2013].

[21] Melin, T., "A Vortex Lattice MATLAB Implementation for Linear Aerodynamic Wing Applications." 2000-12.

[22] Melin, T., "User's Guide and reference manual for Tornado 1.0," 2000-12.

[23] Mulder, J., van Staveren, W., van der Vaart, J., de Weerdt, E., in t Veld, A., and Mooij, E., *Flight Dynamics Lecture Notes*, Delft University of Technology, 2013.

[24] Sadraey, M. H., *Aircraft Design: A Systems Engineering Approach*, John Wiley and Sons Ltd., October 2012.

[25] Staelens, Y. and Blackwelder, R., "Study of Belly-Flaps to Enhance Lift- and Pitching Moment Coefficient of a BWB-Airplane," Tech. rep., University of Southern California, Viterbi School of Engineering, 2007.

[26] LaRocca, G., "Tail data, Controllabilty and Stability," AE3201 System Engineering and Aerospace Design, 2013.

[27] Fu, W., Li, J., and Wang, H., "Numerical Simulation of Propeller Slipstream Effect on A Propeller-driven Unmanned Aerial Vehicle," *Procedia Engineering*, Vol. 31, No. 0, 2012, pp. 150 – 155, International Conference on Advances in Computational Modeling and Simulation.

[28] Ruijgrok, G., *Elements of Airplane Performance*, VSSD, 2009.

[29] Jay, G., *Designing Unmanned Aircraft System - A Comprehensive Approach*, Knovel Corporation, 2012.

[30] Voskuij, M., *Flight and Orbital Mechanics, "Takeoff and Landing Performance" AE2104-11*, TU Delft, 2011.

[31] Holten, T. o., *Flight path simulations AE2201*, TU Delft, 2006.

[32] ONLINE http://en.wikipedia.org/wiki/Conventional_landing_gearDisadvantages, [Online; accessed 21-June-2013].

[33] Jha, A., "Landing Gear Layout Design for Unmanned Aerial Vehicle," *14th National Conference on Machines and Mechanisms*, Vol. 1, 2009.

[34] Currey., N. S., *Aircraft Landing Gear Design*, American Institute of Aeronautics and Astronautics, 1st ed., 1988.

[35] Megson, T., *Aircraft Structures for Engineering Students*, Butterworth-Heinemann, 2007.

[36] Raymer, D. P., *Aircraft Design: A Conceptual Approach*, American Institute of Aeronautics and Astronautics Inc., 3rd ed., 1999.

[37] ONLINE http://www.goodyearaviation.com/resources/pdf/datatires.pdf, [Online; accessed 7-June-2013].

[38] ONLINE http://upload.wikimedia.org/wikipedia/commons/8/8e/Triangle_with_notations.svg, [Online; accessed 18-June-2013].

[39] ONLINE http://www.robart.com/, [Online; accessed 21-June-2013].

[40] ONLINE http://www.robart.com/products/58-dia-straight-robostrut, [Online; accessed 23-June-2013].

[41] ONLINE http://www.robart.com/products/5-no-spoke-aluminum-wheel-brake-ready, [Online; accessed 23-June-2013].

[42] ONLINE http://www.robart.com/products/2-straight-tread-wheel, [Online; accessed 23-June-2013].

[43] ONLINE http://hobbyking.com/hobbyking/store/___11031___Hydraulic_brake_Assembly_for_90_100mm [Online; accessed 22-May-2013].

[44] ONLINE http://www.melasta.com/product.asp?lie=Lithium polymer battery, [Online; accessed 24-June-2013].

[45] ONLINE http://www.hobbyking.com/hobbyking/store/___25030___Turnigy_LSD_6_0V_2300mAh_Ni_M [Online; accessed 24-June-2013].

[46] ONLINE http://shop.dubro.com/p/4-40-steel-solder-rod-ends-qty-pkg-2, [Online; accessed 25-June-2013].

[47] anon., *Distribution Requirements Section*, Department of Transportation, Federal Aviation Administration.

[48] Roskam, J., *Airplane Design Part 5: Component Weight Estimation*, DAR Corperation, 1st ed., 1985.

[49] Hibbeler, R., *Engineering Mechanics Statics*, Pearson, 2010.

[50] Granta Design, CES, software, Version 11.9.9, 2012.

[51] Dassault Systems S.A., Abaqus, Software, Version 6.10, 2010.

[52] ONLINE http://www.hacker-motor.com, [Online; accessed 16-June-2013].

[53] ONLINE http://www.intercitylumber.com/Pine_and_Spruce_Prices.php, [Online; accessed 27-June-2013].

[54] ONLINE http://www.svsp.co.uk/store/Rohacell-IGF51-stock.html, [Online; accessed 28-June-2013].

[55] ONLINE http://theringlord.com/cart/shopdisplayproducts.asp?id=73cat=Saw+Cutting+Tools, [Online; accessed 30-June-2013].

A CATIA drawings

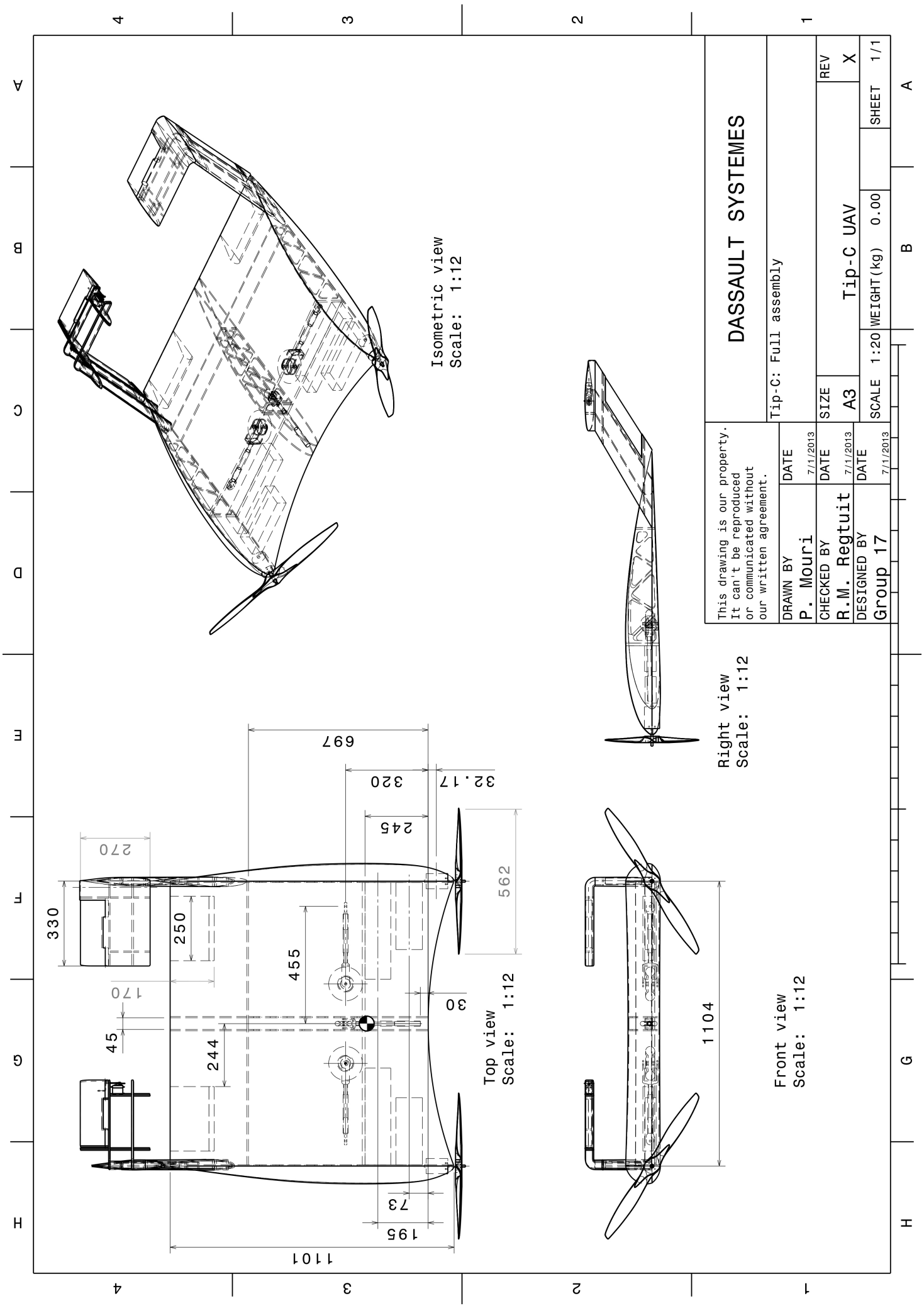

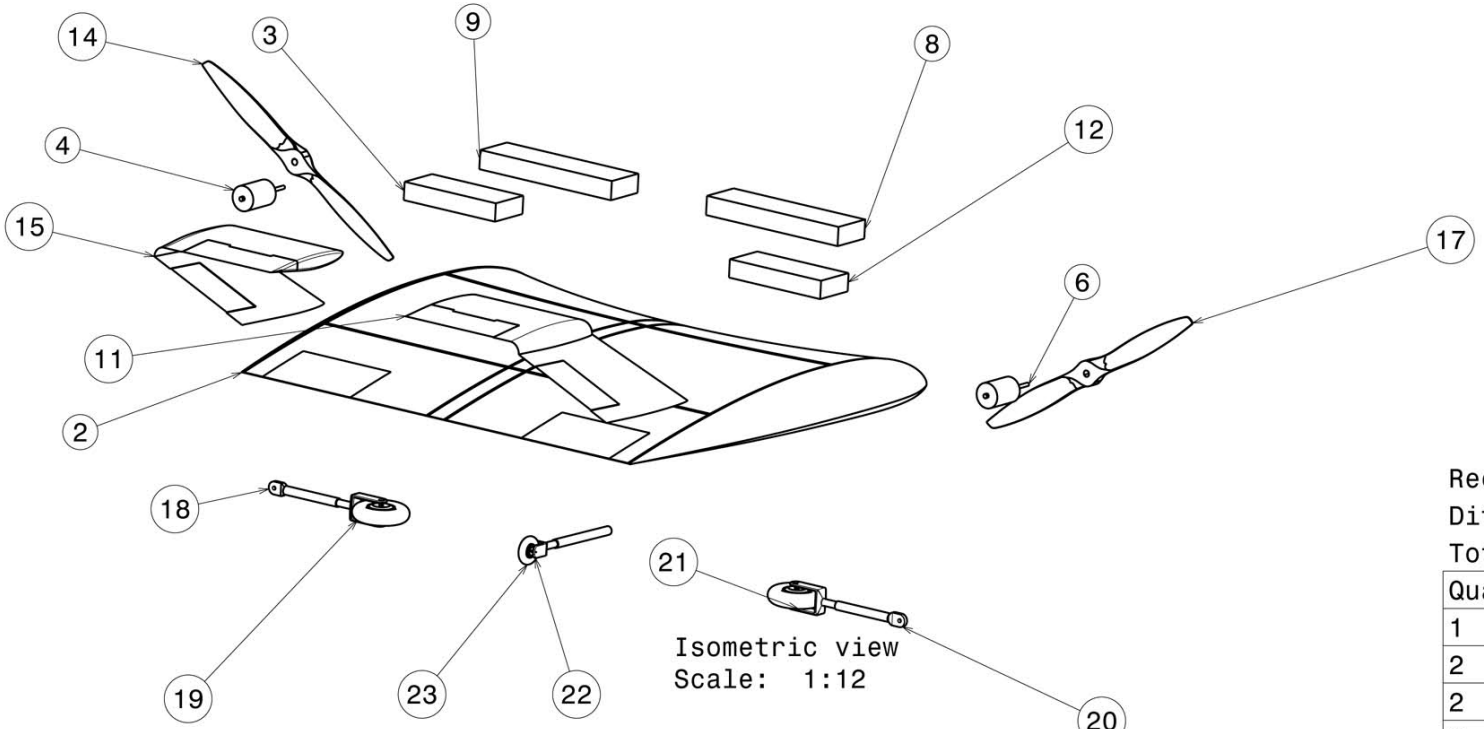

Isometric view
Scale: 1:12

Recapitulation of: Product1
Different parts: 35
Total parts: 40

Quantity	Part Number	Number
1	Body	2
2	Propulsion Battery	3
2	Motor	4
2	Main landing gear strut	18
2	Robart 5-inch tyre	19
2	Payload	8
1	Nose gear	22
1	Robart 2-inch tyre	23
4	Rib	10
2	C-wingg	11
2	Propeller 21' x 14'	14

DASSAULT SYSTEMES

DRAWING TITLE
Tip-C: Exploded View

DRAWN BY: R.M. Regtuit	DATE: 7/2/2013	SIZE: A3	REV: X
CHECKED BY: P. Mouri	DATE: 7/2/2013	SCALE: 1:12	SHEET: 1/1
DESIGNED BY: Group 17	DATE: 7/2/2013		

Recapitulation of: Main landing gear
Different parts: 7
Total parts: 7

Quantity	Part Number	Number
1	Top strut	1
1	Lower strut	2
1	Robart 5-inch tyre	3
1	Mechanism strut	4
1	Mechanism triangle	5
1	Ring	6
1	Connection shaft	7

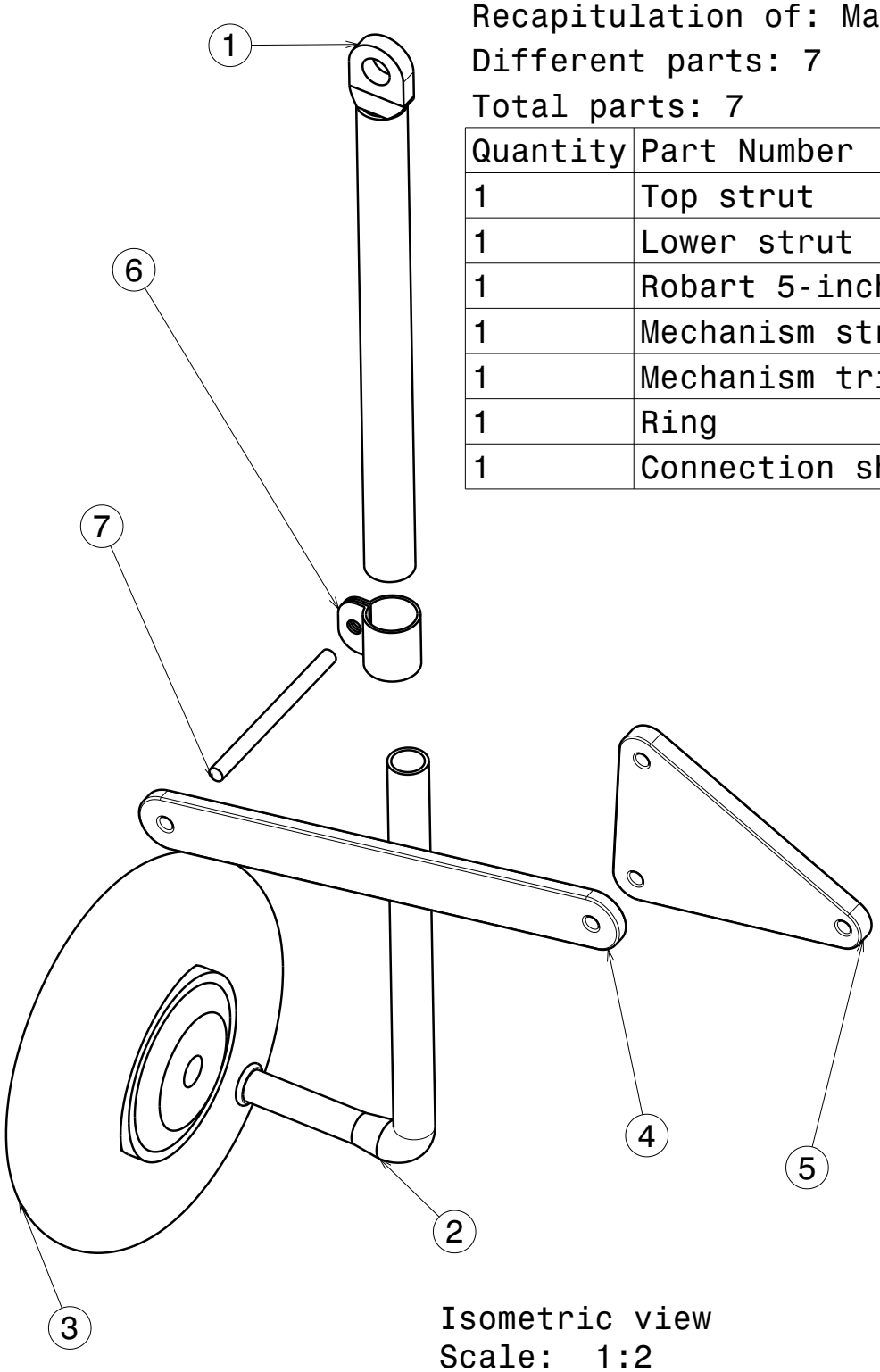

Isometric view
Scale: 1:2

DASSAULT SYSTEMES

Tip-C: Landing gear

DRAWN BY: R.M. Regtuit	DATE: 7/1/2013		
CHECKED BY: M. Schmeetz	DATE: XXX	SIZE: A4	REV: X
DESIGNED BY: Group 17	DATE: 7/1/2013	Main landing gear assembly	
		SCALE 1:2 WEIGHT(kg) XXX	SHEET 1/1

Recapitulation of: Nose gear
Different parts: 7
Total parts: 7

Quantity	Part Number	Number
1	Robart 2-inch tyre	1
1	Nose strut lower	2
1	Top strut nose	3
1	Ring	4
1	Mechanism triangle	5
1	Mechanism strut	6
1	Nose connection shaft	7

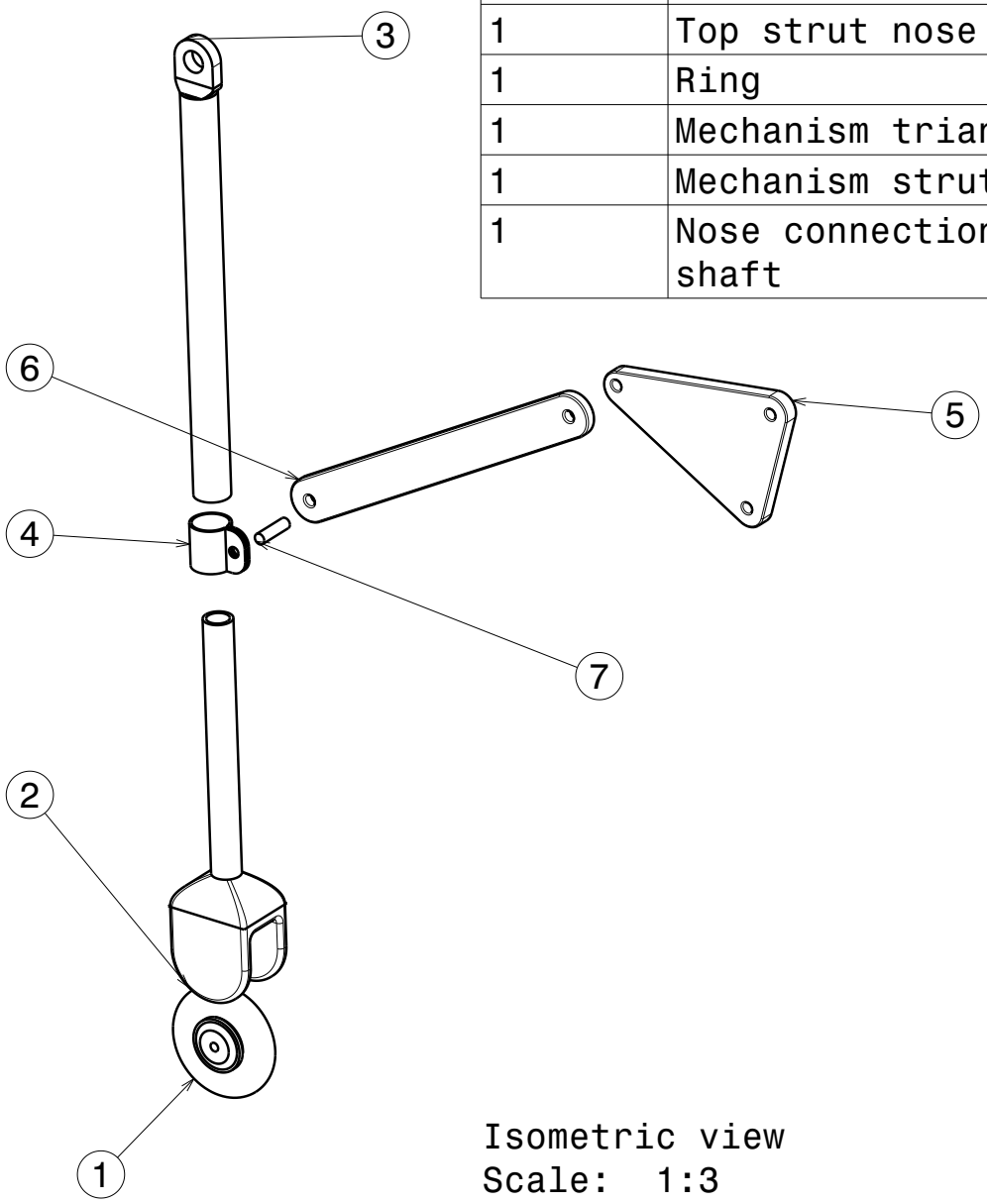

Isometric view
Scale: 1:3

DASSAULT SYSTEMES

Tip-C: Nose landing gear

DRAWN BY: R.M. Regtuit	DATE: 7/1/2013		
CHECKED BY: M. Schmeetz	DATE: 7/1/2013	SIZE: A4	REV: X
DESIGNED BY: Group 17	DATE: 7/1/2013	Nose landing gear assembly	
		SCALE 1:3 WEIGHT(kg) XXX	SHEET 1/1

NOTE: The detailed drawings of the components will be sent to NPU separately.

B Gantt Chart

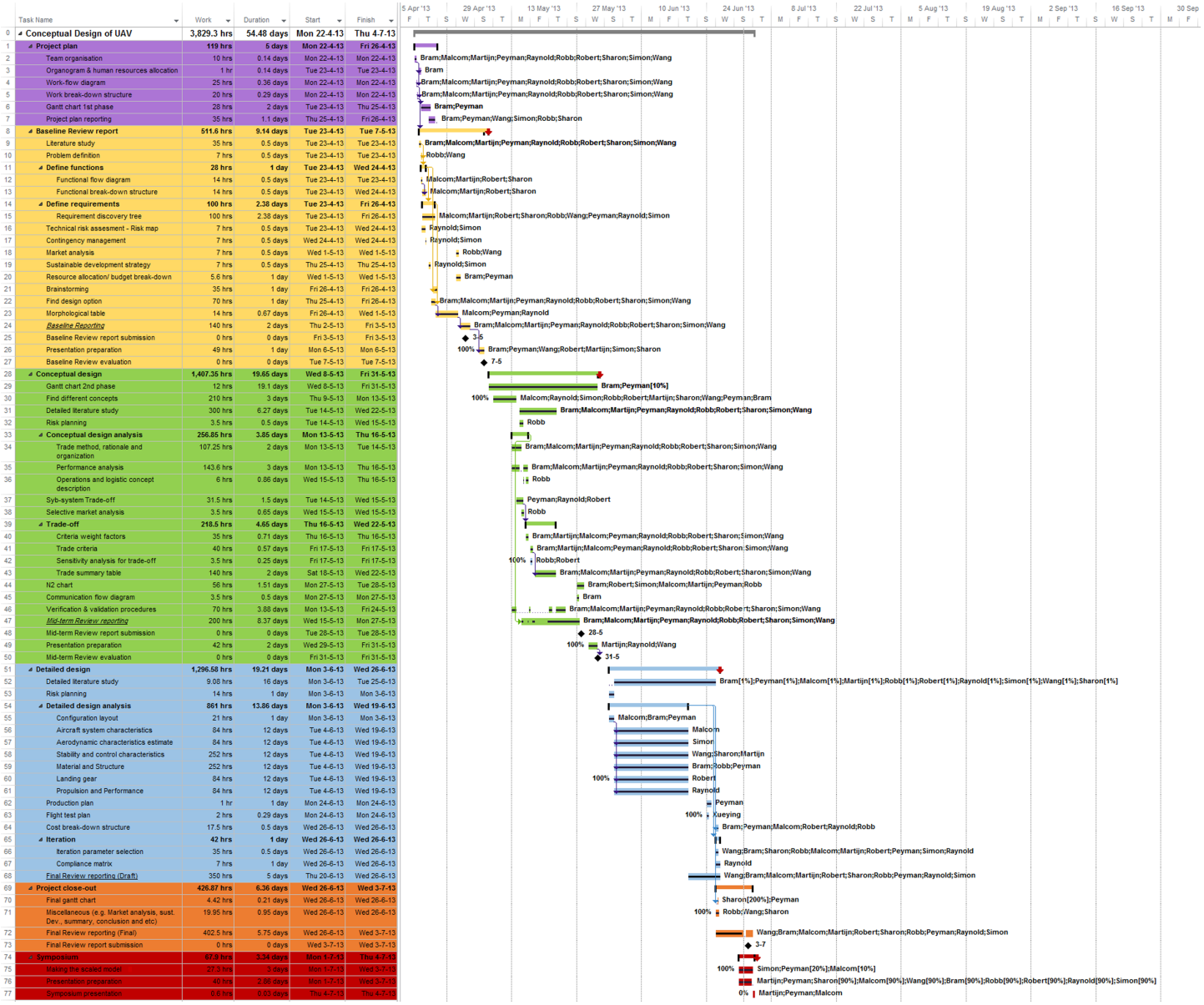

Figure B.1: Gantt chart of the DSE project.